



저작자표시-동일조건변경허락 2.0 대한민국

이용자는 아래의 조건을 따르는 경우에 한하여 자유롭게

- 이 저작물을 복제, 배포, 전송, 전시, 공연 및 방송할 수 있습니다.
- 이차적 저작물을 작성할 수 있습니다.
- 이 저작물을 영리 목적으로 이용할 수 있습니다.

다음과 같은 조건을 따라야 합니다:



저작자표시. 귀하는 원저작자를 표시하여야 합니다.



동일조건변경허락. 귀하가 이 저작물을 개작, 변형 또는 가공했을 경우에는, 이 저작물과 동일한 이용허락조건하에서만 배포할 수 있습니다.

- 귀하는, 이 저작물의 재이용이나 배포의 경우, 이 저작물에 적용된 이용허락조건을 명확하게 나타내어야 합니다.
- 저작권자로부터 별도의 허가를 받으면 이러한 조건들은 적용되지 않습니다.

저작권법에 따른 이용자의 권리는 위의 내용에 의하여 영향을 받지 않습니다.

이것은 [이용허락규약\(Legal Code\)](#)을 이해하기 쉽게 요약한 것입니다.

[Disclaimer](#)

공학박사 학위논문

석출법을 이용한 생체 의료용 히알루론산 하이드로젤  
나노복합체

**Hyaluronic Acid Nanocomposite Hydrogels via  
*In situ* Precipitation Process  
for Biomedical Applications**

2017년 8월

서울대학교 대학원

공과대학 재료공학부

정설하

석출법을 이용한 생체 의료용 히알루론산 하이드로젤  
나노복합체

**Hyaluronic Acid Nanocomposite Hydrogels via In-situ  
Precipitation Process for Biomedical Applications**

지도교수 김 현 이

이 논문을 공학박사 학위논문으로 제출함

2017 년 4 월

서울대학교 대학원

재료공학부

정 설 하

정 설 하의 박사 학위논문을 인준함

2017 년 5 월

위 원 장 안철희 (인)

부위원장 김현이 (인)

위 원 선 정윤 (인)

위 원 김석화 (인)

위 원 고영학 (인)



## **Abstract**

# **Hyaluronic Acid Nanocomposite Hydrogels via *In situ* Precipitation Process for Biomedical Applications**

Seol-Ha Jeong

Department of Materials Science and Engineering

Seoul National University

Hyaluronic acid (HAc) hydrogels offer many advantages as tissue engineering scaffolds, including excellent biocompatibility and biodegradability. However, these hydrogels have limited biomedical applications because of their poor biomechanical properties and rapid enzymatic degradation. Thus, it is essential to understand the effect of modifying the chemical structure of HAc via crosslinking reactions or of fabricating nanocomposite systems on the properties of the resulting hydrogels. In this work, we developed an *in situ* precipitation process to fabricate HAc–calcium phosphate (CaP) nanocomposite hydrogels after the formation of glycidyl methacrylate-conjugated HAc hydrogels via photo-crosslinking to improve the mechanical and biological properties of HAc hydrogels. Our process facilitates

the rapid incorporation of CaP nanoparticles with excellent uniformity and minimal agglomeration into a polymer matrix. We systematically compared our nanocomposite system with one fabricated using simple mixing based on the relationship between the hydrogel structure and rheological properties. Compared with pure HAC, the nanocomposite hydrogels showed improvement of not only the mechanical behavior but also the biostability under both *in vitro* and *in vivo* conditions. In addition, we demonstrate two potential applications of HAC-based nanocomposite hydrogels as injectable dermal fillers and wound dressing materials.

To evaluate the potential of the hydrogels for dermal filler applications, HAC–hydroxyapatite nanocomposite (HAC–nanoHAp) hydrogel fillers were prepared in particulated gel forms, and their properties were compared with those of pure HAp hydrogel fillers. Their rheological behavior, *in vivo* lateral diffusion under mouse skin, and effect on wrinkle improvement in a photo-aged mouse model were evaluated. The HAC–nanoHAp filler resulted in great improvement of the wrinkles because of its higher stiffness and gel cohesiveness compared with those of pure HAC. The strength of the dermal matrix was also greatly enhanced using HAC–nanoHAp, as it stimulated the synthesis of extracellular matrix such as collagen and elastin fibers. Thus, the HAC–nanoHAp filler shows great potential as a soft tissue augmentation product by improving the biophysical and biological performance of skin tissue.

To evaluate the potential of the hydrogels for wound dressing applications, another nanocomposite hydrogel containing calcium fluoride (CaF<sub>2</sub>) was introduced. CaF<sub>2</sub> particles, which are known to exhibit good antibacterial activity, were uniformly embedded within the HAc-based hydrogel using the *in situ* precipitation process. By varying the concentrations of the CaCl<sub>2</sub> and NH<sub>4</sub>F solutions as well as the precipitation time, we obtained hydrogels with different morphologies of CaF<sub>2</sub> particles and different ion-release profiles. Colony tests and live/dead assays using *Escherichia coli* and *Staphylococcus aureus* were employed to evaluate the antibacterial capabilities of the CaF<sub>2</sub> composite hydrogels. Regardless of the bacteria type, a significantly lower density of bacteria was observed on the CaF<sub>2</sub> nanocomposite hydrogels. In addition to their good antibacterial effect, improvement of cellular responses such as cell attachment and proliferation were also achieved for the CaF<sub>2</sub> nanocomposite hydrogels. Furthermore, the excellent wound healing efficiency of these nanocomposite hydrogels was demonstrated using an *in vitro* cell migration assay. Finally, the accelerated wound healing capability of the CaF<sub>2</sub> nanocomposite hydrogels was demonstrated by examining the wound closure changes over time using a full-thickness wound in a rat model compared with those for the pure hydrogel. Based on our findings, the CaF<sub>2</sub> nanocomposite hydrogel shows great potential for application as an advanced hydrogel wound dressing with both antibacterial and accelerated wound healing effects.

**Keywords:** Hyaluronic acid, Nanocomposite hydrogel, *In situ* precipitation, Hydroxyapatite, Calcium fluoride, Injectable dermal filler, Wound dressing, Biocompatibility, Antibacterial

**Student Number:** 2014-30215

# Contents

<b>Abstract</b> .....	i
<b>List of Tables</b> .....	viii
<b>List of Figures</b> .....	ix

## Chapter 1. Introduction

1.1. Hydrogel scaffolds for soft tissue engineering .....	2
1.2. Nanocomposite hydrogels.....	2
1.3. <i>In situ</i> precipitation process .....	3

## Chapter 2. *In situ* Precipitation of Hyaluronic Acid

### Nanocomposite Hydrogels

2.1. <i>In Situ</i> Precipitation of Hyaluronic Acid–Calcium Phosphate Nanocomposite Hydrogels .....	6
2.1.1. Introduction.....	6
2.1.2. Experimental Procedures .....	8
2.1.3. Results.....	14
2.1.4. Discussion .....	20
2.1.5. Conclusion .....	27

2.2. Mechanically Enhanced Hyaluronic-Acid-Based Nanocomposite Hydrogels via Dual-Crosslinking .....	46
2.2.1. Introduction.....	46
2.2.2. Experimental Procedures .....	47
2.2.3. Results.....	50
2.2.4. Discussion .....	54
2.2.5. Conclusion .....	56

## **Chapter 3. Hyaluronic Acid–Hydroxyapatite Nanocomposite**

### **Hydrogels for Injectable Dermal Fillers**

3.1. Introduction.....	69
3.2. Comparison between Hyaluronic Acid–Hydroxyapatite Composite Hydrogels Dermal Fillers.....	73
3.2.1. Introduction.....	73
3.2.2. Experimental Procedures .....	73
3.2.3. Results and Discussion .....	77
3.2.4. Conclusion .....	84
3.3. Wrinkle Improvement Using Hyaluronic Acid–Hydroxyapatite Nanocomposite Hydrogel Fillers .....	94

3.3.1. Introduction.....	94
3.3.2. Experimental Procedures .....	94
3.3.3. Results.....	99
3.3.4. Discussion .....	105
3.3.5. Conclusion .....	108

**Chapter 4. Hyaluronic Acid–Calcium Fluoride  
Nanocomposite Hydrogels for Advanced Antibacterial  
Wound Dressings**

4.1. Introduction.....	124
4.2. Experimental Procedures .....	125
4.3. Results.....	130
4.4. Discussion .....	133
4.5. Conclusion .....	135

**Chapter 5. Conclusion**

5.1. Conclusion .....	150
5.2. Further works .....	151

<b>References .....</b>	<b>153</b>
-------------------------	------------

<b>Abstract (Korean).....</b>	<b>169</b>
-------------------------------	------------

## List of Tables

**Table 1. Theoretical and actual CaP content of pHAc–CaP hydrogels with the corresponding amounts of the two reactants, CaCl<sub>2</sub> and H<sub>3</sub>PO<sub>4</sub>**

**Table 2. Water content of fully hydrated nanocomposite hydrogels as a function of CaP content**

**Table 3. Fitting values for net energy change of a chain segment after adsorption ( $\Delta E_{ad,total}/k_B T$ ) and activation length on the order of the displacement required to detach the absorbed segment from the particle surface ( $\delta$ )**

**Table 4. Mechanical properties of hydrogels crosslinked by either single- or dual-crosslinking with Ca<sup>2+</sup>**

**Table 5. Water content of pure HAc, HAc–microHAp, and HAc–nanoHAp fillers**

## List of Figures

**Figure 2.1.1. Schematic diagram of *in situ* precipitation of pHAc–CaP hydrogels.**

**Figure 2.1.2. Cross-sectional morphologies of (a) pure HAc and (b) pHAc–30 wt% CaP hydrogels and surface morphologies of (c) pure HAc and (d) pHAc–30 wt% CaP hydrogels at high magnification ( $\times 30k$ ).**

**Figure 2.1.3. Surface morphologies of (a) pHAc–10 wt% CaP, (b) pHAc–30 wt% CaP, and (c) pHAc–50 wt% CaP hydrogels at high magnification ( $\times 30k$ ).**

**Figure 2.1.4. Representative TEM image of CaP nanoparticles in pHAc–CaP hydrogels with EDS mapping analysis (inset: SAED patterns of CaP nanoparticles).**

**Figure 2.1.5. XRD patterns of (a) as-prepared pure HAc hydrogel, (b) as-prepared pHAc–CaP hydrogel, and (c) pHAc–CaP hydrogel after heat treatment at 1100 °C.**

**Figure 2.1.6. Rheological behavior of pHAc–CaP hydrogels: (a)  $G'$  as a function of frequency for various CaP contents and (b) complex viscosity as a function of frequency.**

**Figure 2.1.7. (a)  $G'$  of pure HAc, pHAc–30 wt% CaP, and mHAc–30 wt% CaP**

hydrogels as a function of frequency. (b)  $G'$  of pure HAc, pHAc–30 wt% CaP, and mHAc–30 wt% CaP hydrogels as a function of strain.

**Figure 2.1.8.** Swelling ratios of the hydrogels after immersion for 24 h in PBS at 37 °C.

**Figure 2.1.9.** *In vitro* enzymatic degradation behavior of pure HAc, mHAc–CaP, and pHAc–CaP hydrogels: (a) comparison of degradation rates as a function of incubated time and (b) remaining weight after 4 h of degradation with CaP content.

**Figure 2.1.10.** *In vitro* cellular response of pure HAc and pHAc–CaP hydrogels: (a) representative CLSM images of L929 fibroblasts cultured on pure HAc and pHAc–CaP hydrogels for 3 days and (b) cell viability of pure HAc and pHAc–CaP hydrogels measured by MTS assay after 3 and 5 days.

**Figure 2.1.11.** *In vivo* enzymatic degradation behavior of pure HAc and pHAc–CaP hydrogels: (a) histological images of pure HAc (top) and mHAc–30 wt% CaP hydrogel (bottom) stained by Alcian blue 4 weeks after implantation and (b) remaining area ratio of pure HAc and pHAc–30 wt% CaP hydrogels 4 and 8 weeks after implantation.

**Figure 2.1.12.** *In vivo* bioactivity test of hydrogel injection on subcutaneous

tissue of SD rat: histological images (left) of (a) pure HAc and (b) pHAc–30 wt% CaP hydrogel stained by MT 4 weeks after implantation and high-magnification images (right) of the histological images.

**Figure 2.1.13.** Schematic diagram of the composite hydrogel models with CaP nanoparticles showing two representative volume element models with and without CaP nanoparticles in the unit.

**Figure 2.1.14.** Schematic illustration (left) and surface morphology (right) of (a) pHAc–30 wt% CaP and (b) mHAc–30 wt% CaP hydrogels.

**Figure 2.2.1.** Fabrication of hydrogels using single crosslinking and dual crosslinking.

**Figure 2.2.2.** Cross-sectional images of single-CL and dual-CL hydrogels.

**Figure 2.2.3.** (a) Rheological behaviors ( $G'$ ,  $G''$ ) of HAc and HAc–CaP hydrogels crosslinked by single- or dual-crosslinking using  $\text{Ca}^{2+}$  ions in frequency sweep and (b)  $G'$  at 1 Hz of single- or dual-CL hydrogels.

**Figure 2.2.4.** Compression properties of single- and dual-CL hydrogels: (a) stress–strain curves of HAc and HAc–CaP hydrogels crosslinked by single- or dual-crosslinking using  $\text{Ca}^{2+}$  ions until gel fracture and (b) cyclic test until 50%

**compression.**

**Figure 2.2.5. (a) Optical images and (b) swelling ratio of single- and dual-CL hydrogels.**

**Figure 2.2.6. (a) Osteoblast cell attachment and (b) MTS proliferation assay after 3 and 5 days of culturing on HAC–CaP hydrogels. (c) Schematic diagrams of cell differentiation tests: (i) seeded on the surface of hydrogels and (ii) cultured in ion-release medium. ALP activity of osteoblasts cells (d) on the surface of HAC–CaP hydrogels and (e) in the ion-release medium after 7 days of culturing.**

**Figure 2.2.7. Pre-treatment effects at different pH:  $G'$  at 1 Hz of dual-CL HAC–CaP hydrogels compared with that of single-CL HAC–CaP hydrogel.**

**Figure 2.2.8. (a) TGA curves of single- and dual-CL HAC–CaP hydrogels. (b) TEM and EDS mapping images of inorganic CaP nanoparticles in HAC–CaP hydrogels after dual-crosslinking using ionic solutions containing (a)  $\text{Ca}^{2+}$ , (b)  $\text{Ba}^{2+}$ , and (c)  $\text{Sr}^{2+}$  (scale bar = 250 nm).**

**Figure 2.2.9. Swelling ratio profile of single- and dual-CL HAC–CaP hydrogels.**

**Figure 3.1.1. Objectives for development of highly functional nanocomposite**

hydrogels for injectable dermal filler applications.

**Figure 3.2.1. Surface morphologies of (a) pure HAc, (b) HAc–microHAp, and (c) HAc–nanoHAp and (d) a high-magnification image of HAc–nanoHAp ( $\times 30k$ ).**

**Figure 3.2.2.  $G'$  of pure HAc, HAc–microHAp, and HAc–nanoHAp as a function of frequency.**

**Figure 3.2.3. Axial T2 images of (a) pure HAc, (b) HAc–microHAp, and (c) HAc–nanoHAp at 0, 4, and 12 weeks after filler injection.**

**Figure 3.2.4. Remaining gel volume as a function of time until 12 weeks based on MRI volumetric analysis.**

**Figure 3.2.5. (a) *In vitro* cell attachment images of pure HAc, HAc–microHAp, and HAc–nanoHAp using L929 fibroblast cells. First and second row scale bars = 50 and 20  $\mu\text{m}$ , respectively. (b) Cell viability after 4 days of culturing on pure HAc, HAc–microHAp, and HAc–nanoHAp (\* $P < 0.05$ ).**

**Figure 3.2.6. Filler morphological analysis by H&E staining at 8 weeks. Scale bars = 100  $\mu\text{m}$ .**

**Figure 3.2.7. (a) Analysis of dermis thickness using H&E staining at 12 weeks.**

Scale bars = 100  $\mu\text{m}$ . (b) Analysis of dermal thickness using ImageJ (\*\*P<0.01).

Figure 3.2.8. (a) Analysis of collagen distribution using MT staining at 12 weeks.

Scale bars = 100  $\mu\text{m}$ . (b) Analysis of collagen area in the dermis (\*P<0.05, \*\*P<0.01). (c) Procollagen gene expression at 8 weeks (\*\*P<0.01, #P<0.5).

Figure 3.3.1. Cross-sectional SEM images of (a) pure HAc with high porosity and (b) HAc–nanoHAp. High-magnification images of (c) pure HAc with a smooth surface and (d) HAc–nanoHAp containing uniformly distributed HAp nanoparticles.

Figure 3.3.2. (a) Photographs of fillers on the rheometer plate. G' of fillers as a function of (b) angular frequency and (c) strain. (d) Axial force graph of fillers in unconfined mode under compression.

Figure 3.3.3. G' and cohesivity index of commercial filler products and HAc–nanoHAp to illustrate their lifting capacities.

Figure 3.3.4. (a) T2 parametric images showing fillers and dermal tissue modification and lateral diffusion of fillers over 7 days. (b) Lateral diffusion ratio and (c) T2 relaxation time graph of fillers over time.

Figure 3.3.5. (a) H&E stained image showing shallow and deep wrinkles. (b)

**Illustration of skin layer components obtained using Image J. Scale bar = 500  $\mu\text{m}$ . (c) Constitutive parameters for each skin layer and simulation conditions. (d) Mesh-generated image of each skin layer and injected filler.**

**Figure 3.3.6. Color plot of logarithmic strain distribution after simulation for pure HAc and HAc–nanoHAp, showing the gel stiffness effect on wrinkle improvement after loading a normal force on the skin to observe filler deformation in accordance with wrinkle deformation. The red arrow indicates the direction of filler deformation.**

**Figure 3.3.7. Examination of wrinkles using skin replica: (a) UVB-treated, (b) pure-HAc-filler-treated, (c) HAc–nanoHAp-filler-treated, and (d) untreated samples. (e) Mean wrinkle depth calculated from histological images. (\* $P < 0.05$ ).**

**Figure 3.3.8. Images stained with H&E stain (100 $\times$ ): (a) UVB-treated, (b) pure-HAc-filler-treated, (c) HAc–nanoHAp-filler-treated, and (d) untreated skin. (e) Quantification of dermal thickness (\*\*  $P < 0.01$ ).**

**Figure 3.3.9. Collagen fiber formation in the dermis observed from images stained with MT stain (100 $\times$ ): (a) UVB-treated, (b) pure-HAc-filler-treated, (c) HAc–nanoHAp-filler-treated, and (d) untreated skin. (e) Quantification of collagen fiber area from MT stained images (\*  $P < 0.05$ ).**

**Figure 3.3.10. Elastic fiber formation in the dermis observed from images stained with Verhoeff–Van Gieson (100x): (a) UVB-treated, (b) pure-HAc-filler-treated, (c) HAc–nanoHAp-filler-treated, and (d) untreated skin. (e) Quantification of elastic fiber area (\* P < 0.05, \*\* P < 0.01).**

**Figure 3.3.11. Procollagen level of untreated, UVB-treated, pure-HAc-treated, and HAc–nanoHAp-treated skin 4 weeks after injection (\* P < 0.05, \*\* P < 0.01).**

**Figure 3.3.12. Observation of vimentin in (a) pure HAc and (b) HAc–nanoHAp by immunostaining (scale bar = 100  $\mu$ m). (c) Quantitative vimentin area at week 1, 4, and 12.**

**Figure 3.3.13. TEM images of dermis after treatment with (a) pure HAc and (b) HAc–nanoHAp showing the higher density of collagen in highly organized forms following HAc–nanoHAp filler injection.**

**Figure 4.1. Schematic illustration of fabrication of CaF<sub>2</sub> composite hydrogel via *in situ* precipitation process.**

**Figure 4.2. SEM images of (a) pure gel and (b) CaF<sub>2</sub> composite gel and high-magnified images of (c) pure gel and (d) CaF<sub>2</sub> composite gel.**

**Figure 4.3. EDS mapping images and elemental analysis of CaF<sub>2</sub> composite gels**

for precipitation times of 10 min, 30 min, and 1 h.

**Figure 4.4. XRD patterns of CaF<sub>2</sub> composite gels for precipitation times of 10 min, 30 min, and 1 h.**

**Figure 4.5. Fluoride ion release profiles of CaF<sub>2</sub> composite gels for precipitation times of 10 min, 30 min, and 1 h.**

**Figure 4.6. Rheological behavior of pure gel and CaF<sub>2</sub> composite gel in frequency sweep mode.**

**Figure 4.7. Live/dead assay images: Live and dead E. coli on the (a) pure gel and (b) CaF<sub>2</sub> composite gel. Live and dead S. aureus on the (c) pure gel and (d) CaF<sub>2</sub> composite gel.**

**Figure 4.8. Colonies of E. coli on the (a) pure gel and (b) CaF<sub>2</sub> composite gel and colonies of S. aureus on the (c) pure gel and (d) CaF<sub>2</sub> composite gel.**

**Figure 4.9. (a) CLSM images of L929 fibroblasts cultured on pure gel and CaF<sub>2</sub> composite gel after 2 days. (b) Cell viability of pure gel and CaF<sub>2</sub> composite gel measured by MTS assay after 3 and 5 days.**

**Figure 4.10. *In vitro* HUVEC migration test using pure gel and CaF<sub>2</sub> composite gel.**

**Figure 4.11. *In vivo* animal test results: (a) optical images showing wound closure and (b) wound closure over time for untreated wound and wounds treated with pure gel and CaF<sub>2</sub> composite gel up to day 6.**

**Figure 4.12. H&E stained images for (a) untreated wound and wounds treated with (b) pure hydrogel and (c) CaF<sub>2</sub> composite hydrogel at day 7 and (d) untreated wound and wounds treated with (e) pure hydrogel and (f) CaF<sub>2</sub> composite hydrogel at day 7 day 14.**

**Figure 5. Various applications of HAc based nanocomposite hydrogels for further works.**

# **Chapter 1.**

## **Introduction**

## **1.1. Hydrogel scaffolds for soft tissue engineering**

The aim of tissue engineering is generally to restore, preserve, or replace biological tissues for a wide range of regenerative medical applications [1]. For tissue engineering to be successful, the design of an appropriate scaffold is critical [2, 3]. Biomaterial scaffold materials must be biocompatible, biodegradable, and biomechanically stable [4]. In other words, the scaffolds should possess several functions to promote cell proliferation and differentiation, thereby leading to tissue formation, while also being biodegradable to allow the infiltration of cells and tissues. The mechanical properties of the scaffold can also affect the cellular environment. Hydrogel-based scaffolds have attracted considerable attention for tissue engineering, especially for soft tissue engineering applications because they resemble the natural extracellular matrix (ECM) microenvironment and provide desirable frameworks for cellular organization and tissue constructs [5, 6]. In addition, hydrogels consist of a hydrated network of crosslinked polymers; their mechanical and chemical properties can thus be easily tuned by adjusting the crosslinking density, introducing reactive moieties, or tethering biofunctional molecules [7].

## **1.2. Nanocomposite hydrogels**

To extend and customize the functionality of hydrogel scaffolds, an approach to

fabricate “nanocomposite hydrogels” has recently emerged for various biomedical applications [8]. The incorporation of nanoparticles such as metallic/metal-oxide-based (silver, gold, iron oxide, titania, alumina, zirconia) [9], ceramic (hydroxyapatite (HAp), silicate, silica, calcium phosphate, bioactive glasses) [10], polymeric [11], and carbon-based nanomaterials [12] into nanocomposite hydrogels can result in superior properties, including a mechanically reinforced gel matrix, stimuli-responsive properties, enhanced biocompatibility, and a controlled drug delivery system [13]. The improved performance of the nanocomposite hydrogels is mostly attributed to the high level of interaction between the polymer chains and nanoparticles. Thus, the design of fabrication methods to prepare desired nanocomposite hydrogel systems is critical.

A general and simple approach to prepare nanocomposite hydrogels is to create a nanoparticle suspension in a hydrogel-forming solution before gelation, which is called “simple mixing” [14]. However, this approach has several drawbacks such as the low level of interaction between the polymer chains and nanoparticles [15] and aggregation of nanoparticles within the hydrogel networks [16, 17]. To overcome these issues, additional steps such as functionalization of the nanoparticles or polymer chains are needed.

### **1.3. *In situ* precipitation process**

Herein, we introduce an advanced procedure, called an “*in situ* precipitation process,” that produces uniform nanocomposite hydrogels with a high level of integration between the precipitated particles and hydrogel networks. Because hydrogels absorb a large amount of water, various solutes and ion fluxes are available through the gel matrix [18]. The ions can be easily transformed into particles by changing the environment (e.g., adjusting the pH). During this process, a uniform distribution of particles at the nanoscale within the gel matrix is expected. This precipitation process results in nanocomposite hydrogel systems with greatly improved mechanical properties and even enhanced biocompatibility. We present this approach for the precipitation of bioceramic nanoparticles within hyaluronic acid (HAc) hydrogels, which are representative hydrophilic polymers with high water uptake capability. In Chapter 2, HAc–calcium phosphate (CaP) nanocomposite hydrogel systems are introduced, and the enhancements of their mechanical properties and biocompatibility compared with those of nanocomposites fabricated using conventional methods are systematically evaluated. The applications of this system to injectable dermal fillers and hydrogel wound dressings are introduced in Chapter 3 and Chapter 4, respectively.

## **Chapter 2.**

# ***In situ* Precipitation of Hyaluronic Acid Nanocomposite Hydrogels**

## **2.1. *In situ* Precipitation of Hyaluronic Acid Nanocomposite Hydrogels**

### **2.1.1. Introduction**

Hyaluronic acid (HAc) is a polysaccharide consisting of alternating units of a repeating disaccharide,  $\beta$ -1,4-D-glucuronic acid - $\beta$ -1,3-N-acetyl-D-glucosamine [19]. HAc is an essential component of the ECM of connective tissues such as cartilage, the vitreous of the eye, synovial joint fluids, and dermal tissue [20-22]. Because of its hydrophilic and polyanionic macromolecule structure, it not only provides a hydrated environment for cell growth and tissue infiltration [23] but also plays an important role in lubrication [24]. This material also possesses excellent biological properties, including non-immunogenicity, biocompatibility, and biodegradability [25]. Thus, HAc has attracted considerable interest for use as a biomedical scaffold for various applications including arthritis treatment [20], soft tissue augmentation and replacement [26-28], cartilage [29] or bone repair substitutes [30], ophthalmic surgery [31, 32], and drug delivery [33]. However, in its natural state, HAc is rapidly turned over under physiological condition via enzymatic or free radical degradation; thus, it lacks the robustness and stability needed in biomedical scaffolds [34-37]. To improve its mechanical properties and biostability,

various crosslinking strategies involving chemical modification or conjugation have been extensively explored [38-41].

Despite the development of HAC hydrogels using various crosslinking systems, improvements of their mechanical and biological properties are still limited. Thus, the introduction of different polymeric materials or bioactive nanoparticles to create HAC nanocomposite hydrogel systems has been highlighted for functional biomaterial applications [42-45]. For example, the incorporation of silica nanoparticles into HAC hydrogels has resulted in mechanical improvement and high stability [46]. In another study, improvement of the mechanical properties of a HAC nanocomposite system was reported after the incorporation of functionalized nanosized calcium phosphate (CaP) particles [47]. These nanocomposite hydrogels are generally fabricated using simple physical mixing of the inorganic particles with the HAC solution before crosslinking. However, agglomeration or aggregation of nanoparticles during this mixing often leads to morphological inhomogeneity in the overall structure. Thus, a new methodology to fabricate uniform and homogenous nanocomposite hydrogels is needed.

In our work, we employed an *in situ* precipitation process that combines the principle of ion diffusion through the hydrogel, which can absorb a large amount of water, with the facile synthesis of inorganic phases through precipitation. In fact, *in*

*situ* precipitation has been shown to be effective in generating uniformly distributed CaP nanoparticles in alginate-based biofilms [48, 49] and chitosan hydrogels [50], with remarkable enhancements of the mechanical and biological performance of the nanocomposite systems. However, the *in situ* precipitation process has not yet been implemented for HAc hydrogels. In our work, HAc–CaP nanocomposite hydrogels were fabricated using an *in situ* precipitation process. The surface morphologies and chemical compositions of the nanocomposite hydrogels were evaluated and compared with those of a hydrogel formed using simple mixing to determine the relationship between the mechanical improvement and hydrogel structure. Finally, the *in vitro* and *in vivo* biological performances were investigated to evaluate the potential of this system for tissue engineering applications.

## **2.1.2. Experimental procedures**

### **Fabrication of nanocomposite hydrogels via *in situ* precipitation**

HAc hydrogels were prepared using a typical photo-crosslinking system, following previously established protocols [51]. Briefly, to obtain glycidyl methacrylated HAc (GMHAc), 1 w/v% HAc with a molecular weight of 1.8–2.5 MDa (Bioland, Seoul, Korea) was dissolved in 100 mL of phosphate-buffered saline (PBS). Then, 2.2 v/v% of triethylamine and glycidyl methacrylate and 2.2 w/v% of tetrabutylammonium bromide were added to the HAc solution. After stirring

overnight at room temperature to obtain a homogenous mixture, the GMHA conjugates in solution were precipitated by adding acetone and were then cleaned with distilled water to remove excess reactants. The GMHAc precipitates were then redissolved in distilled water and exposed to ultraviolet (UV) light for 15 min with a photoinitiator (2-hydroxy-4'-(2-hydroxyethoxy)-2-methylpropiophenone, Irgacure 2959). The hydrogels were subsequently soaked overnight in a mixture of  $\text{CaCl}_2$  and  $\text{H}_3\text{PO}_4$  with a Ca/P ratio of 1.67; this process is referred to as an “ion permeation process”. The amounts of the two reactants were varied to yield CaP contents ranging from 10 to 40 wt% (**Table 1**), with the products called ‘pHAc–10, 20, 30, or 40 wt% CaP’. These hydrogels were then subjected to the *in situ* precipitation process. They were immersed in 15%  $\text{NH}_4\text{OH}$  solution for 3 h to precipitate CaP particles within the hydrogels. The final products of the nanocomposite hydrogels were dialyzed in a PBS solution to remove the remnants. A schematic diagram of the *in situ* precipitation process for the fabrication of the HAc–CaP nanocomposite hydrogels is presented in **Figure 2.1.1**. The samples prepared by the *in situ* precipitation process and simple mixing were designated as pHAc–CaP and mHAc–CaP, respectively.

### **Characterization of hydrogels**

All the samples were lyophilized overnight to maintain their structures, and the

surface morphologies were then examined using field-emission scanning electron microscopy (FE-SEM, SUPRA 55VP, Carl Zeiss Co., Germany). The chemical compositions of the precipitated nanoparticles in the hydrogels were evaluated using transmission electron microscopy (TEM, Tecnai F20, FEI Co., USA). During the fabrication process, 400-mesh copper grids were placed in the pHAc–CaP hydrogels, which were dried in air for 2 days. The phase of the precipitated CaP was analyzed using X-ray diffraction (XRD, D8-Advance, Bruker Co., Germany). Samples for three different conditions were prepared: pure HAc hydrogel, pHAc–30 wt% CaP before heat treatment, and pHAc–30 wt% CaP after heat treatment at 1100°C for 5 min. XRD data were obtained from 20° to 60° (2 $\theta$ ) using CuK $\alpha$  radiation at a scan rate of 1°/min. The actual CaP content was quantified using thermogravimetric analysis (TGA, Discovery TGA, TA instruments Co., USA), and the results showed good agreement with the theoretical content (**Table 1**). Before the analysis, all the hydrogel samples were completely dried in air and heated to 1100°C at a rate of 10°C/min under a N<sub>2</sub> atmosphere.

### **Rheological properties of hydrogels**

The rheological behavior of the hydrogels was assessed using a controlled strain rheometer (ARES, Rheometric Scientific, USA). Hydrogel samples with diameters of 25 mm and thicknesses of 2 mm were prepared for the analysis. Frequency sweeps

were performed in the angular frequency range of 0.1 to 100 rad/s at a strain of 1% in the linear region to measure the mechanical properties, including the storage ( $G'$ ) and loss ( $G''$ ) moduli and the complex viscosity. Strain sweeps were also performed in the range of 0.01% to 100% of strain at a fixed frequency of 6.28 rad/s (1 Hz).

### **Swelling properties of hydrogels**

The equilibrium swelling ratios of the hydrogels were evaluated in a PBS solution at 37°C. The hydrogels were dried in a vacuum oven and weighed to determine the initial weight ( $W_i$ ). They were then immersed in PBS for 24 h and reweighed to determine the hydrated weight ( $W_h$ ). The swelling ability of the hydrogels was calculated using the following equation:

$$\text{Swelling ratio } \left(\frac{g}{g}\right) = (W_h - W_i / W_i),$$

where  $W_i$  and  $W_h$  represent the initial dried weight and hydrated weight, respectively.

### ***In vitro* degradation tests of hydrogels**

*In vitro* degradation tests of the hydrogels were performed in a PBS solution at 37°C with hyaluronidase (Type I-S, lyophilized powder, 400–1000 UI/mg solid, Sigma Co., Korea) at a concentration of 500  $\mu\text{g/mL}$  (200–500 UI/mL). The degradation rates for the hydrogels were determined by immersing them in the hyaluronidase solution for predetermined periods and measuring the weight changes

using the following equation:

$$\text{Remaining weight ratio (\%)} = \left( \frac{W_r}{W_i} \right) \times 100,$$

where  $W_i$  and  $W_r$  represent the initial and remaining weight, respectively.

### ***In vitro* cell tests of hydrogels**

The L929 fibroblast cell line (derivative of strain L, *Mus musculus*, mouse) was used to assess the cellular responses on the hydrogels. Before cell seeding, the samples were washed with 70% ethanol and PBS solution and sterilized on a clean bench under UV irradiation. The pre-incubated cells were seeded on the hydrogels at densities of  $5 \times 10^4$  cells/mL for the cell attachment test and  $2 \times 10^4$  cells/mL for the cell proliferation test. The cells were cultured in alpha-minimum essential medium ( $\alpha$ -MEM, Welgene Co., Ltd., Korea) supplemented with 10% fetal bovine serum (FBS) and 1% penicillin–streptomycin in a humidified incubator with 5% CO<sub>2</sub> at 37°C. The cell attachments were visualized using confocal laser scanning microscopy (CLSM, FluoView FV1000, Olympus, Japan) after culturing for 3 days. Before visualization, the cultured cells on the samples were fixed in 4% paraformaldehyde in PBS for 10 min, washed 3 times with PBS solution, and then permeabilized with 0.1% Triton X-100 in PBS for 5 min and 1% BSA in PBS for 30 min. The cells on the samples were then stained with fluorescent phalloidin for 20 min and with 4', 6-diamidino-2-phenylindole (DAPI) for 5 min before examination

of cell morphology on the sample surface. The level of cell proliferation was measured using the methoxyphenyl tetrazolium salt (MTS) assay (CellTiter 96 Aqueous One Solution, Promega, USA) after 3- and 5-day culturing of cells on the surfaces of the hydrogels.

### ***In vivo* biological performance of hydrogels**

Animal tests were performed to examine the *in vivo* biological performance after implanting pure HAc and pHAc–30 wt% CaP hydrogels under intramuscular sites of 6-week-old Sprague Dawley (SD) rats. The use and handling of the animals in the study followed the Guide for the Care and Use of Laboratory Animals of Seoul National University, and the tests were performed according to protocol No. 15-0075 approved by the Institutional Animal Care and Use Committee (IACUC) of Seoul National University. The dorsal skin of the rats was incised using a surgical blade, and 0.4 mL of disc-shaped hydrogels was implanted. The rats were sacrificed 4 or 8 weeks after implantation. The tissues extracted with the hydrogels were fixed in 10% formalin, gradually dehydrated with ethanol, and embedded in paraffin for histological analysis. The prepared paraffin blocks were cut into 4- $\mu$ m-thick sections along the longitudinal axis of the hydrogels, which was perpendicular to the skin surface. The slices were stained with Alcian blue to detect the remnants of the HAc-based hydrogels in the implanted region. The *in vivo* stability of the hydrogels was

evaluated by calculating the remaining amount of hydrogel by normalizing the cross-sectional area of the hydrogels using the computerized image analysis system SPOT (Diagnostic Instruments, Inc., MI, USA). The *in vivo* biocompatibility of the hydrogels was also assessed histologically after Masson's trichrome (MT) staining.

### **Statistical analysis**

All the experimental results are expressed as the mean  $\pm$  standard deviation, and the difference between the two groups was determined using a one-way analysis of variance (ANOVA), with  $p < 0.05$  and  $p < 0.01$  considered statistically significant (\* $p < 0.05$  and \*\* $p < 0.01$ ).

## **2.1.3. Results**

### **Characterization of pHAc–CaP hydrogels**

The pure HAc hydrogels typically had porous microstructures with pore sizes of 200–500  $\mu\text{m}$ , as observed in **Figure 2.1.2a**. The pHAc–30 wt% CaP hydrogels also exhibited a highly porous structure with interconnected pores, implying that the network structure of the hydrogel was maintained after the *in situ* process (**Figure 2.1.2b**). Significant differences in the surface morphologies of the pure HAc and pHAc–CaP hydrogels are clearly observed in the high-magnification images. A smooth surface matrix was observed for the pure HAc hydrogel (**Figure 2.1.2c**),

whereas a nano-roughened surface with 200–350 nm spherical nanoparticles was observed for the hydrogels containing 30 wt% CaP (**Figure 2.1.2d**). Similar to the pHAc–30 wt% CaP hydrogel, a dense and uniform distribution of spherical CaP nanoparticles was observed throughout the HAc matrix without any agglomeration for the pHAc–CaP hydrogels with different CaP contents (**Figure 2.1.3**).

Highly spherical CaP nanoparticles with a uniform size of 200 nm are observed in the TEM micrographs of the pHAc–CaP hydrogels in **Figure 2.1.4**. In addition, the selected-area electron diffraction (SAED) pattern reveals the presence of an amorphous phase of the CaP nanoparticles. The nanoparticles contained Ca, P, and O according to the energy-dispersive X-ray spectroscopy (EDS) mapping results. Quantitative EDS analyses of these nanoparticles also indicated a composition of 18 at.% Ca–17 at.% P–65 at.% O, implying that the expected Ca/P ratio of the CaP precipitates was approximately 1.05. The composition and phase of the nanoparticles were also identified through XRD analysis, as shown in **Figure 2.1.5**. The XRD pattern of the pure HAc hydrogel contained no significant peaks (**Figure 2.1.5a**). In contrast, a broad peak at approximately 32° to 35° was identified in the XRD pattern of the nanocomposite hydrogels (**Figure 2.1.5b**), indicating that the precipitated CaP particles had low crystallinity during the *in situ* precipitation process. When the composites were heat treated at 1100°C in air, two sharp peaks appeared for Ca<sub>2</sub>P<sub>2</sub>O<sub>7</sub> and Ca<sub>3</sub>(PO<sub>2</sub>)<sub>2</sub>, as observed in **Figure 2.1.5c**, indicating a Ca/P ratio of 1–1.5, which

agrees well with the EDS mapping data from the TEM images.

### **Mechanical properties of pHAc–CaP hydrogels**

The mechanical properties of pHAc–CaP hydrogels with various CaP contents were investigated using a strain-controlled rheometer, and the results are presented in **Figure 2.1.6**.  $G'$  of pHAc–CaP was significantly increased compared with that of the pure HAc hydrogel. In addition, with increasing CaP content up to 40 wt%,  $G'$  increased steadily, as observed in **Figure 2.1.6a**.  $G'$  of pHAc–CaP and pure HAc exhibited frequency-independent and frequency-dependent behaviors, respectively, meaning that the elasticity of the HAc hydrogel was markedly enhanced by the incorporation of the CaP nanoparticles through the *in situ* process. The results of the complex viscosity measurements are presented in **Figure 2.1.6b**. All of the hydrogels exhibited shear thinning phenomena under deformation. The complex viscosities of the pHAc–CaP hydrogels were considerably higher than those of the pure HAc hydrogels at all the shear rates. Furthermore, the concentration of CaP had a positive effect on the viscosity at low frequencies. These results imply the strong integration of the CaP nanoparticles with the HAc matrix after the *in situ* precipitation process.

The viscoelastic behavior of the hydrogel systems was examined by performing both frequency sweep and strain sweeps, and the results were compared with those

of the mHAc–CaP system (**Figure 2.1.7**).  $G'$  of the pure HAc hydrogel showed a frequency-dependent elastic behavior, whereas that of the nanocomposites was relatively constant. More interestingly, the  $G'$  values of pHAc–CaP were consistently approximately 5 times larger than those of mHAc–CaP.

### ***In vitro* biostability of hydrogels**

The swelling behaviors of the pure HAc, pHAc–CaP, and mHAc–CaP hydrogels are shown in **Figure 2.1.8**. The equilibrium swelling ratio of the pure HAc hydrogel was approximately 110, whereas those of the nanocomposite hydrogels decreased with increasing CaP content. The amount of water influx in the pHAc–CaP hydrogels was thus significantly lower than that in the mHAc–CaP hydrogels. The water contents of the fully hydrated nanocomposite hydrogels as a function of CaP content are listed in **Table 2**.

The *in vitro* biodegradability of the hydrogels was assessed by monitoring the weight change as a function of incubation time, and the results are presented in **Figure 2.1.9a**. As expected, degradation of the pure HAc hydrogels occurred most rapidly. The pHAc–CaP hydrogels showed improved resistance to enzymatic degradation compared with pure HAc and mHAc–CaP with the same CaP content. After 2 days, 40 wt% of pHAc–CaP still remained, with the shape of the hydrogel maintained, whereas both pure HAc and mHAc–CaP were completely degraded. The

optical images of the remnant hydrogels after degradation clearly demonstrate that the pHAc–CaP hydrogels exhibited superior biostability. The degradation ratios for pHAc–CaP as a function of the CaP content were also compared by calculating the relative remaining weight after 4 h of enzymatic degradation (**Figure 2.1.9b**). In the hyaluronidase solution, the pHAc–CaP hydrogels underwent less hydrolytic degradation, as increasing the CaP content led to less swelling.

### **Biological performance of pHAc–CaP nanocomposite hydrogels**

To evaluate the cytocompatibility of the pHAc–CaP nanocomposite hydrogels, cell tests were performed. The *in vitro* cellular responses of fibroblast cells on the hydrogels are presented in **Figure 2.1.10**. The fibroblasts on the pHAc–CaP hydrogels appeared more polarized and stretched compared with the round-shaped cells on the pure HAc hydrogels (**Figure 2.1.10a**). In addition, the cell spreading area of the nanocomposite hydrogels ( $\sim 400 \mu\text{m}^2$ ) was significantly larger than that of the pure HAc hydrogels ( $\sim 250 \mu\text{m}^2$ ). The cell spreading areas were comparable among the pHAc–CaP nanocomposites, with no significant differences detected. In addition, the cell densities on the pHAc–CaP hydrogel surfaces were higher than those on the pure HAc hydrogels, which agrees well with the cell densities determined using the MTS assay, as shown in **Figure 2.1.10b**. The level of fibroblast proliferation on the pHAc–CaP hydrogels after culturing for 5 days was

approximately 8 times higher than that on the pure HAc hydrogels, implying enhanced biocompatibility for the nanocomposite hydrogels.

Finally, we investigated the *in vivo* stability and bioactivity of the pHAc–CaP hydrogels based on volume retention and histological analysis, respectively, 4 and 8 weeks after implantation in subcutaneous sites in rats. The histological images of the hydrogel-tissue paraffin blocks were used to determine the amount of remaining hydrogels. As shown in **Figure 2.1.11a**, the thicknesses and diameters of the cross-sectioned pure HAc hydrogel decreased markedly, indicating that a large portion of the hydrogel was degraded in the body even 4 weeks after implantation. However, the pHAc–30 wt% CaP maintained its original shape with good structural integrity 4 and 8 weeks after implantation. The remaining area was quantified based on image analysis, as shown in **Figure 2.1.11b**. In addition, 4 weeks after implantation, only 20% of the pure HAc hydrogels remained in the body, whereas more than 50% of the pHAc–30 wt% CaP remained. After 8 weeks, the pure hydrogel was mostly degraded (10% remnant), in contrast to the approximately 50% remaining for the pHAc–CaP hydrogel.

The bioactivity of the hydrogel was evaluated using histological analyses. The collagen formation in the pHAc–CaP hydrogels observed by M&T staining was significantly greater than that of the pure HAc hydrogels, as shown in **Figure 2.1.12**, indicating that the CaP nanoparticles provide a highly effective microenvironment

for fibroblast cell proliferation and ECM production [52].

## **2.1.4. Discussion**

### **Enhancement of mechanical properties of pHAc–CaP hydrogels**

The development of a theoretical model that relates the viscoelastic behavior of pHAc–CaP hydrogels on a macroscopic scale to the structural morphology on a microscopic scale is of interest [53-57]. A rheological model was used to estimate the elastic behavior of HAc-based composite hydrogel systems in this work [55]. The effect of the binding energy on enhancing the mechanical properties of various nanocomposite hydrogel systems has been previously demonstrated [56-59]. For instance, the stiffness of a polylactic acid (PLA)–polyethylene glycol (PEG)–hydroxyapatite (HAp) composite hydrogel was remarkably improved by increasing the binding energy between HAp and polymers through surface modification of the HAp nanoparticles [55]. In this work, HAc molecules with a molecular weight of 3000 kDa were used. The repeat unit of HAc is a disaccharide comprised of D-glucuronic acid and N-acetyl-D-glucosamine with a length of 0.95 nm, radius of 0.5 nm, and molecular weight of 400 g/mol [60]. Therefore, the average number of monomers per HAc molecule is assumed to be 7500, with an estimated chain length of  $\sim 7 \mu\text{m}$ . At a crosslinking density of 1%, the estimated number of monomers per chain segment between crosslinking points is assumed to be 100. Thus, the Flory

radius ( $R_F$ ) of each HAc segment between crosslinking points should be  $\sim 15$  nm, which is much smaller than the average diameter of CaP nanoparticles (200 nm). Nanoparticles smaller than or similar to  $R_F$  of the HAc segments were not considered for this model. Therefore, based on the rheology model, each segment of the crosslinked gels with or without CaP nanoparticles was constructed as the representative volume element (RVE), as illustrated in **Figure 2.1.13**.

The total stress to the composite hydrogel systems is the sum of the stresses from two types of RVEs in the total volume with the numbers of each segment,  $N_{CPCS}$  and  $N_{FCS}$  (CPCS and FCS refer to CaP-absorbed chain segment and free chain segment, respectively):

$$\sigma_{tot} = N_{CPCS}\sigma_{CPCS} + N_{FCS}\sigma_{FCS}.$$

The stress tensors for both RVEs can be expressed using Kramers expression as follows:

$$\sigma_{CPCS} = 3G_{CPCS} \frac{\langle \mathbf{R}_{CPCS} \mathbf{R}_{CPCS} \rangle}{R_F}$$

$$\sigma_{FCS} = 3G_{FCS} \frac{\langle \mathbf{R}_{FCS} \mathbf{R}_{FCS} \rangle}{R_F},$$

where  $G_{CPCS}$  and  $G_{FCS}$  represent the stiffnesses of the two RVEs and  $\langle \mathbf{R}_{CPCS} \mathbf{R}_{CPCS} \rangle$  and  $\langle \mathbf{R}_{FCS} \mathbf{R}_{FCS} \rangle$  represent the average end-to-end distances of each segment after deformation compared with  $R_F$ , which is assumed to be the initial length of the segments. Under steady-state conditions, the model suggests the following stiffness

of CPCS:

$$G_{CPCS} = G_{FCS}^P \exp \left[ \frac{fN\Delta E_{ad} - \delta F_{CPCS}}{k_B T} \right] = G_{FCS}^P \exp \left[ \frac{\Delta E_{ad, total} - \delta F_{CPCS}}{k_B T} \right],$$

where  $G_{FCS}^P$  is the stiffness of the free chain portions within the absorbed chain segments,  $\Delta E_{ad}$  is the net energy change of an individual monomer after adsorption, with the fraction of absorbed monomers (f), number of monomers per a chain segment (N), and activation length on the order of the displacement required to detach the absorbed segment from the particle surface ( $\delta$ ) at the entropic force ( $F_{CPCS}$ ). The total net energy change of the absorbed chain segment is  $\Delta E_{ad, total}$ .

Assuming that composite hydrogels exhibit linear viscoelasticity under small deformation, the mechanical response of the hydrogels can be decoupled into rate-independent and rate-dependent components. For simplicity, in the strain rheometer tests, the time-independent part of the deformation ( $G'$ ) was only predicted with a small deformation,  $\lambda(t) = \lambda_0 \sin \omega t$ .  $F_{CPCS}$  was also estimated [55, 61] as follows:

$$F_{CPCS} = \frac{3k_B T}{R_F^2} \overline{R_{CPCS}} \left( 1 - \frac{\overline{R_{CPCS}}^2}{R_{CPCS, max}^2} \right)^{-1},$$

where  $\overline{R_{CPCS}} = \overline{\mathbf{F}} \cdot \mathbf{R}_F$  and  $\overline{\mathbf{F}}$  were obtained from the average values of the deformation gradient,  $\mathbf{F}$ , over one cycle of oscillation:

$$\mathbf{F} = \begin{pmatrix} 1 & \lambda_0 \sin \omega t & 0 \\ 0 & 1 & 0 \\ 0 & 0 & 1 \end{pmatrix}.$$

To predict  $G'$  of the composite hydrogel systems, a simple approximation was

applied assuming the isostrain case ( $n = 1$ ):

$$G'_{comp}(\omega) = \nu_{CPCS} G_{CPCS}'(\omega)^n + \nu_{FCS} G_{FCS}'(\omega)^n,$$

where  $\nu_{CPCS}$  and  $\nu_{FCS}$  are the volume fractions of each RVE.  $G_{FCS}(\omega)$  was obtained by fitting and calibrating the pure HAc hydrogel data, and the volume fractions of CaP nanoparticles for composite systems were calculated under the assumption that the density of the amorphous CaP nanoparticles was 2.5 g/cm<sup>3</sup> [62].

For both the pHAc–CaP and mHAc–CaP hydrogels, the CaP content was fixed at 30 wt% ( $\nu_{CPCS} = 0.12$ ). Thus, the  $G'$  values of both nanocomposite hydrogels were expressed in terms of frequency as follows:

$$G'_{comp}(\omega) = 0.12 \cdot G_{FCS}^P \exp \left[ \frac{\Delta E_{ad,total} - \delta F_{CPCS}}{k_B T} \right] + 0.88 \cdot G_{FCS}'(\omega).$$

All the parameters except for  $\Delta E_{ad,total}$  and  $\delta$  were assumed to be the same for both the pHAc–CaP and mHAc–CaP hydrogels. The dissociation between CaP and HAc chains for pHAc–CaP systems was assumed to be negligible (i.e.,  $\delta = 0$ ) because  $\Delta E_{ad,total}$  should be much larger than the dissociation energy ( $\delta F_{CPCS}$ ) because of the high electrostatic interaction between precipitated CaP and HAc chains. For the mHAc–CaP system, the values for  $\Delta E_{ad}$  and  $\delta$  reported by Sarvestani et al. were used [55] because the nanoparticles were directly used for the fabrication of composites without further treatment. Curve fitting revealed that the total absorption energy ( $\Delta E_{ad,total}$ ) of the pHAc–CaP hydrogel was approximately

10 times larger than that of the mHAc–CaP hydrogel, as indicated in **Table 3**. The higher total absorption energy between CaP nanoparticles and the HAc matrix in the pHAc–CaP hydrogels was induced by both the increased number of CaP particle–polymer binding sites ( $fN$ ) and higher absorption energy ( $\Delta E_{ad}$ ) compared with those of the mHAc–CaP hydrogels. The *in situ* precipitation facilitated 1) uniform particle distribution throughout the polymer matrix and 2) strong electrostatic interaction between CaP nanoparticles and polymer chains.

The numerical curve fitting followed the trends of the viscoelastic response observed in the experimental results, as shown in **Figure 2.1.14a**. In addition, significant enhancement of the mechanical stability of pHAc–CaP compared with that of the pure HAc and mHAc–CaP hydrogels was observed in the strain sweep results (**Figure 2.1.14b**). pHAc–CaP exhibited a noticeably larger linear viscoelastic region than mHAc–CaP, maintaining its structural integrity until a strain of 20%, whereas mHAc–CaP exhibited network breakdown from a strain of 7% with a decrease of  $G'$ . The enhanced elastic reinforcement and mechanical stability of pHAc–CaP indicates stronger binding between the HAc chains and CaP particles. The low  $G'$  and high nonlinearity of mHAc–CaP can be attributed to the weak polymer–particle interaction and strong aggregation of CaP particles. Based on these results, an overall schematic model of the composite hydrogels is presented in **Figure 2.1.14(left)**. A higher proportion of adsorbed HAc chains around CaP

particles was observed in the pHAc–CaP hydrogels, as shown in **Figure 2.1.14a**, which clearly differs from the lower density of attached chains in the mHAc–CaP hydrogels (**Figure 2.1.14b**). These pHAc–CaP hydrogel networks are believed to originate from the CaP nanoparticles acting as physical crosslinkers [63-66]. As discussed in the previous section, the chelating effect of ionized carboxyl groups of HAc and calcium ions during *in situ* CaP formation is believed to promote apatite nucleation through electrostatic interactions [67-69].

HAc played an important role in the formation of small and uniform CaP particles. One of the key parameters is the negatively charged carboxyl groups in HAc. During immersion of the HAc hydrogels in the solution of CaCl<sub>2</sub> and H<sub>3</sub>PO<sub>4</sub>, the carboxyl groups of HAc chains likely exist in a neutral form, with calcium and phosphate ions uniformly distributed in the HAc network. By increasing the pH of the solution to 11, the solubility of calcium and phosphate ions is rapidly lowered, and CaP precipitates start forming. Meanwhile, the calcium ions are thought to be chelated with the ionized carboxyl groups of HAc at higher pH. Therefore, the nucleation and precipitation of CaP is initiated from the surface of the HAc hydrogels [70, 71].

The surface morphologies of the specimens also support the suggested structural model concerning the molecular interaction mechanisms between HAc chains and CaP nanoparticles (**Figure 2.1.14(right)**). The surface morphology of pHAc–CaP

consisted of homogeneously dispersed CaP nanoparticles on the HAc surface (**Figure 2.1.14a**). During the *in situ* precipitation, these nanoparticles were uniformly formed on HAc with minimal agglomeration. However, the surface morphology of the mHAc–CaP was inhomogeneous because of the non-uniform distribution of agglomerated CaP particles (**Figure 2.1.14b**). The particles were observed to form clusters through particle agglomeration during physical mixing.

### **Enhancement of biological properties of pHAc–CaP hydrogels**

In most cases, phosphate-containing biomaterial scaffolds positively affect the promotion of cellular response [72,73]. In the present system, the nanosized adhesive sites of CaP nanoparticles in pHAc–CaP hydrogels may have provided physical attachment for the fibroblast cells [74]. In addition, the mechanical stability of the hydrogels is believed to positively affect fibroblast behavior [75-77]. Notably, no significant difference in cell proliferation levels was observed among the pHAc–CaP composite hydrogels with different CaP contents.

The poor biostability of HAc hydrogels is one of the major obstacles for suitable resistance to degradation, which is a prerequisite for all biomedical scaffold applications [52,55, 78, 79]. Pure HAc hydrogel is known to exhibit limited biostability because of its inherent structural instability and enzymatic reactions in the body. Our results clearly indicate that CaP nanoparticles not only improve the

dimensional stability of pHAc–CaP hydrogels over a certain period by hindering enzymatic degradation but also stimulate the cellular environments to generate collagen, which can enhance the structural support of the hydrogels and surrounding ECM [74, 80]. More specifically, stimulated by exposed CaP nanoparticles on the surface of pHAc–CaP hydrogels, fibroblast cells from surrounding tissues migrated to the area around pHAc–CaP hydrogels. This process resulted in the regeneration of a new tissue structure, including collagen deposition and vascularization [80,81]. Thus, HAc–CaP nanocomposites with long-term biostability and excellent bioactivity were generated using the *in situ* precipitation process, and these hydrogels show great potential for soft tissue engineering applications.

### **2.1.5. Conclusion**

By introducing *in situ* precipitation within a HAc hydrogel matrix, we developed HAc–CaP nanocomposite hydrogels with significantly enhanced mechanical strength and degradation resistance. These improvements were attributed to the resulting structural homogeneity, integrity, and minimal nanoparticle aggregation. In addition, pHAc–CaP hydrogels were successfully fabricated with uniformly precipitated CaP nanoparticles strongly conjugated with HAc polymer chains. With their structurally homogeneous architecture, enhanced physical crosslinks, and high density of entanglements resulting from the precipitated CaP nanoparticles, the

pHAc–CaP hydrogels exhibited significantly reduced *in vitro* and *in vivo* degradation rates and greatly improved mechanical moduli with highly elastic behavior. The biocompatibilities of the composite hydrogels was clearly enhanced compared with those of pure HAc and mHAc–CaP hydrogels. The pHAc–CaP hydrogels thus show great potential for use in various biomedical applications.

## Tables

**Table 1.** Theoretical and actual CaP content of pHAc–CaP hydrogels with the corresponding amounts of the two reactants, CaCl<sub>2</sub> and H<sub>3</sub>PO<sub>4</sub>

HAc–CaP hydrogel	Intended			Theoretical Ca/P ratio	Actual	Actual Ca/P ratio*
	CaP content (wt%)	CaCl <sub>2</sub> (M)	H <sub>3</sub> PO <sub>4</sub> (M)		CaP content (wt%)	
HAc–10 wt% CaP	10	0.041	0.024		11.98	
HAc–20 wt% CaP	20	0.072	0.043		21.10	
HAc–30 wt% CaP	30	0.153	0.092	1.67	33.26	1–1.5
HAc–40 wt% CaP	40	0.198	0.119		42.30	

\*The Ca/P ratios were calculated from both quantitative EDS analysis with amorphous nanoparticles and XRD phase analysis with heat-treated nanoparticles.

**Table 2.** Water content of fully hydrated nanocomposite hydrogels as a function of CaP content

CaP content (wt%)	Water content of pHA–CaP hydrogel (%)	Water content of mHA–CaP hydrogel (%)
0		99.06 ± 0.19
10	99.04 ± 0.19	98.96 ± 0.12
20	98.63 ± 0.17	98.47 ± 0.17
30	96.47 ± 0.78	98.35 ± 0.07
40	94.22 ± 0.52	98.28 ± 0.07

**Table 3.** Fitting values for net energy change of a chain segment after adsorption ( $\Delta E_{ad,total}/k_B T$ ) and activation length on the order of the displacement required to detach the absorbed segment from the particle surface ( $\delta$ )

Composite system	$\Delta E_{ad,total}/k_B T$	$\delta$
mHAc-30 wt% CaP	1.2	$0.5R_F$
pHAc-30 wt% CaP	12	0

## Figures

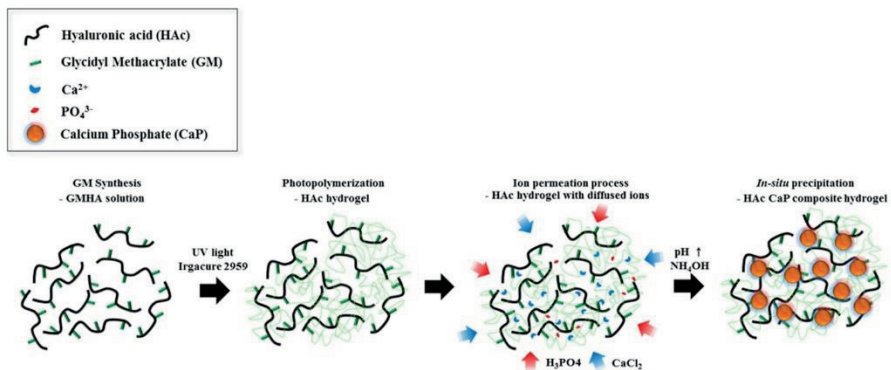
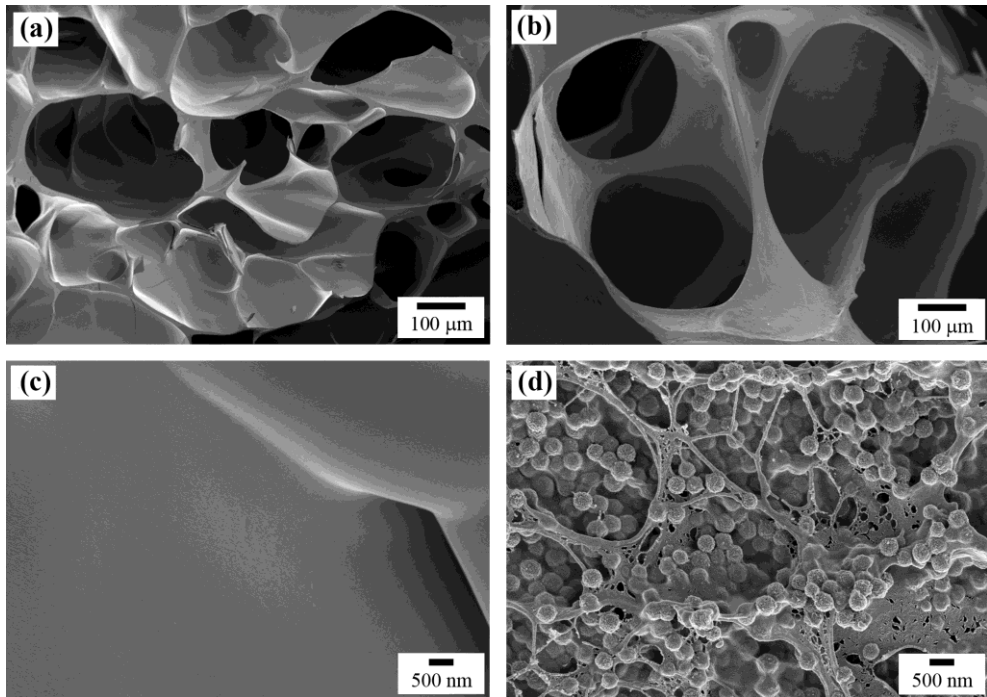
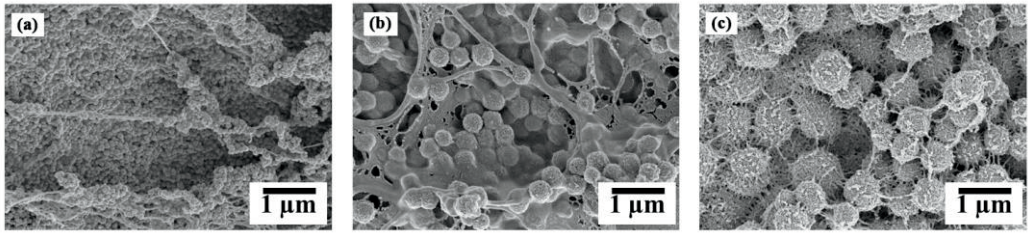


Figure 2.1.1. Schematic diagram of *in situ* precipitation of pHAc-CaP hydrogels.



**Figure 2.1.2. Cross-sectional morphologies of (a) pure HAc and (b) pHAc-30 wt% CaP hydrogels and surface morphologies of (c) pure HAc and (d) pHAc-30 wt% CaP hydrogels at high magnification ( $\times 30k$ ).**



**Figure 2.1.3. Surface morphologies of (a) pHAc–10 wt% CaP, (b) pHAc–30 wt% CaP, and (c) pHAc–50 wt% CaP hydrogels at high magnification ( $\times 30k$ ).**

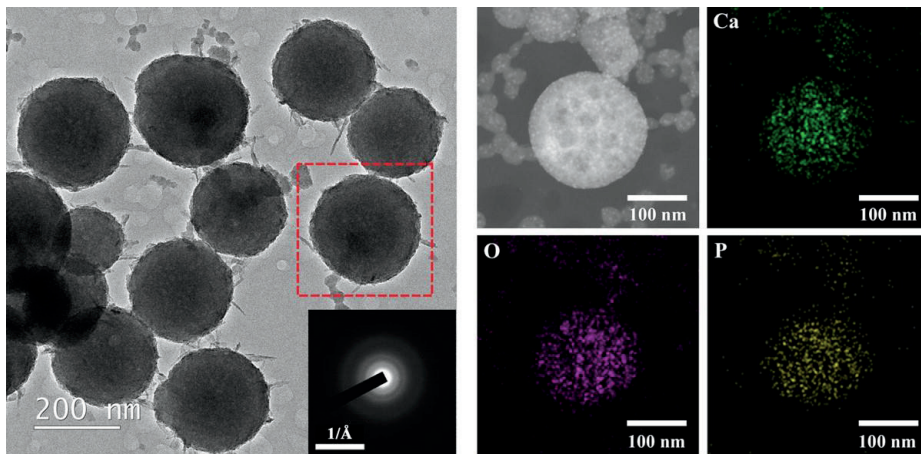


**Figure 2.1.4. Representative TEM image of CaP nanoparticles in pHAc–CaP hydrogels with EDS mapping analysis (inset: SAED patterns of CaP nanoparticles).**

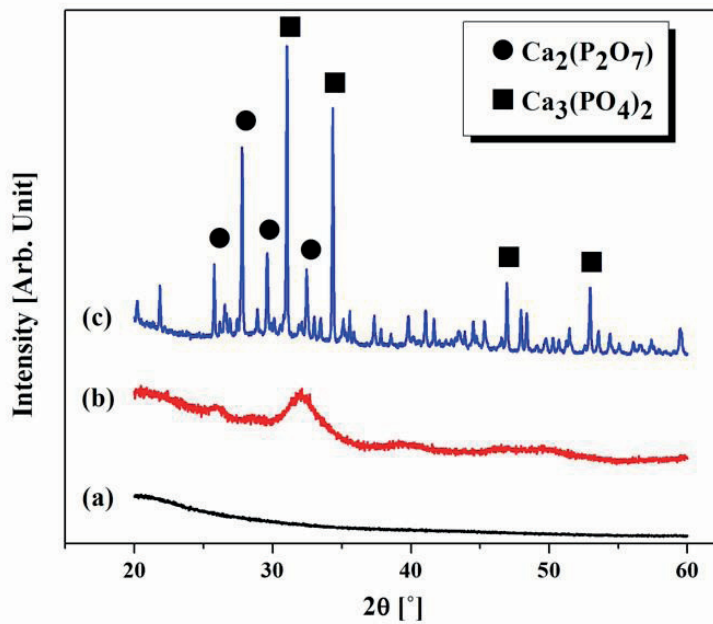
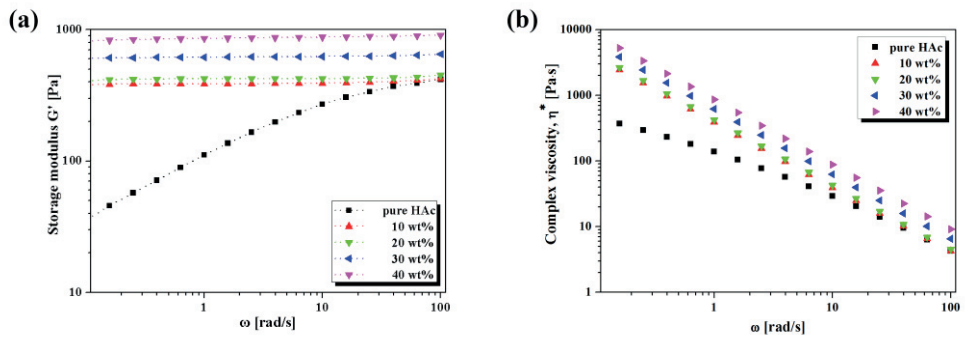
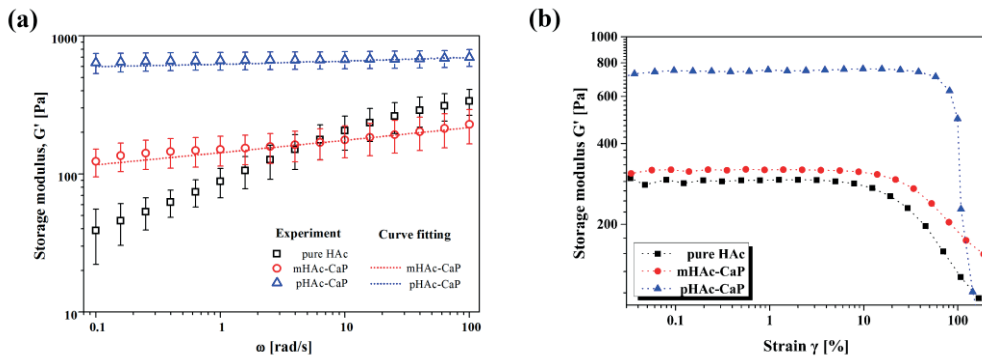


Figure 2.1.5. XRD patterns of (a) as-prepared pure HAc hydrogel, (b) as-prepared pHAc–CaP hydrogel, and (c) pHAc–CaP hydrogel after heat treatment at 1100 °C.



**Figure 2.1.6. Rheological behavior of pHAc–CaP hydrogels: (a)  $G'$  as a function of frequency for various CaP contents and (b) complex viscosity as a function of frequency.**



**Figure 2.1.7. (a)  $G'$  of pure HAc, pHAc-30 wt% CaP, and mHAc-30 wt% CaP hydrogels as a function of frequency. (b)  $G'$  of pure HAc, pHAc-30 wt% CaP, and mHAc-30 wt% CaP hydrogels as a function of strain.**

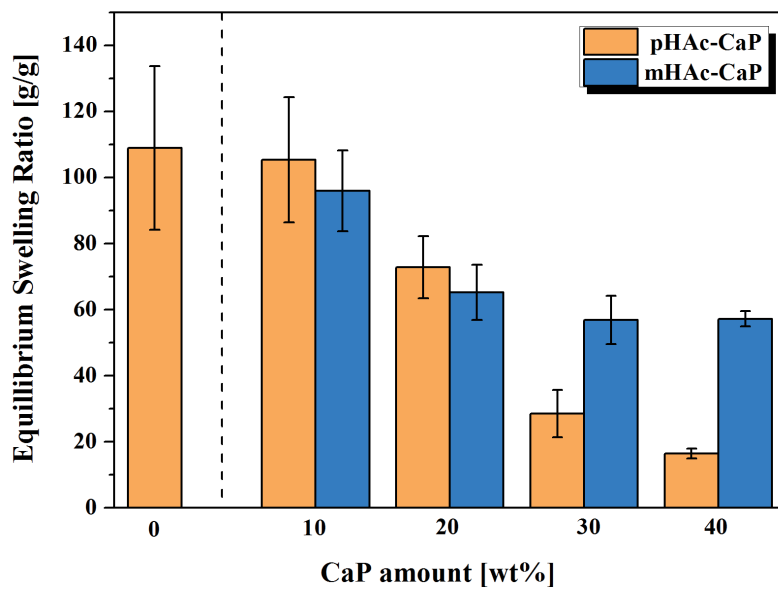
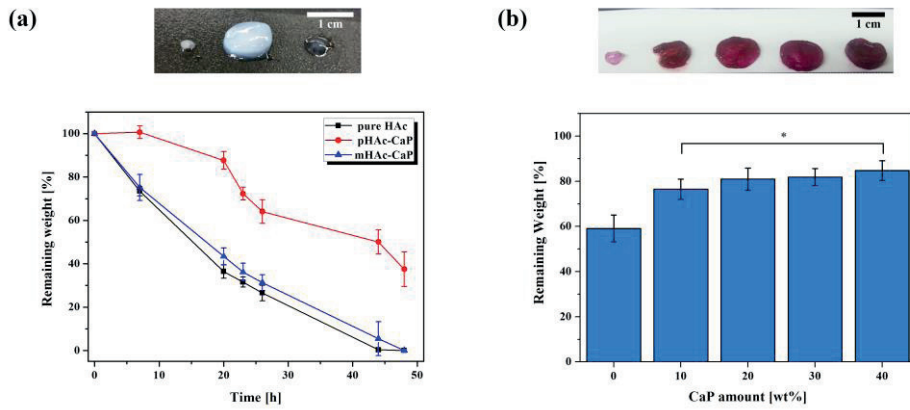
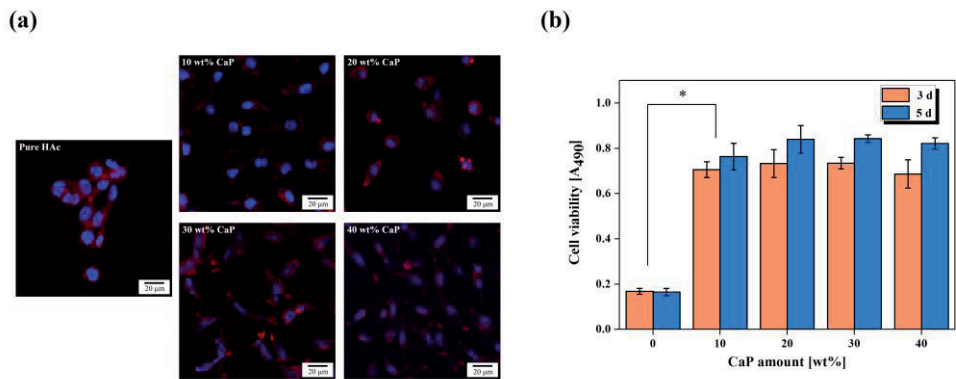


Figure 2.1.8. Swelling ratios of the hydrogels after immersion for 24 h in PBS at 37 °C.



**Figure 2.1.9. *In vitro* enzymatic degradation behavior of pure HAC, mHAc–CaP, and pHAc–CaP hydrogels: (a) comparison of degradation rates as a function of incubated time and (b) remaining weight after 4 h of degradation with CaP content.**



**Figure 2.1.10. *In vitro* cellular response of pure HAC and pHAc–CaP hydrogels:**  
**(a) representative CLSM images of L929 fibroblasts cultured on pure HAC and**  
**pHAc–CaP hydrogels for 3 days and (b) cell viability of pure HAC and pHAc–**  
**CaP hydrogels measured by MTS assay after 3 and 5 days.**

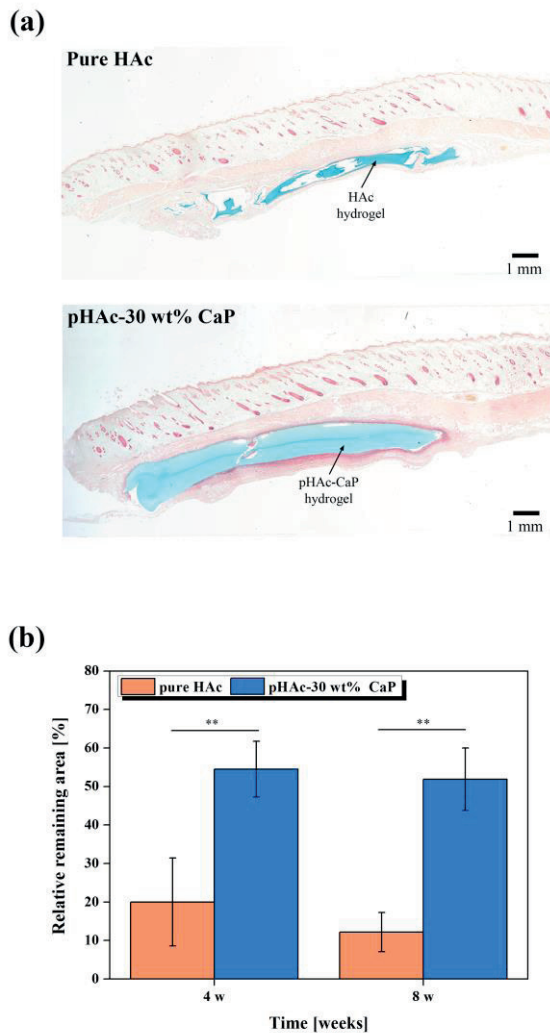


**Figure 2.1.11. *In vivo* enzymatic degradation behavior of pure HAc and pHAc–CaP hydrogels: (a) histological images of pure HAc (top) and mHAc–30 wt% CaP hydrogel (bottom) stained by Alcian blue 4 weeks after implantation and (b) remaining area ratio of pure HAc and pHAc–30 wt% CaP hydrogels 4 and 8 weeks after implantation.**

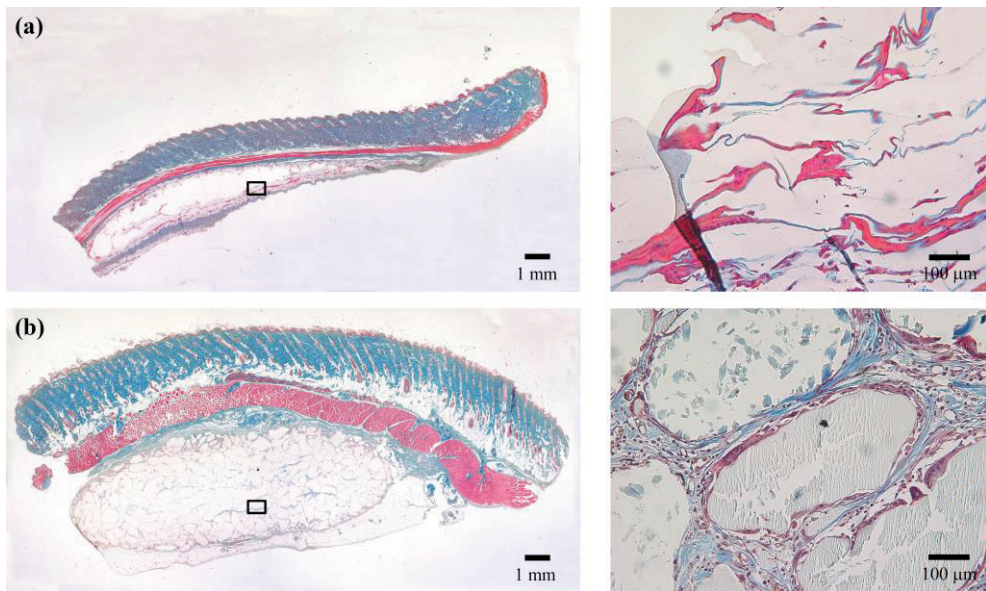


**Figure 2.1.12. *In vivo* bioactivity test of hydrogel injection on subcutaneous tissue of SD rat: histological images (left) of (a) pure HAc and (b) pHAc-30 wt% CaP hydrogel stained by MT 4 weeks after implantation and high-magnification images (right) of the histological images.**

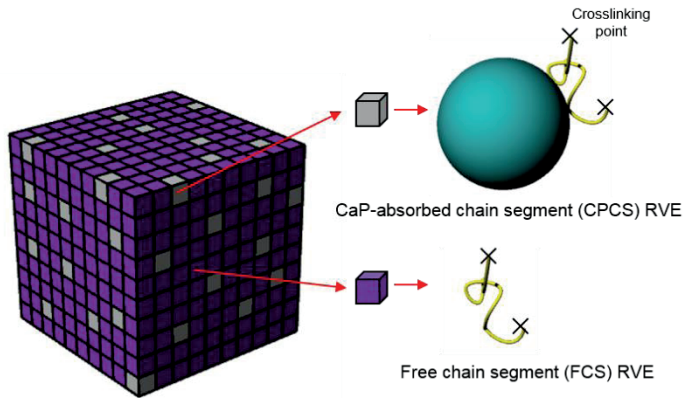


**Figure 2.1.13. Schematic diagram of the composite hydrogel models with CaP nanoparticles showing two representative volume element models with and without CaP nanoparticles in the unit.**

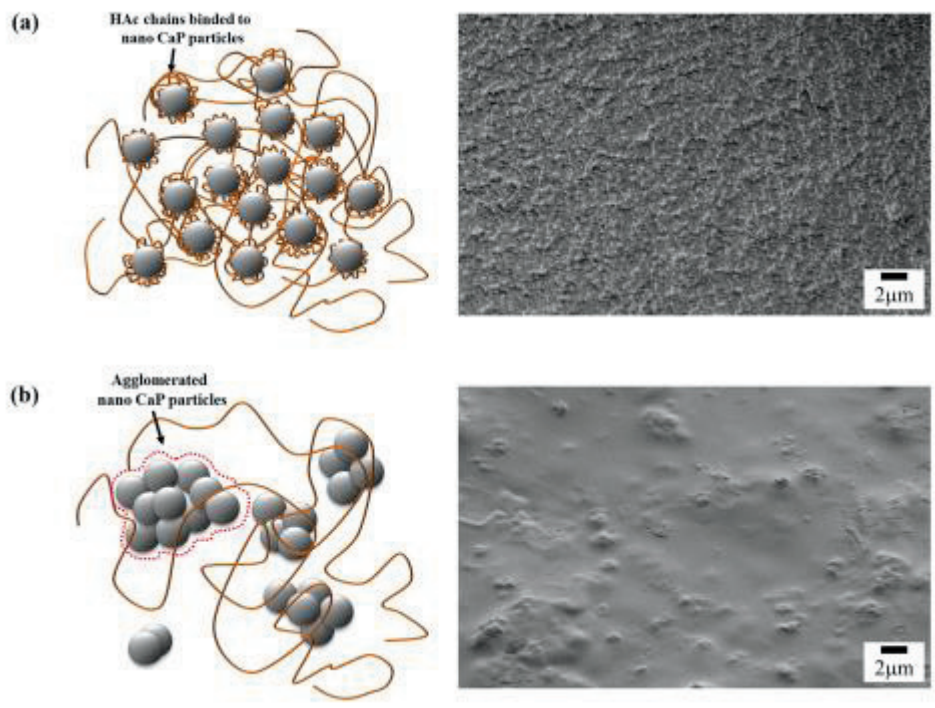


**Figure 2.1.14. Schematic illustration (left) and surface morphology (right) of (a) pHAc–30 wt% CaP and (b) mHAc–30 wt% CaP hydrogels.**

## **2.2. Mechanically Enhanced HAc-Based Nanocomposite Hydrogels via Dual-Crosslinking Process**

### **2.2.1. Introduction**

Hydrogels with enhanced mechanical properties have been comprehensively investigated using various approaches, such as introducing double networks [82-85] and ionic-covalent entanglement networks [86-88]. These hybrid systems have been demonstrated to generate toughness via covalent crosslinking and to dissipate mechanical energy under deformation via ionic crosslinking [89]. Ionic crosslinking not only easily generates an interpenetrating network but also provides multifunctionality, such as *in situ* gelling formation for an injectable scaffold or a controlled delivery system [90-92]. Chelation of metallic ions between negatively charged groups of polymers generally results in the formation of coordinate bonds during ionic crosslinking [93,94]. Thus, hydrogels crosslinked by different cations have been extensively developed [95-97]. However, the effects of ionic crosslinking on the mechanics of nanocomposite hydrogel systems have been explored much less frequently.

We investigated the contribution of ionic crosslinking using various cations in HAC–CaP nanocomposite hydrogels, which were fabricated using the *in situ* precipitation process. We proposed an ionic crosslinking method using various cations in conjunction with chemical crosslinking after *in situ* CaP precipitation of HAC to enhance the mechanical stability. The multi-functionality of dual-crosslinked HAC–CaP hydrogels was expected, which would not only improve the mechanical and structural stabilities but also accelerate cellular responses during dissolution under physiological conditions.

## **2.2.2. Experimental procedures**

### **Fabrication of dual-crosslinked nanocomposite hydrogels**

All the HAC hydrogels in this work were photo-crosslinked via glycidyl methacrylation synthesis. CaP was precipitated through *in situ* precipitation in the crosslinked HAC hydrogel, as described in **Chapter 2.1** [98]. Dual-crosslinking systems were introduced to both pure HAC and HAC–CaP hydrogels using various cations. NaCl, CaCl<sub>2</sub>, BaCl<sub>2</sub>, SrCl<sub>2</sub>, FeCl<sub>3</sub>, and AlCl<sub>3</sub> were purchased from Sigma–Aldrich. The ionic crosslinking process was initiated in both the crosslinked HAC and HAC–CaP hydrogels by immersing them in aqueous solutions (1 M concentrations) containing multivalent cations (Ca<sup>2+</sup>, Al<sup>3+</sup>, Ba<sup>2+</sup>, Sr<sup>2+</sup>, and Fe<sup>3+</sup>) for 6 h.

### **TEM Characterization of HAC–CaP hydrogels**

The inorganic phases of the HAC–CaP hydrogels after dual crosslinking with divalent cations ( $\text{Ca}^{2+}$ ,  $\text{Ba}^{2+}$ , and  $\text{Sr}^{2+}$ ) were evaluated using TEM (Tecnai F20, FEI, USA). During the fabrication process, 400-mesh copper grids were placed in the hydrogels, which were then dried in air for 2 days. The solutions containing divalent cations were diluted to  $10^{-3}$  M. EDS mapping was also performed to examine the compositional changes of the nanoparticles.

### **Mechanical behaviors of composite hydrogels**

The mechanical behavior of the hydrogels was assessed using a rheometer (ARES, Rheometric Scientific, USA). Frequency sweeps were performed in the angular frequency range of 0.1 to 100 rad/s at a strain of 1% in the linear region to measure  $G'$  and  $G''$ . Disc-shaped hydrogels with diameters of 12 mm and lengths of 7 mm were prepared for the compression tests. For dual-crosslinking, the HAC and HAC–CaP hydrogels were immersed in 0.5 M solutions using different cations for 10 h. Uniaxial compression tests were performed on the hydrogels at a rate of 2 mm/min using an Instron machine with a 1-kN load cell.

### ***In vitro* cell tests**

Pre-osteoblast cells (MC3T3-E1) at densities of  $1 \times 10^4$  cells/mL were seeded on

the hydrogels for the cell attachment. The cells were cultured in  $\alpha$ -MEM (Welgene, Korea) supplemented with 5% FBS and 1% penicillin–streptomycin in a humidified incubator with 5% CO<sub>2</sub> at 37 °C for 3 days. After being fixed using 4% paraformaldehyde, the cells on the samples were stained with anti-vinculin, fluorescent phalloidin, and DAPI for 1 h, 20 min, and 5 min, respectively. The cells attached on the hydrogels were examined using CLSM (FluoView FV1000, Olympus, Japan). For the cell proliferation test,  $3 \times 10^4$  cells/mL of cells were seeded on the hydrogels. After culturing for 3 and 5 days, the levels of cell proliferation were measured using the MTS assay (CellTiter 96 Aqueous One Solution, Promega, USA). Cell differentiation tests were performed in two ways. First,  $1 \times 10^4$  cells/mL of cells were seeded on the surface of the hydrogels to verify the bioactivity of the samples. In addition, ion-release medium was used to investigate the ion effect on cell differentiation. All the media were refreshed into new media including 10 mM b-GP and 50  $\mu$ g/mL ascorbic acid every 2 days. The alkaline phosphatase (ALP) test was conducted on day 7 to measure the amount of p-nitrophenyl phosphate (pNPP, Sigma–Aldrich, UK), which is an early indicator of the osteoblastic phenotype maintenance. The conversion of pNPP to p-nitrophenol (pNP) in the presence of ALP results in a color change. A microplate reader was used to determine the absorbance at 405 nm.

### Statistical analysis

All the experimental results were expressed as the mean  $\pm$  SD. The difference between the two groups was determined using a one-way ANOVA, and  $p < 0.01$  and  $p < 0.005$  were considered to be statistically significant.

## 2.2.3. Results

### Characterization of hydrogels

First, HAC–CaP hydrogels were fabricated via *in situ* precipitation of photo-crosslinked HAC hydrogels (single crosslinked, called **single CL**). Ionic crosslinking systems using various cations have been developed to fabricate HAC–CaP nanocomposite hydrogels with additional crosslinking (dual crosslinked, called **dual CL**) to achieve higher mechanical stabilities. The single- and dual-CL systems are schematically illustrated in **Figure 2.2.1**.

All the hydrogels had porous microstructures, as observed in **Figure 2.2.2**, indicating that the hydrogel network was maintained after the *in situ* precipitation process and ionic treatment for the dual-CL system. The single-CL HAC and HAC–CaP hydrogels exhibited highly porous structures with pore sizes of 300–500  $\mu\text{m}$  and interconnected pores. After dual crosslinking, the pore size decreased; however, the sample morphologies differed depending on the cations used. The  $\text{Na}^+$ -treated HAC hydrogels exhibited similar morphology as the single-CL HAC hydrogel. The

pore sizes of the  $\text{Ca}^{2+}$ -,  $\text{Ba}^{2+}$ -, and  $\text{Sr}^{2+}$ -treated HAC and HAC–CaP hydrogels decreased to approximately 200–300  $\mu\text{m}$ , indicating the increase of the crosslinking densities of those hydrogels. The  $\text{Fe}^{3+}$ - and  $\text{Al}^{3+}$ -treated HAC–CaP hydrogels also showed a decrease in pore size compared with the pure HAC hydrogels.

### **Mechanical properties of hydrogels**

The mechanical behavior of the pure HAC and HAC–CaP hydrogels crosslinked by both chemical and ionic crosslinking ( $\text{Ca}^{2+}$ ) was significantly improved compared with that of the photo-crosslinked hydrogels without ionic crosslinking, as observed in **Figure 2.2.3a**. In particular, ionic crosslinking increased  $G'$  of both the pure and composite HAC hydrogels by factors of  $\sim 1.5$  (pure HAC) and  $\sim 2.5$  (HAC–CaP). To explore the efficiency of ionic crosslinking using different cations, the  $G'$  values at 1 rad/s were compared, as depicted in **Figure 2.2.3b**. Interestingly, dual crosslinking had a more positive effect on the HAC–CaP hydrogels than on the pure HAC hydrogels. Even though all six cations appeared to work as effective ion crosslinkers, the mechanical improvements differed for the HAC–CaP hydrogels depending on the ions used (but not for the pure HAC hydrogels). In particular, treatment with  $\text{Ca}^{2+}$  ions resulted in the highest mechanical improvement of the HAC–CaP hydrogels, whereas  $\text{Al}^{3+}$  and  $\text{Fe}^{3+}$  were less effective, as they resulted in decomposition of the CaP particles because of their acidic environments.

During the compression tests, all the hydrogels collapsed at strains of approximately 0.77–0.8. The fracture stress was determined from the fracture point, and the fracture energy was determined by measuring the area of the stress–strain curve. From the cyclic test to 50% compression, the dissipation energy was measured by calculating the areas of the loading and unloading curves. As observed in the representative stress–strain curve of the hydrogels (**Figure 2.2.4a**), the dual-CL system is clearly more effective in enhancing the mechanical properties for the HAc–CaP hydrogels than the HAc hydrogel. In addition, the HAc hydrogels crosslinked by either single or dual crosslinking showed highly elastomeric behavior, as observed in the cyclic test graph (**Figure 2.2.4b**). The incorporation of CaP into the hydrogels reduced the recovery of the compressive properties. The dual-CL HAc–CaP hydrogels exhibited an even further reduction in recovery than the single-CL HAc–CaP hydrogels, showing an increase of dissipated energy after unloading compared with the other samples. These findings clearly demonstrate that the presence of CaP nanoparticles and additional ionic treatment induced viscoelasticity behavior of the hydrogel, restricting the HAc chain movement. The stress at 0.5 strain, dissipation energy, fracture strain, fracture stress, and fracture energy data are summarized in **Table 4**.

### **Swelling properties of hydrogels**

The swelling properties of the hydrogels showed similar tendencies as the mechanical properties (**Figure 2.2.5**). **Figure 2.2.5a** shows the swelling properties of the composite hydrogels, which were single or dual crosslinked in distilled water. The use of *in situ* precipitation to incorporate nanosized CaP particles in HAc–CaP hydrogels resulted in a reduction of the swelling ratio from 150% to 50%. The Ca<sup>2+</sup>-, Ba<sup>2+</sup>-, and Sr<sup>2+</sup>-treated composite hydrogels shrunk significantly compared with the Fe<sup>3+</sup>-treated one because their acidic environments caused the decomposition of CaP particles of the composite hydrogel (**Figure 2.2.5b**).

### ***In vitro* cellular responses of hydrogels**

The ion effect on the cellular response was analyzed using cell attachment, proliferation, and differentiation tests with MC3T3 cells (**Figure 2.2.6**). Ionic treatment led to a significant enhancement of the cell viability when dual crosslinking was applied to the HAc–CaP hydrogel. In particular, Ca<sup>2+</sup> and Ba<sup>2+</sup> ions strongly affected the MC3T3 cells, causing substantial stretching (**Figure 2.2.6a**) and proliferation (**Figure 2.2.6b**). The MC3T3 cells on the dual-CL HAc–CaP hydrogels appeared more stretched than those on the single-CL HAc hydrogels. The cell spreading areas of the dual-CL hydrogels, especially for those treated with Ca<sup>2+</sup> and Ba<sup>2+</sup>, were significantly larger (350–410  $\mu\text{m}^2$ ) than those of the single-CL hydrogels (~205  $\mu\text{m}^2$ ).

To investigate the ion effect on cell differentiation, an ALP activity test was performed in two ways, by producing cell-laden hydrogels and using ion-release medium; the results for the dual-CL HAC–CaP hydrogels are presented in **Figure 2.2.6c**. The  $\text{Ca}^{2+}$ - and  $\text{Ba}^{2+}$ -treated HAC–CaP hydrogels exhibited higher levels of ALP than the single-CL HAC–CaP and  $\text{Sr}^{2+}$ -treated hydrogels (**Figure 2.2.6d**). However, all the ions greatly affected osteogenic differentiation, as observed in **Figure 2.2.6e**, which agrees well with the findings of a previous study on the  $\text{Sr}^{2+}$  ion effect on preosteoblast cell viability [99].

#### **2.2.4. Discussion**

We focused on dual crosslinking using divalent ions to enhance the mechanical properties of HAC–CaP hydrogels. Increased efficiency of ionic crosslinking was observed with pre-treatment of HAC at pH 11 compared with that at pH 7 (**Figure 2.2.7**). Because the *in situ* precipitation was performed at pH 11 for the composite hydrogels, no additional pH treatment was required.

The pH effect during the dual-CL process could provide a reasonable explanation for the resulting mechanical enhancement. Because the HAC–CaP hydrogels were fabricated using the *in situ* precipitation process, the pH was approximately 11. Thus, pre-treatment of HAC at pH 11 was conducted to verify the efficiency of ionic crosslinking compared with that at pH 7.  $G'$  of the HAC–CaP hydrogels at higher pH

showed a significant increase. This finding is associated with the charge density of HAc, which contains negatively charged carboxyl groups [93, 100]. The charge density highly depends on the pKa value [101] and is thus affected by the pH of the solution during dual crosslinking. Because the pKa of HAc carboxyl groups is known to be 3–4, the global charge density increased with the pH 11 treatment compared with the pH 7 treatment, corresponding with the higher efficiency of mechanical enhancement at higher pH, as observed in **Figure 2.2.7**. Thus, it can be inferred that the *in situ* precipitation environment facilitated a high affinity of ions for chelation with the ionized carboxyl groups of HAc, resulting in higher crosslinking densities.

The CaP nanoparticles after dual crosslinking using  $\text{Ca}^{2+}$ ,  $\text{Ba}^{2+}$ , and  $\text{Sr}^{2+}$  ions were also examined to verify the structural and compositional changes resulting from the additional ion incorporation (**Figure 2.2.8**). According to the TGA results presented in **Figure 2.2.8a**, the amount of particles increased after treatment with divalent ions. Although smaller CaP particles were additionally formed after treatment with  $\text{Ca}^{2+}$  ions, no compositional change was observed after the dual-CL process using either  $\text{Ba}^{2+}$  or  $\text{Sr}^{2+}$  ions (**Figure 2.2.8b**). It can be inferred that the Ca ions resulted in a synergistic effect, inducing additional precipitation and subsequently facilitating the ionic crosslinking with HAc chains.

The great enhancement of the mechanical stability resulted in improvement of the cell biocompatibility of the hydrogels because the stiffer matrix served as a more

desirable environment for fostering cellular behaviors, especially for osteogenic differentiation [102-104]. In addition, the CaP nanoparticles with biocompatible ions positively affected the stimulation of pre-osteoblast cells. In particular, the  $\text{Ca}^{2+}$  and  $\text{Sr}^{2+}$  ions seemed to greatly contribute to enhanced cell attachment and viability [105-107]. Moreover, the  $\text{Ba}^{2+}$ -treated HAc–CaP hydrogels supported better cell attachment, showing a high degree of cell polarization and proliferation, which can be explained by its good hydrophilicity [108, 109]. Because the dual-CL HAc–CaP hydrogels continuously released ions under physiological conditions, especially in the early stage, the cells surrounding the hydrogels were greatly stimulated by biocompatible ions.

Finally, the structural stabilities of the nanocomposite hydrogels in PBS solution were also investigated (**Figure 2.2.9**). Because of the exchange of divalent ions to  $\text{Na}^+$  ions in PBS solution, the dual-CL nanocomposite hydrogels exhibited a dramatic increase in weight (approximately 30% increase) with large water uptake. After 1 day in PBS, the dual-CL hydrogels maintained their structure. Interestingly, the  $\text{Ca}^{2+}$ - and  $\text{Ba}^{2+}$ -treated hydrogels exhibited higher stability than the  $\text{Sr}^{2+}$ -treated one and thus had longer-lasting properties.

### **2.2.5. Conclusion**

In this work, we demonstrated that introducing the additional step of ionic

crosslinking in preparing the HAc–CaP hydrogels resulted in great improvement of the physical properties. In particular, treatment with  $\text{Ca}^{2+}$ ,  $\text{Ba}^{2+}$ , and  $\text{Sr}^{2+}$  ions was more efficient than treatment with trivalent ions, which resulted in the decomposition of CaP particles in the acidic environment. In addition, the dual-CL HAc–CaP hydrogels exhibited promising biological properties, thereby extending their potential application to hard tissue engineering.

## Table

**Table 4. Mechanical properties of hydrogels crosslinked by either single- or dual-crosslinking with Ca<sup>2+</sup>**

		Stress at 0.5 strain	Dissipation energy until 0.5 strain (kJ/m <sup>3</sup> )	Fracture strain	Fracture stress (kPa)	Fracture energy (kJ/m <sup>3</sup> )
HAc	Single-CL	2.49±0.60	0.075±0.01	0.78±0.01	116.61±16.88	6.00±0.12
	Dual- CL(Ca)	2.65±0.83	0.068±0.01	0.81±0.03	160.25±54.41	8.71±1.15
HAc- CaP	Single-CL	2.75±0.43	0.113±0.02	0.78±0.01	342.57±40.44	12.95±2.06
	Dual- CL(Ca)	4.82±1.30	0.164±0.06	0.75±0.04	453.11±151.5	18.50±4.32

# Figures

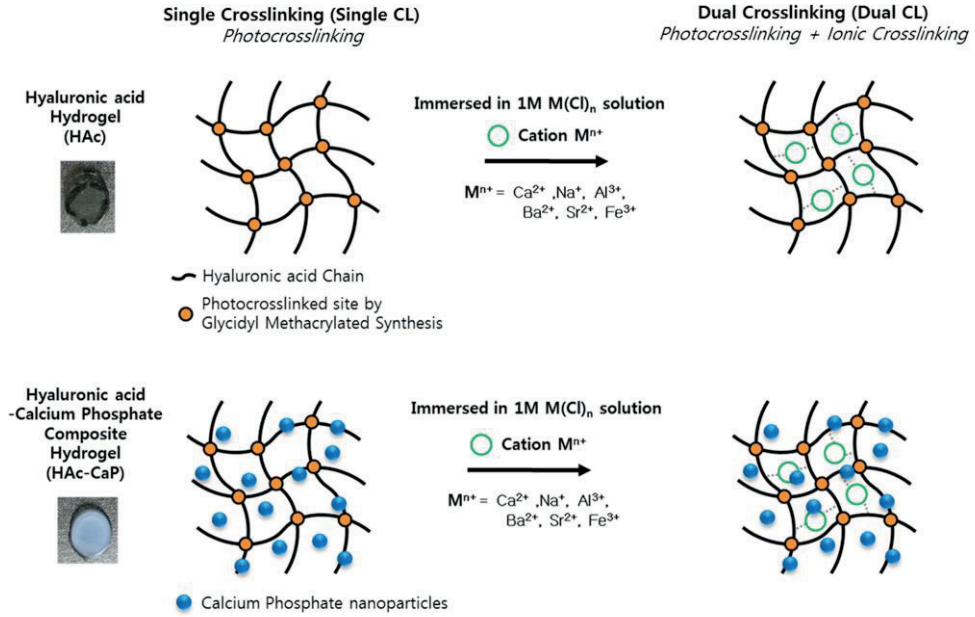


**Figure 2.2.1. Fabrication of hydrogels using single crosslinking and dual crosslinking.**

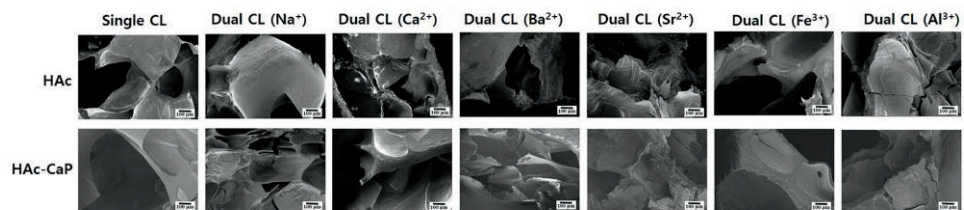


**Figure 2.2.2. Cross-sectional images of single-CL and dual-CL hydrogels.**

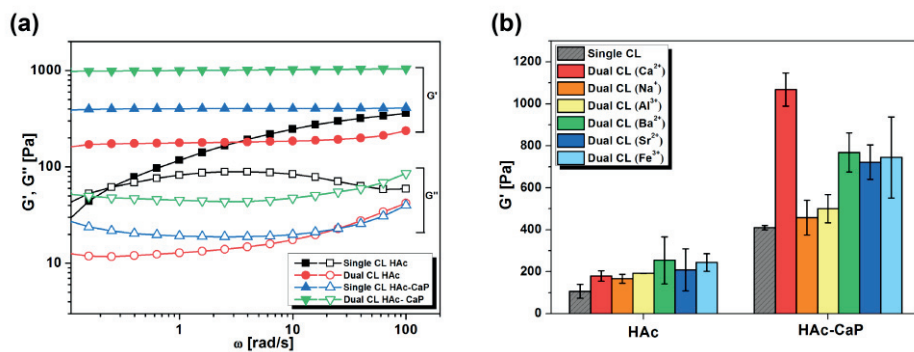
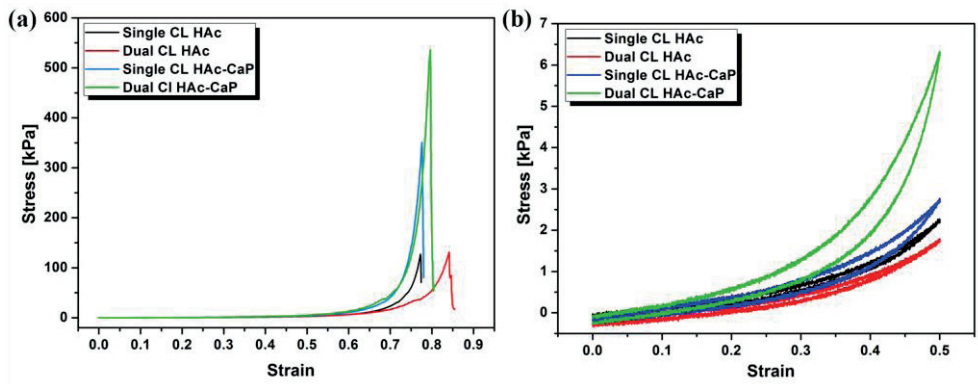


Figure 2.2.3. (a) Rheological behaviors ( $G'$ ,  $G''$ ) of HAc and HAc-CaP hydrogels crosslinked by single- or dual-crosslinking using  $\text{Ca}^{2+}$  ions in frequency sweep and (b)  $G'$  at 1 Hz of single- or dual-CL hydrogels.



**Figure 2.2.4. Compression properties of single- and dual-CL hydrogels: (a) stress–strain curves of HAC and HAC–CaP hydrogels crosslinked by single- or dual-crosslinking using  $\text{Ca}^{2+}$  ions until gel fracture and (b) cyclic test until 50% compression.**

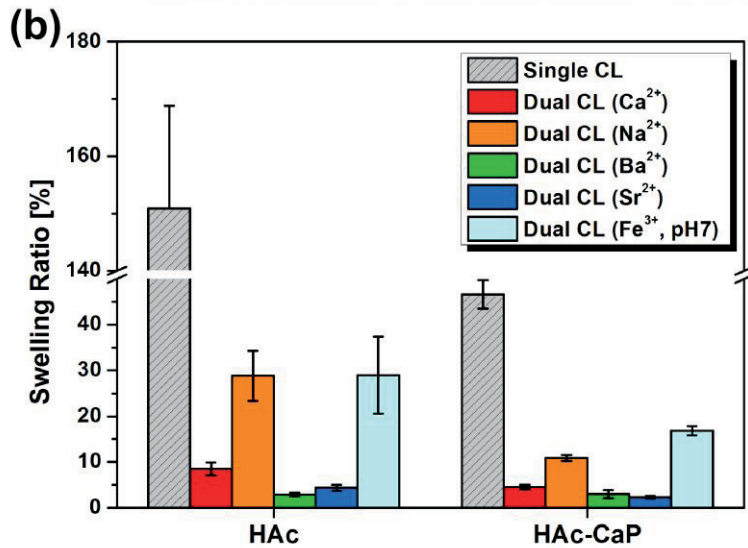
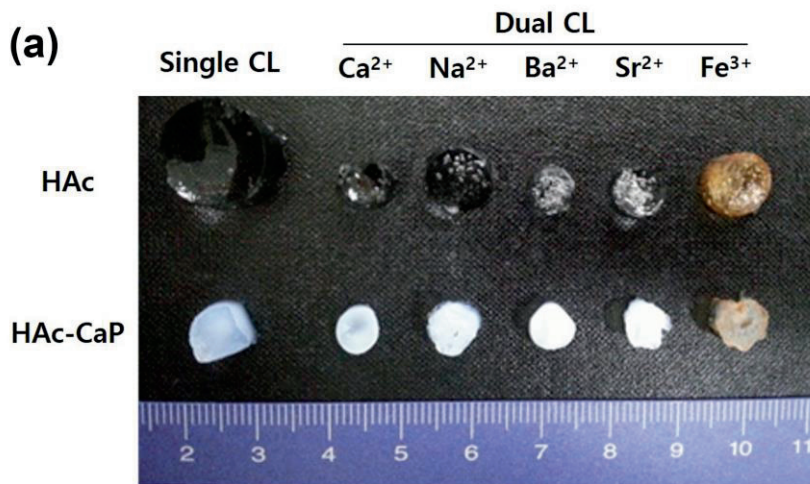
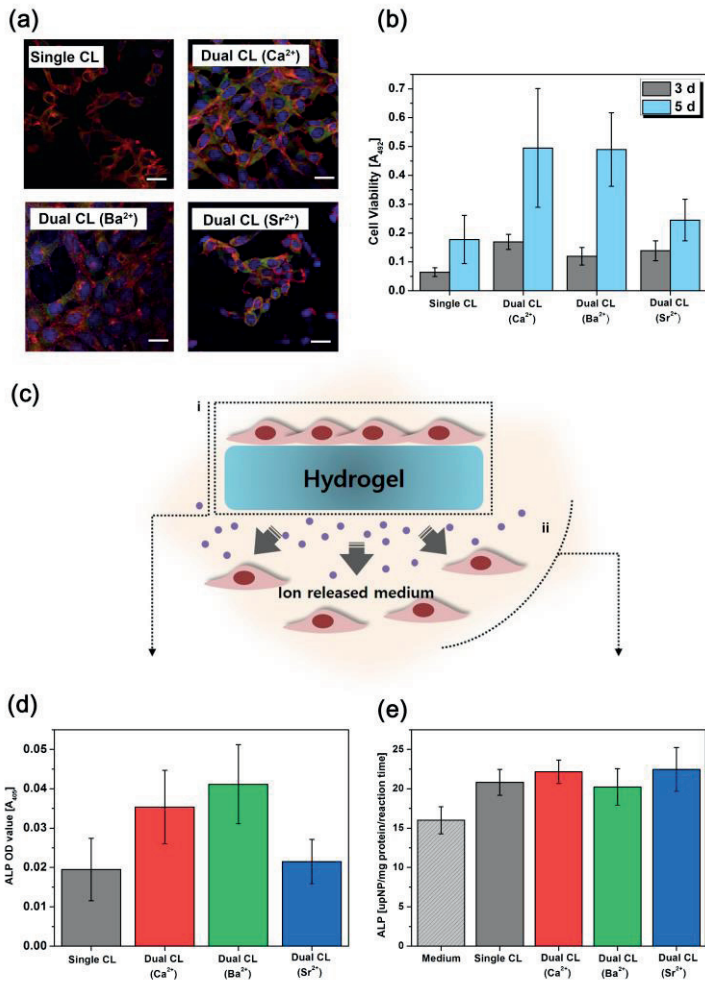


Figure 2.2.5. (a) Optical images and (b) swelling ratio of single- and dual-CL hydrogels.



**Figure 2.2.6. (a) Osteoblast cell attachment and (b) MTS proliferation assay after 3 and 5 days of culturing on HAC–CaP hydrogels. (c) Schematic diagrams of cell differentiation tests: (i) seeded on the surface of hydrogels and (ii) cultured in ion-release medium. ALP activity of osteoblasts cells (d) on the surface of HAC–CaP hydrogels and (e) in the ion-release medium after 7 days of culturing.**

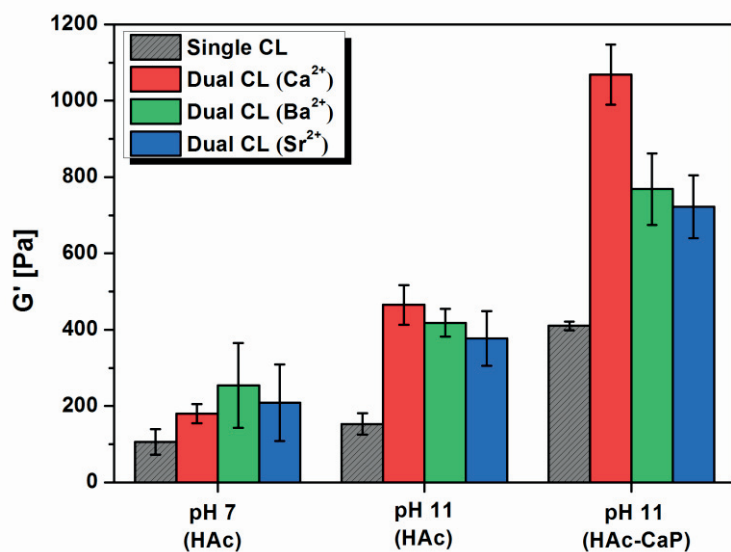


Figure 2.2.7. Pre-treatment effects at different pH:  $G'$  at 1 Hz of dual-CL HAc–CaP hydrogels compared with that of single-CL HAc–CaP hydrogel.

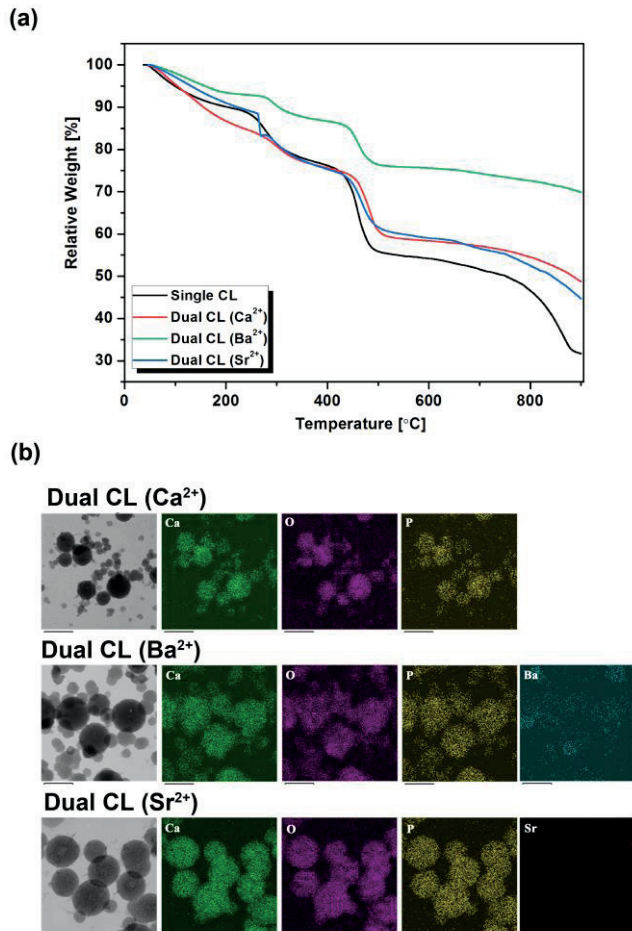


Figure 2.2.8. (a) TGA curves of single- and dual-CL HAC–CaP hydrogels. (b) TEM and EDS mapping images of inorganic CaP nanoparticles in HAC–CaP hydrogels after dual-crosslinking using ionic solutions containing (a)  $\text{Ca}^{2+}$ , (b)  $\text{Ba}^{2+}$ , and (c)  $\text{Sr}^{2+}$  (scale bar = 250 nm).

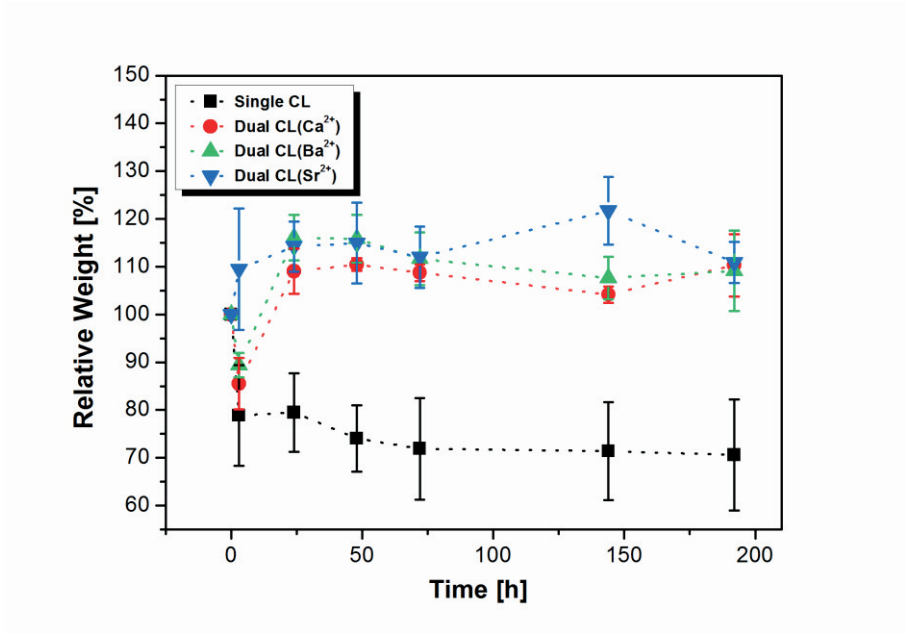


Figure 2.2.9. Swelling ratio profile of single- and dual-CL HAC-CaP hydrogels.

## **Chapter 3.**

# **Hyaluronic Acid–Hydroxyapatite Nanocomposite Hydrogels for Injectable Dermal Fillers**

### 3.1. Introduction

Skin aging is a physiological phenomenon that involves a gradual change in biomechanical performance and several associated defects, such as contour deficiencies and wrinkles [110] and loss of the dermal matrix. The resulting decreases in the amounts of collagen and elastic fibers eventually cause decreased elasticity [111, 112]. Thus, the design of a soft tissue augmentation product, such as an injectable filler, has been highlighted for wrinkle correction and skin elasticity recovery [113-115]. An injectable dermal filler has been developed in hydrogel form with high water uptake capacity to lift the tissue matrix. Ideal filler requires additional properties such as biocompatibility, high viscoelasticity, and longevity for better lifting capacity and stable maintenance of the strengthened state of the skin [116, 117]. To fulfill these requirements, the medical use of dermal fillers has evolved from the introduction of bovine collagen to synthesized materials such as poly l-lactic acid or polymethyl methacrylate and finally to a mixture of polymers and ceramic particle mixtures [118]. However, these materials have limitations. Collagen often generates an immune response [119]; synthetic polymers lack reversibility [120], which leads to the need for multiple treatments; and the ceramic particles in polymer and ceramic particle mixtures can be contraindications for their use, thus limiting their applicability to specific sites [121].

The most prevalent material for injectable dermal fillers is HAc because it is

biocompatible, non-immunogenic, and biodegradable [122, 123]. In addition, the high water absorption capability of HAc helps to further augment skin tissue [124, 125] and results in excellent biological performance by stimulating fibroblast cells to produce collagen [80, 111, 112, 126]. However, because of the fast degradation of HAc via enzymatic hydrolysis, the bioactive effects of HAc filler significantly decrease over time, which has a negative effect on cell proliferation to produce a new matrix under skin defects, resulting in poor structural integrity between the tissue matrix [127, 128]. Thus, there have been many efforts to increase the stability of HAc by chemical crosslinking to provide robust gel networks [129, 130] or by incorporating other materials to fabricate composite systems [131].

The biomechanical properties and biological stability of HAc composite systems can be significantly improved by incorporating synthetic materials, such as PEG [116], polyvinyl alcohol [132], and natural polymers such as collagen [133-136] and carboxymethyl cellulose, which is a biosynthesized form of cellulose [137]. However, these polymer–polymer composite systems tend to be limited in terms of improving the mechanical robustness or bioactivity in filler applications. Another approach involves using nanoparticles to reinforce polymer hydrogels as the strong interactions between polymer chains and nanoparticles play critical roles in enhancing the strength of the hydrogels [138]. In addition, the use of polymeric scaffolds and nanoparticles has resulted in promising improvements, extending their

application for soft tissue repairs. As a more extensible approach of fabricating nanocomposite hydrogels, our group developed an *in situ* precipitation process to fabricate HAc–HAp nanocomposite hydrogels (HAc– nanoHAp) that possess high mechanical strength and enzymatic resistance [98, 139]. In this system, *in situ* precipitation expedited the strong reaction between HAc and Hap, regulating uniform mineralization of HAp nanoparticles in HAc chains. These homogeneous structures greatly enhanced the mechanical properties of the hydrogels [140]. In addition, the HAp nanoparticles provided a supportive environment for cell functions, increasing the bioactivity of the gels.

In our current work, we assessed the potential of an *in situ* precipitated HAc– nanoHAp hydrogel for application as an injectable soft tissue augmentation product with highly enhanced biocompatibility, volumetric resistance, and *in vivo* longevity. A schematic diagram of our objectives in developing a highly functional nanocomposite filler is presented in **Figure 3.1.1**.

Figure

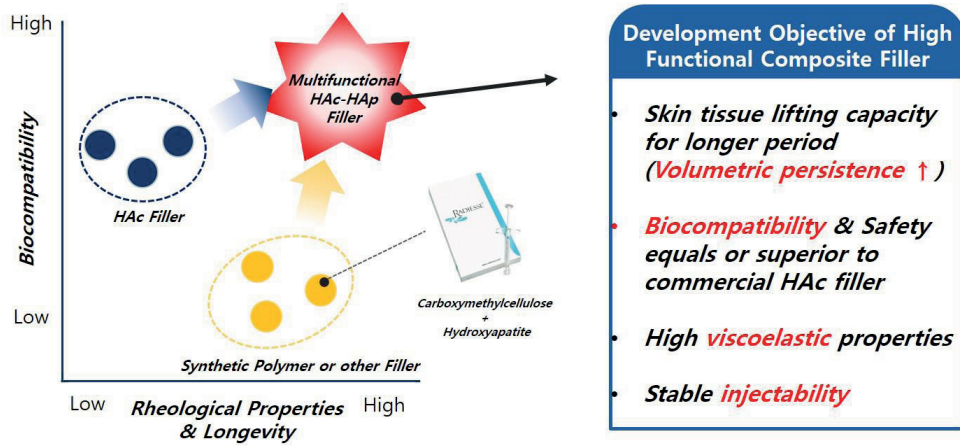


Figure 3.1.1. Objectives for development of highly functional nanocomposite hydrogels for injectable dermal filler applications.

## **3.2. Comparison between Hyaluronic Acid–Hydroxyapatite Composite Hydrogel Dermal Fillers**

### **3.2.1. Introduction**

Herein, two types of HAC–HAp composite fillers were fabricated: HAC–microHAp and HAC–nanoHAp fillers. HAC–nanoHAp was fabricated via *in situ* precipitation of HAp particles with HAC chains and showed high structural homogeneity [98]. For comparison, HAC–microHAp was prepared by mixing microsized HAp particles with HAC. The microstructures and rheological properties of these composite fillers were compared, and the *in vivo* persistence of the fillers in subcutaneous nude mice was demonstrated by monitoring changes in their volume compared with those of pure HAC fillers. The effect of HAp on skin tissue stimulation was also verified by performing a histological analysis.

### **3.2.2. Experimental Procedures**

#### **Preparation and characterization of HAC–HAp composite fillers**

A commercial filler from Q-MED (Restylane, Uppsala, Sweden) was selected for the pure HAC filler. HAC with a molecular weight of 1.8–2.5 MDa was also prepared to fabricate the HAC–HAp composite filler (Biomed, Seoul, Korea). The

HAc–HAp composite fillers were prepared using the crosslinker 1,4-butanediol diglycidyl ether (BDDE) because the pure HAc filler was manufactured using this crosslinker. For the HAc–microHAp filler preparation, HAp microspheres were prepared by spray drying a solution consisting of HAp powder, polyvinyl butyral, and KD-6 (a commercially available polymer surfactant), followed by heat treatment at 500°C for 2 h and at 1200°C for 2 h. HAp microspheres (30 vol.%) with an average size of 20 µm were homogeneously mixed into the 10 w/v% of HAc solution with BDDE in 0.2 N NaOH. The mixture was sealed and stored at 40°C for 12 h to allow gelation. For the HAc–nanoHAp filler fabrication, the HAc hydrogel was prepared following the aforementioned procedure described in **Chapter 2**[141]. The hydrogel was then dialyzed and fully swollen in distilled water at room temperature. Meanwhile, 3 w/v% CaCl<sub>2</sub> solution was prepared and H<sub>3</sub>PO<sub>4</sub> was added at a molar ratio of 1.67. The HAc hydrogel was then immersed in the solution of CaCl<sub>2</sub> and H<sub>3</sub>PO<sub>4</sub> for 2 h and then dipped in 15% NH<sub>4</sub>OH solution for 30 min to precipitate 30 wt% nanoHAp within the hydrogel. All of the HAc–HAp composite hydrogels were washed in PBS and homogenized at 7,000 rpm for 5 min and then autoclaved at 121°C for 30 min to prepare the gel particles for injection through a needle.

The surface morphologies of the hydrogel fillers were examined using FE-SEM (SUPRA 55VP, Carl Zeiss Co., Oberkochen, Germany). Before the characterization, all the samples were lyophilized overnight to maintain the structure of the samples.

## Swelling and rheological properties

The water uptake of the fillers was evaluated in a PBS solution at 37°C. The fillers were dried in a vacuum oven and weighed to obtain the initial dry mass ( $W_i$ ) and then immersed in PBS and re-weighed to obtain the hydrated weight ( $W_h$ ). The swelling ratio of the fillers was calculated as follows:

$$\text{Swelling ratio (\%)} = ((W_h - W_i)/W_i) \times 100.$$

The water content of fillers was also determined from the swelling ratio as follows:

$$\begin{aligned} \text{Water content (\%)} = \\ ((W_h - W_i)/W_h) \times 100 = ((\text{swelling ratio}) / (\text{swelling ratio} + 1)) \times 100. \end{aligned}$$

The rheological measurements were conducted using a rheometer (ARES, Rheometric Scientific, Piscataway, NJ, USA) equipped with a parallel plate geometry (plate diameter of 20 mm). Frequency sweep tests were performed at a constant strain over the frequency range of 1 to 100 rad/s, and  $G'$  was measured as a function of frequency.

## Magnetic resonance image volumetric analysis

Five-week-old female BALB/c nude mice were obtained from a commercial vendor (Orient Bio Inc., Seongnam, Korea) and were fed a standard diet. After resting for 1 week, 200  $\mu$ l of pure HAc, HAc–microHAp, or HAc–nanoHAp was injected between the panniculus adiposus layer and panniculus carnosus of the mice.

The animal experiment was approved by the Institutional Animal Care and Use Committee of Seoul National University.

At weeks 0, 1, 4, 8, and 12, all the groups were examined by magnetic resonance imaging (MRI) volumetric analysis under isoflurane/O<sub>2</sub> (1.5% isoflurane, 1.0 l/min O<sub>2</sub>). A magnetic resonance scanner (Agilent 9.4T/160AS; Agilent Technologies, Santa Clara, CA, USA) and 1-ch coil (Millipede Coil, Agilent Technologies, Santa Clara, CA, USA) were used for the MRI analysis. Both T2-weighted axial and coronal images were obtained. The slice thicknesses of the axial and coronal images were 0.3 and 1.0 mm, respectively. The axial T2-weighted image was used for the volumetric analysis using a SNUH PACS Viewer (Seoul National University, Seoul, Korea).

### **Histological analysis**

At weeks 1, 4, 8, and 12, injected skin biopsies with sizes of 1 cm × 1 cm were extracted and fixed in a 10% formaldehyde solution for 24 h, after which they were embedded in paraffin and sectioned to thicknesses of 6 μm. The sections were stained using hematoxylin and eosin (H&E) and MT stain and were analyzed using image analysis software (ImageJ, National Institute of Health, Bethesda, MD, USA; Leica QWin V3, Leica Microsystems Cambridge, England, UK).

## Statistical analysis

All the data were analyzed using Kruskal–Wallis tests implemented in SPSS version 20.0 (IBM Corporation, Armonk, NY, USA). Step-up Mann–Whitney tests were used with a multiple comparison adjustment. A *P*-value of less than 0.05 was considered statistically significant.

## 3.2.3. Results and Discussion

### Microstructures of HAc–HAp composite fillers

The surface morphologies of the HAc–HAp composite fillers were verified by comparison with that of pure HAc. All the specimens exhibited particulated form, as observed in **Figure 3.2.1**. The average size of the gel particles of the pure HAc filler was 250  $\mu\text{m}$  (**Figure 3.2.1a**). In the HAc–microHAp, HAp microspheres were embedded within the gel particles, as observed in **Figure 3.2.1b**. The HAp microspheres had high sphericity, with an average size of 20  $\mu\text{m}$ . HAc–nanoHAp exhibited a similar morphology as that of pure HAc (**Figure 3.2.1c**). The gel particles of HAc–nanoHAp were also approximately 250  $\mu\text{m}$ . As observed in the high-magnification image (**Figure 3.2.1d**), 200-nm-sized spherical nanoparticles were formed on the surface of the HAc gel particles and were uniformly distributed in the HAc matrix.

## Swelling capabilities and rheological properties

The swelling capacity and stiffness are considered key factors for injectable fillers [142, 143]. In particular, these parameters are closely correlated to the tissue lifting capacity [117]. Thus, the water uptake capacities of the HAC–HAp composite fillers were investigated to elucidate their effective lifting capacities, and the results are presented in **Table 5**. All the HAC–HAp composite fillers absorbed less water (~91%) than pure HAC (~97%), as indicated by their lower swelling ratios at equilibrium. These results indicate that the addition of HAp in the fillers decreased their swelling capacity. In particular, nanosized HAp tightly bonded to the HAC surface, which limited the movement of HAC chains and reduced the swelling capacity [141]. The reduced swelling eventually resulted in an increased stiffness of the fillers; thus, the HAC–HAp composite fillers exhibited stronger performance than pure HAC because of their decreased water uptake capacity.

The filling capacity is also associated with gel stiffness [144]. Stronger gels show greater resistance to deformation, resulting in greater volume restoration [28].  $G'$   $G''$ , which is a key parameter used to describe the gel strength, is plotted as a function of frequency for the HAC–HAp composite fillers and the pure HAC filler in **Figure 3.2.2**.  $G'$  of the pure HAC filler exhibited frequency-dependent behavior and highly deformable gel properties. The HAC–HAp composite fillers exhibited predominantly elastic behaviors, with  $G'$  remaining constant over the entire frequency range. In

particular, HAC–nanoHAp exhibited the highest  $G'$  value. The HAC–HAp composite fillers with higher stabilities are suitable for the correction of deeper wrinkles or severe skin deformation.

### **Volumetric persistence**

The *in vivo* persistence, another key factor for ideal injectable fillers, is highly dependent on the sensitivity of the filler to enzymatic degradation [127]. Thus, a comparative analysis of the degradation profiles of the HAC–HAp composite and pure HAC fillers was performed using animal tests.

MRI techniques are an efficient method for evaluating the evolution of filler volume over time [145, 146]. All of the fillers were easily detectable and their three-dimensional structures were easily visualized using MRI because of their high levels of hydration [147]. The images of pure HAC were the brightest because its main component was water. The T2 images of the HAC–microHAp and HAC–nanoHAp fillers were darker than those of pure HAC because of the presence of HAp; however, the contrast was sufficiently high to distinguish the fillers from skin tissues. The fillers were initially examined immediately after injection, and the remaining volumes after 4 and 12 weeks were also measured. **Figure 3.2.3** reveals the significant difference in residual volume between the HAC–HAp composite fillers and pure HAC. The volume of pure HAC (**Figure 3.2.3a**) significantly decreased over

time, whereas those of HAC–microHAp (**Figure 3.2.3b**) and HAC–nanoHAp (**Figure 3.2.3c**) showed long-lasting performance. The remaining volume over time was measured by calculating the filler area in the T2 images (**Figure 3.2.4**). After 4 weeks, the volume changes started to differ significantly for pure HAC and HAC–nanoHAp ( $P < 0.05$ ). For HAC–nanoHAp, 77% of the volume was retained, whereas only 36% of pure HAC remained after 4 weeks. HAC–microHAp and HAC–nanoHAp showed similar volume maintenance until 4 weeks. After 8 and 12 weeks, the remaining filler volume was significantly higher for HAC–microHAp ( $65 \pm 8\%$ ) and HAC–nanoHAp ( $76 \pm 7\%$ ) than for pure HAC ( $24 \pm 8\%$ ) ( $P < 0.01$ ).

Hydrated HAC gel networks generally decrease in size when exposed to hyaluronidase [148]. The degradation profiles and volume persistence of HAC are assumed to be associated with the swelling capacity. Thus, the aforementioned results may be related to the lower water content in the HAC–HAp composite fillers compared with pure HAC. Less water implies reduced accessibility of HAC specimens to enzymes. Thus, HAC–HAp composite fillers would consequently undergo less degradation than pure HAC.

The HAp microspheres and nanoparticles in the HAC–microHAp and HAC–nanoHAp, respectively, also promoted the persistence of the HAC–HAp composite fillers because of their good stability under physiological conditions. In particular, the HAC–nanoHAp fillers exhibited excellent mechanical strength and high

resistance to enzymes because the nanoHAp particles were strongly bonded to the surface of the HAc hydrogels. In addition to their structural stability, the HAc–HAp composites resulted in significant enhancement to the bioactivity on fibroblast cells in our previous study [141]. Indeed, the *in vitro* results depicted in **Figure 3.2.5** demonstrate that the bioactive HAp particles stimulate fibroblasts to proliferate compared with pure HAc. A comparison of HAc–microHAp and HAc–nanoHAp reveals that the cellular performance is greatly affected by the size of the HAp particles (**Figure 3.2.5a**). Fibroblasts were attached to the HAp microspheres in HAc–microHAp, and the micro-sized cell clusters were examined at high magnification. In HAc–nanoHAp, more fibroblasts were attached on the overall surface. In addition, the cells were highly stretched on HAc–nanoHAp, as observed in the image at high magnification. The nano-sized HAp particles in HAc–nanoHAp were more uniformly distributed than the micro-sized HAp particles in HAc–microHAp. These results show good correlation with the *in vitro* cell proliferation results after 4 days of culturing of the fibroblasts on the hydrogels (**Figure 3.2.5b**). The number of fibroblasts on HAc–nanoHAp significantly increased compared with those on pure HAc and HAc–microHAp, which agrees well with the *in vivo* results showing a higher cell influx to HAc–nanoHAp than to pure HAc or HAc–microHAp. HAp is thought to induce the stimulation of fibroblasts and increase ECM synthesis around the fillers, which eventually enhances the *in vivo* persistence of the fillers.

Histomorphometrical images of the fillers are presented in **Figure 3.2.6**. There was less tissue ingrowth between the pure HAC gel particles; however, more extensive fibrous tissue extended into the HAC–HAp composite filler particles than into pure HAC. In particular, the HAp nanoparticles on the surface of the HAC–nanoHAp fillers significantly induced fibroblast cell migration from the surrounding tissue and led to regeneration of a new tissue structure. These noticeable cell influxes into the HAC–HAp composite filler particles are expected to promote biointegration with the surrounding tissue [81, 111, 149]. In addition, mechanically strengthened HAC–HAp composite fillers might have positive effects on fibroblasts with respect to stretching for robust collagen synthesis [150, 151]. Thus, collagen network reinforcement in the area injected with HAC–HAp composite fillers resulted in improved performance compared with pure HAC with respect to localization at the injection site and prolonged volume maintenance.

### **Bioactivity on the dermis**

The biological responses on the dermis were histologically examined to predict the effect of the addition of HAp in the fillers on the biocompatibility and bioactivity. The dermal thickness after filler injection was analyzed using H&E staining. The dermal thicknesses of all of the HAC–HAp composite fillers were significantly increased compared with that of pure HAC after 12 weeks (**Figure 3.2.7a**). The HAC–

microHAp fillers initially showed increases of the dermal thickness (**Figure 3.2.7b**). At week 12, the thickness of the HAc–HAp group was significantly larger than that of the pure HAc group ( $P < 0.01$ ). In the dermal microenvironment, collagen stimulation is directly associated with dermal thickness [80, 152, 153]. Therefore, the collagen distribution was also examined using MT staining, and the results are presented in **Figure 3.2.8a**. Accordingly, at week 1, the HAc–microHAp group initially exhibited accelerated collagen formation and showed more collagen deposition than the pure HAc group (**Figure 3.2.8b**). At weeks 8 and 12, the collagen area of the HAc–nanoHAp group was significantly larger than that of the pure HAc group ( $P < 0.01$ ). A greater dermal thickness along with highly formed collagen is highly associated with increased cell proliferation, which eventually enhances the dermal structure [80]. These biological results corroborate the notion that HAp particles in HAc–HAp composite fillers activate fibroblast proliferation and ECM synthesis [52, 74]. In particular, nanoHAp particles have better effects on ECM stimulation than microHAp over a longer period because they have a larger surface area exposed to the dermal environment. Nano-sized HAp particles appear to provide effective interference for various proteins and growth factors that promote cell growth and tissue formation. However, further analyses are necessary to verify the mechanism of ECM synthesis via HAp at the genetic level.

### **3.2.4. Conclusion**

The effectiveness of HAc–HAp composite fillers in improving the mechanical strength and durability compared with pure HAc was systematically demonstrated. The HAc–HAp composite fillers exhibited enhanced long-lasting properties as well as beneficial biological properties. Accordingly, the HAc–HAp composite fillers are great candidates for soft tissue augmentation. However, further research should be conducted to determine the mechanism of dermal ECM synthesis considering the receptor-mediated interactions between HAc–HAp composite fillers.

## Table

**Table 5. Water content of pure HAc, HAc–microHAp, and HAc–nanoHAp fillers.**

<b>Filler</b>	<b>Water content [vol%]</b>
<b>Pure HAc</b>	$96.7 \pm 0.20$
<b>HAc–microHAp</b>	$91.8 \pm 4.13$
<b>HAc–nanoHAp</b>	$91.0 \pm 1.60$

## Figures

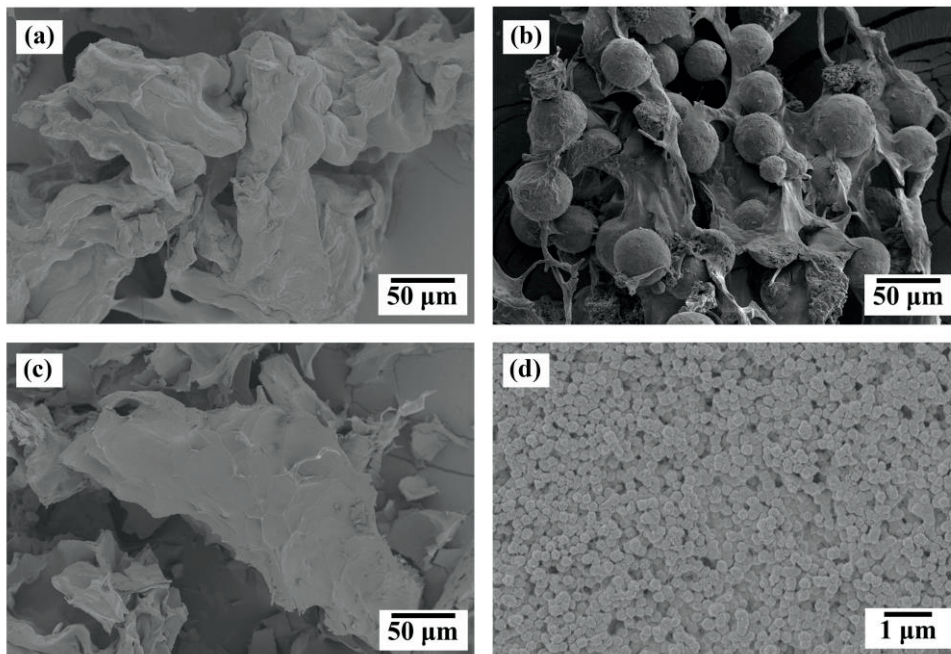


**Figure 3.2.1. Surface morphologies of (a) pure HAc, (b) HAc–microHAp, and (c) HAc–nanoHAp and (d) a high-magnification image of HAc–nanoHAp ( $\times 30k$ ).**

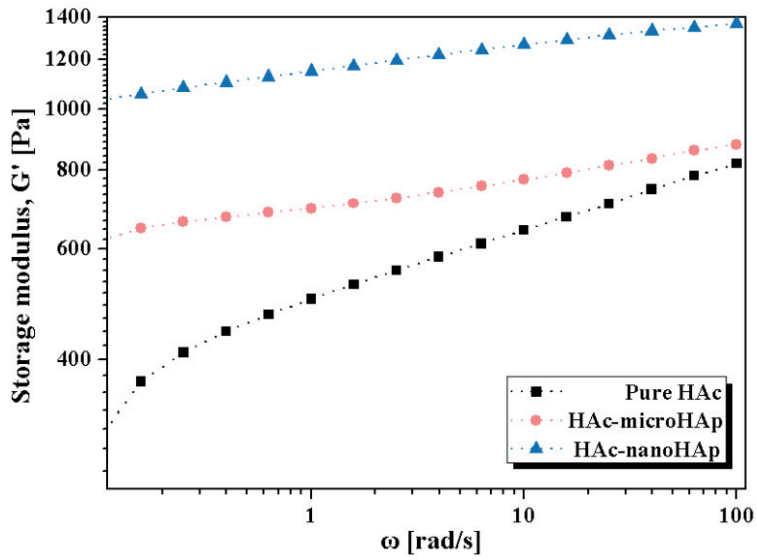


Figure 3.2.2.  $G'$  of pure HAC, HAC-microHAp, and HAC-nanoHAp as a function of frequency.

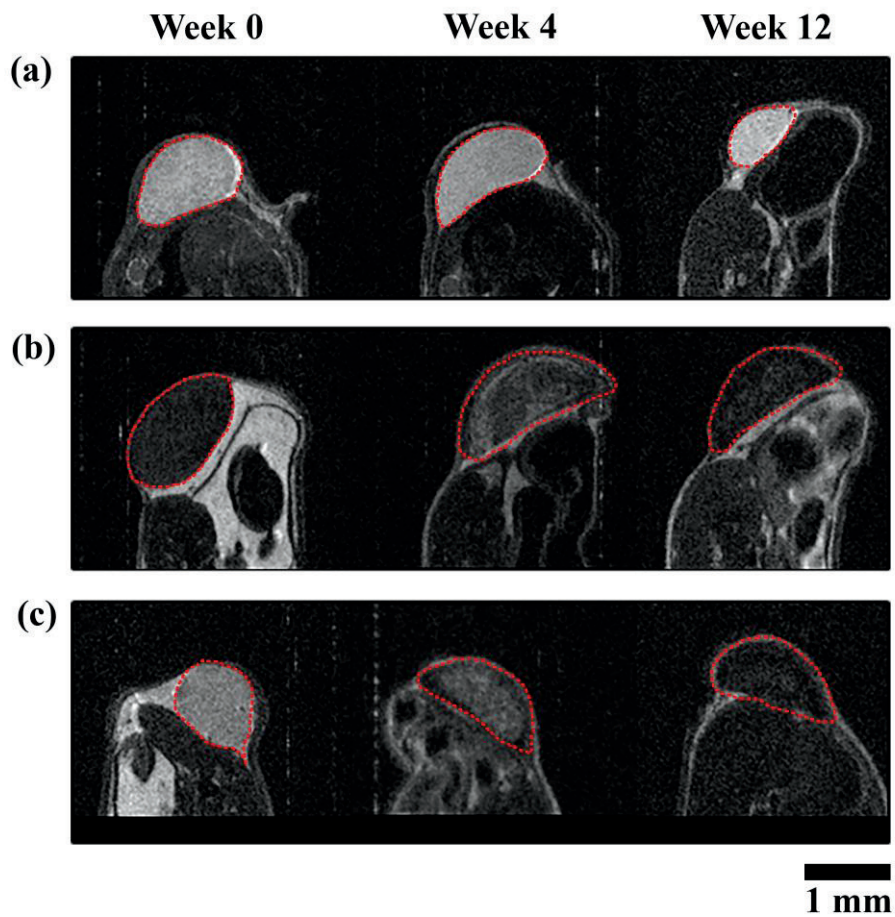
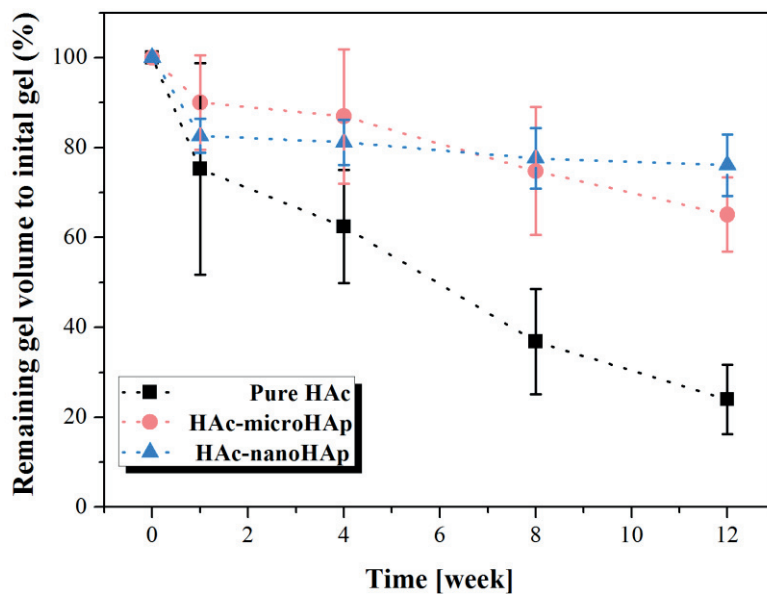


Figure 3.2.3. Axial T2 images of (a) pure HAc, (b) HAc-microHAp, and (c) HAc-nanoHAp at 0, 4, and 12 weeks after filler injection.



**Figure 3.2.4. Remaining gel volume as a function of time until 12 weeks based on MRI volumetric analysis.**

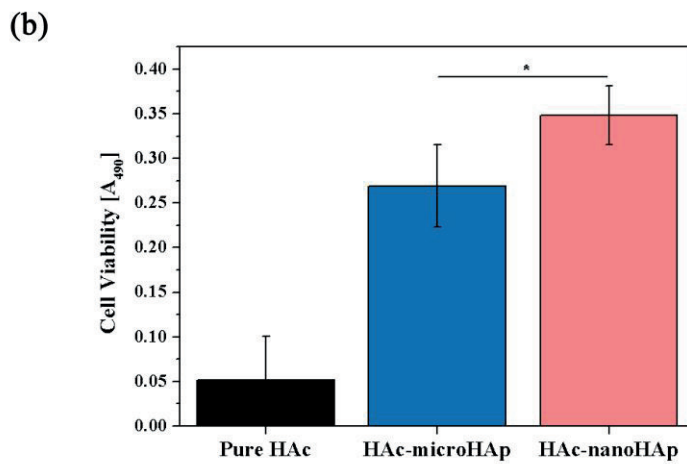
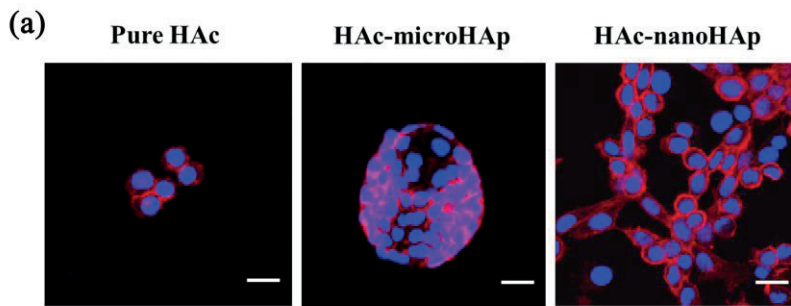
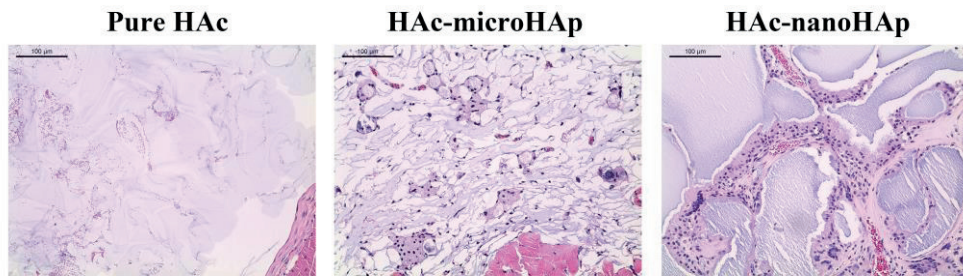


Figure 3.2.5. (a) *In vitro* cell attachment images of pure HAc, HAc–microHAp, and HAc–nanoHAp using L929 fibroblast cells. First and second row scale bars = 50 and 20  $\mu\text{m}$ , respectively. (b) Cell viability after 4 days of culturing on pure HAc, HAc–microHAp, and HAc–nanoHAp (\* $P < 0.05$ ).



**Figure 3.2.6. Filler morphological analysis by H&E staining at 8 weeks. Scale bars = 100 µm.**

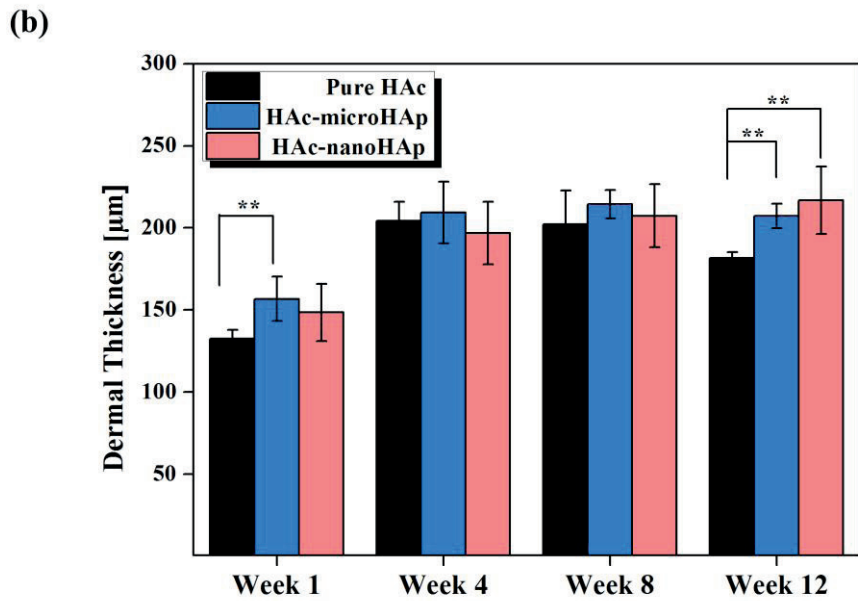
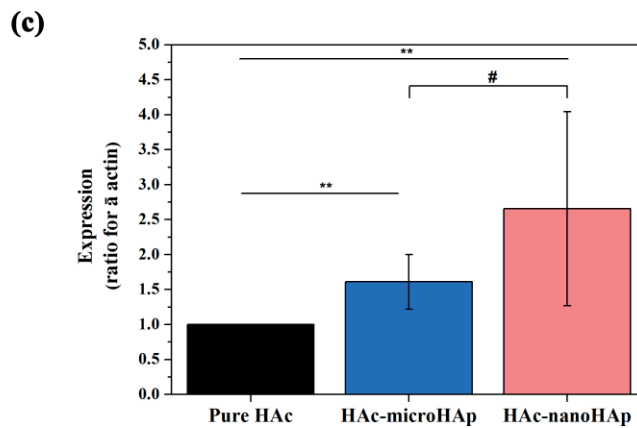
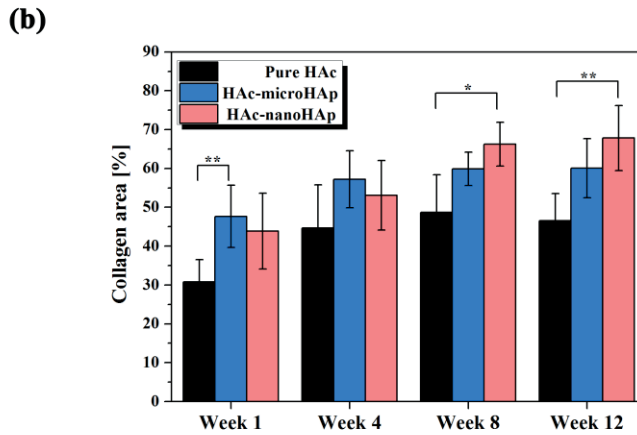
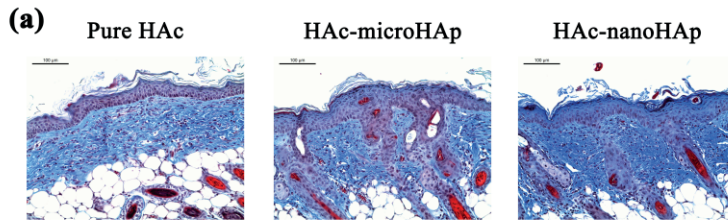


Figure 3.2.7. (a) Analysis of dermis thickness using H&E staining at 12 weeks.

Scale bars = 100 μm. (b) Analysis of dermal thickness using ImageJ (\*\*P<0.01).



**Figure 3.2.8. (a)** Analysis of collagen distribution using MT staining at 12 weeks. Scale bars = 100 μm. **(b)** Analysis of collagen area in the dermis (\*P<0.05, \*\*P<0.01). **(c)** Procollagen gene expression at 8 weeks (\*\*P<0.01, #P<0.5).

## **3.3. Wrinkle Improvement Using Hyaluronic Acid–Hydroxyapatite Nanocomposite Hydrogel Fillers**

### **3.3.1. Introduction**

In this study, the effect of HAC–nanoHAp composite fillers on wrinkle improvement was analyzed using a photo-aged animal model. For this purpose, the rheological performance (gel stiffness and cohesiveness) was examined to verify the effect of the mechanical properties of the composite hydrogels on the skin tissue. The filler performance under skin was also evaluated using MRI to examine the lateral diffusion after injection. Finite element modeling was conducted to investigate the correlation between the gel stiffness and lifting effect of the fillers. Furthermore, the biological response of the HAC–nanoHAp filler was analyzed to evaluate the efficacy of HAp nanoparticles on dermal tissue stimulation.

### **3.3.2. Experimental procedures**

#### **Characterization and mechanical properties of hydrogels**

HAC–nanoHAp hydrogels were fabricated following an identical process as that introduced in **Chapter 3.2**. Briefly, pure HAC hydrogel was prepared after being crosslinked by BDDE and was then immersed in a solution of  $\text{CaCl}_2$  and  $\text{H}_3\text{PO}_4$ . Subsequently, the hydrogel was dipped in 15%  $\text{NH}_4\text{OH}$  solution for 30 min to

precipitate HAp nanoparticles within the hydrogel. All the hydrogels for the rheological tests and *in vivo* analysis were homogenized at 7000 rpm for 5 min and autoclaved at 121°C for 30 min.

The morphologies of the hydrogels were examined using FE-SEM (SUPRA 55VP, Carl Zeiss Co., Germany). Before their characterization, the samples were lyophilized overnight to maintain the structure of the samples.

The actual HAp content and chemical stability of the composite hydrogels were quantified and analyzed using TGA (Discovery TGA, TA instruments Co., USA). Before the analysis, all the hydrogel samples were completely dried in air and heated to 1000°C at a rate of 20°C/min under an N<sub>2</sub> atmosphere.

The rheological behavior of the hydrogels was assessed using a controlled strain rheometer (ARES, Rheometric Scientific, USA). Hydrogel samples with diameters of 20 mm and thicknesses of 1 mm were prepared. Frequency sweeps were performed in the angular frequency range of 0.1 to 100 rad/s at a strain of 1% in the linear region, and strain sweeps were performed in the strain range of 0.1% to 200%. In addition, the hydrogels were also evaluated in the compressive mode to evaluate the gel cohesiveness. First, 0.2 mL of the hydrogels was placed between two 20-mm-thick plates. In normal force mode, the upper plate was placed in contact with the hydrogels and was then lowered toward the bottom plate, thus compressing the hydrogel to 70% compression. The resulting normal force was measured during the

experiment.

### ***In vivo* cohesivity measurements using magnetic resonance imaging**

*In vivo* filler injection of 5-week-old male BALB/c nude mice from KOSA Bio Inc. (Seongnam, Korea) was conducted. At hours 0.5, 1, 2, and 24 and on day 7, all the fillers were examined using MRI surface analysis under isoflurane/O<sub>2</sub> (1.5% isoflurane, 1.0 l/min O<sub>2</sub>). A magnetic resonance scanner (Agilent 9.4T/160AS, Agilent Technologies, Santa Clara, CA, USA) and 1-ch coil (Millipede Coil, Agilent Technologies) were used for the MRI analysis. T2-weighted axial images were obtained using a slice thickness of 1.0 mm. The axial images were used for the lateral diffusion analysis using a SNUH PACS Viewer. T2-parametric images were obtained using a multispin-echo sequence (FSE: TR/TE= 6000/25 ms with 15 echos) with a 35-mm-diameter dedicated surface coil. The images were evaluated using the image analysis software MATLAB (Mathworks, Natick, MA, USA).

### **Wrinkle improvement observation using UV-irradiated *in vivo* models**

Six-week-old female BALB/c nude mice were treated with ultraviolet-B (UVB) rays 6 times a week for 6 weeks following the irradiation procedures introduced in our previous study [154]. The wavelengths were between 290 and 320 nm, the radiation source was provided by 4 UVB lamps (TL 20W/12 RS; Koninklijke Philips

N.V., Eindhoven, The Netherlands), and Kodacel (TA401/407; Eastman Kodak Company, Rochester, NY) was used to filter the ultraviolet-C (UVC) wavelengths [154]. The UVB-treated mice were then classified into three groups: those treated with no therapy, commercial pure HAc from Q-MED (Restylane, Uppsala, Sweden), and HAc–nanoHAp filler. The wrinkle improvement results were compared before and 4 weeks after injection.

Replicas of the upper back skins were created using a silicon-based impression material (Courage and Khazaka Electronic GmbH, Cologne, Germany). The replicas were cut into circular 1-cm-diameter pieces, which were processed to ensure that they were flat. Before and after injection, the skin biopsies with size of 1 cm × 1 cm were fixed in a 10% formaldehyde solution for 24 h and were then embedded in paraffin and sectioned at 6 μm. The sections were stained using H&E, MT, and Verhoeff–Van Gieson stains and were analyzed using image analysis software (ImageJ, National Institute of Health, Bethesda, MD, USA; Leica QWin V3, Leica Microsystems Cambridge, England, UK).

For immunohistochemistry analysis, tissue sections were cut and placed on microscope slides. An automated immunohistochemistry stainer (Discovery XT, Ventana Medical Systems, Inc., Tucson, AZ, USA) was used to stain the slides, and the Ventana ChromoMap Kit (Ventana Medical Systems) was used for detection. The tissue sections were deparaffinized, and CC1 standard (a buffer containing Tris,

borate, and ethylenediaminetetraacetic acid, pH 8.4) was used to retrieve the antigen. Inhibitor D (3% H<sub>2</sub>O<sub>2</sub>, endogenous peroxidase) was plugged in for 4 min at 37°C. The slides were incubated with vimentin (Abcam, Cambridge, MA, USA) for 32 min and with OmniMap anti-rabbit horseradish peroxidase as a secondary antibody for 20 min. The slides were incubated in diaminobenzidine using a H<sub>2</sub>O<sub>2</sub> substrate for 8 min at 37°C followed by hematoxylin bluing reagent counterstaining. A Tris buffer at pH 7.6 was used as the washing solution. The stained slides were evaluated using image analysis software (Leica QWin V3 and Leica Microsystems CMS GmbH, Wetzlar, Germany).

### **TEM examination of *in vivo* biological specimens with hydrogel fillers**

Skin biopsies with the hydrogel fillers 5 and 8 weeks after injection were further analyzed using TEM. After fixation with Karnovsky's solution, the samples were washed with 0.05 M sodium cacodylate buffer twice for 10 min each. They were post fixed with a solution of 2% of osmium tetroxide and 0.1 M cacodylate buffer in sequence. The samples were then dehydrated with a gradually increasing concentration of ethanol from 30% to 90%. To ensure complete ethanol saturation, the ethanol content of the dehydration solution was increased to 100%, and the dehydration was performed three times. En bloc staining using 0.5% uranyl acetate solution was conducted before the gradual dehydration procedures. The samples

were then passed through propylene oxide, which is a transition solvent, before being infiltrated and embedded in Spurr's resin. After embedding the resin, the blocks were sectioned by an ultramicrotome and sections with thicknesses of 50–70 nm were collected on a metal mesh grid. The internal structure of the dermis above the hydrogel fillers was examined using TEM (JEM1010, JEOL, Japan).

### Statistical analysis

All the data were analyzed using the Kruskal–Wallis test with SPSS software version 20.0 (IBM Corporation, Armonk, NY, USA). Step-up Mann–Whitney tests were used with a multiple comparison adjustment. A *P*-value of less than 0.05 was considered statistically significant.

### 3.3.3. Results

#### Characterization and rheological properties of HAc–nanoHAp

**Figure 3.3.1** shows the microstructures of the hydrogel fillers. The pure hydrogel had a highly porous structure (**Figure 3.3.1a**). HAc–nanoHAp also exhibited an interconnected porous structure, as observed in **Figure 3.3.1b**, implying that the network of hydrogels was maintained after the *in situ* precipitation procedure. At higher magnification, however, the morphology of the pure HAc hydrogel was distinctly different from that of the HAc–nanoHAp. The pure HAc had a smooth

surface, as observed in **Figure 3.3.1c**, whereas a high density of nanosized spherical particles was observed on the HAC–nanoHAp surface (**Figure 3.3.1d**). A uniform distribution of HAp nanoparticles with an average size of 200 nm was observed on the surface of HAC–nanoHAp. In this system, we changed the concentration of the CaCl<sub>2</sub> and H<sub>3</sub>PO<sub>4</sub> solution to obtain different contents and sizes of the precipitated HAp particles. A gradual increase in quantity and size was observed in the high-magnification images. The particle content was similar when the CaCl<sub>2</sub> concentration was controlled from 1 to 3 w/v%. However, the CaCl<sub>2</sub> concentration affected the nanoparticle size during precipitation process. The size distribution decreased and the average particle size increased with increasing CaCl<sub>2</sub> concentration from 1 to 3 w/v%. The total amount of HAp was calculated under the assumption that the particles were spherical. It was concluded that smaller particles were precipitated in larger numbers in the HAC matrix, with the total amount of HAp remaining the same. Increasing the concentration of precursors for the *in situ* precipitation played a more critical role in increasing the nanoparticle size than increasing the content.

The rheological properties of the hydrogel particulates after granulation were characterized using a rheometer (**Figure 3.3.2a**). For all frequencies, great enhancement of G' was observed for HAC–nanoHAp compared with that of pure HAC (**Figure 3.3.2b**). From the rheological kinetics results in strain sweep mode,

depicted in **Figure 3.3.2c**, the strain point of HAc–nanoHAp, at which the gel starts to collapse, was significantly higher than that of pure HAc, implying higher structural integrity. The interaction between the gel particles was also analyzed in compressive mode, as shown in **Figure 3.3.2d**. The compressive force–displacement profiles are shown after 70% compression in unconfined mode. HAc–nanoHAp had a higher modulus than pure HAc. In addition, the cohesivity index of HAc–nanoHAp was 50-fold higher than that of pure HAc, which implies that the HAp nanoparticles remarkably affect the gel cohesiveness, affecting the friction between the surfaces of the gel particles during compressive deformation. These rheological results indicate that the uniformly precipitated nanoHAp enhanced the structural integrity of the hydrogels, demonstrating their great ability of maintaining their shape under force. Overall, among the pre-existing products, HAc–nanoHAp exhibit the best lifting capacity thanks to the combination of its high G' and high gel cohesiveness, as depicted in **Figure 3.3.3**.

### **Biophysical performance of HAc–nanoHAp on dermal matrix**

The HAc–nanoHAp fillers were applied to an *in vivo* animal model to determine the effect of gel stiffness on their behaviors under skin compared with that of the pure HAc fillers. The lateral diffusion of both fillers was visualized using MRI, which helps explain the good correlation between the rheological performance and

*in vivo* gel diffusion. As observed in **Figure 3.3.4a**, the pure HAc first diffused laterally and was then progressively resorbed, whereas HAc–nanoHAp showed significantly less flow, and they both maintained their original shape relatively well at the injected sites. The lateral diffusion ratio of pure HAc dramatically increased even in the early stage, whereas that of HAc–nanoHAp decreased over time (**Figure 3.3.4b**). Notably, the filler and dermal tissue modification were clearly observed in the T2 parametric images (**Figure 3.3.4c**) over time because HAc contains a large amount of water and the transverse relaxation time of water (200 ms) differs distinctly from that of dermal tissues (35 ms) [155, 156]. The T2 relaxation time of HAc–nanoHAp was much lower than that of pure HAc because of the presence of HAp. In addition, not only the swelling ratio but also the bioactivity of the fillers were determined from the T2 signal graph and images. A shorter T2 time was observed for HAc–nanoHAp than for pure HAc, indicating a smaller swelling ratio for HAc–nanoHAp because of the nanoparticles. The dermal tissue also had a lower T2 value over time, especially for HAc–nanoHAp, implying that it more greatly induced ECM formation surrounding the fillers than pure HAc.

Computational modeling was also performed, with the load applied from the top part of the skin, to verify the gel stiffness effect on wrinkle improvement using mesh-generated wrinkle images (**Figure 3.3.5**). A larger stress distribution was observed on the pure HAc filler and surrounding tissues than on HAc–nanoHAp, as shown in

**Figure 3.3.6.** Pure HAc exhibited 20% deformation in the vertical direction and laterally diffused, with a lateral ratio of 1.10:1, whereas HAc–nanoHAp only exhibited 9% deformation with a lateral ratio of 1.04:1. Because of the high stiffness of HAc–nanoHAp, there was less modification of the filler shape, resulting in significant retention of its lifting capacity. In contrast, the pure HAc filler was greatly flattened because of the loss of skin elasticity.

### **Wrinkle observation and biological performance of HAc–nanoHAp on dermal matrix**

The wrinkles 4 weeks after implantation were compared with those of the pre-injection samples by examining the replicas of the skin and histologically stained images. Deep wrinkles were clearly observed for the UVB-treated skin, as shown in **Figure 3.3.7a**. After filler treatment, all the samples treated using pure HAc (**Figure 3.3.7b**) and HAc–nanoHAp (**Figure 3.3.7c**) were flattened compared with the UVB-treated and untreated samples (**Figure 3.3.7d**). Quantitative analysis of the wrinkles was conducted by measuring the wrinkle depth from the cross-sectioned histological images. A significant decrease in the wrinkle mean depth was observed when using HAc–nanoHAp compared with pure HAc, as depicted in **Figure 3.3.7e** (\* $P < 0.05$ ).

The wrinkled skins, dermal thickness, and collagen fibers of the wrinkled skins were evaluated 4 weeks after injection. A significant increase of the dermal thickness

was observed for the UVB-treated skin (**Figure 3.3.8a**) because of the severe damage that occurred to the collagen fibers and the increase of abnormal elastic fibers, leading to fibroelastosis. After filler injection, a significant decrease in skin thickness was observed for both filler treatment groups (**Figure 3.3.8b–c**). The filler-treated samples had similar thicknesses as the untreated samples (**Figure 3.3.8d**). The thickness of the HAC–nanoHAp group was significantly smaller than that of the UVB-treated group (\*\*  $P < 0.01$ ), as observed in **Figure 3.3.8e**, implying that nanoHAp regenerated normal ECM matrix. The MT-stained images (**Figure 3.3.9**) showed the collagen fibers in the dermis. Compared with the UVB-treated group (**Figure 3.3.9a**), the pure HAC group (**Figure 3.3.9b**) and HAC–nanoHAp group (**Figure 3.3.9c**) had similar collagen areas as the untreated group (**Figure 3.3.9d**). Quantitative analysis of the collagen area from the MT-stained images revealed a significant increase in the collagen area after HAC–nanoHAp injection compared with both the UVB-treated and pure HAC groups (**Figure 3.3.9e**) (\*  $P < 0.05$ ). Therefore, the HAp nanoparticles in the HAC–nanoHAp filler remarkably enhanced the dermal structure and resulted in high collagen deposition under deep furrows [52]. The elastic fiber areas (black area in the dermis) (**Figure 3.3.10**) were also examined using Verhoeff–Van Gieson staining. After UVB irradiation, the elastic fiber areas in the dermis significantly decreased (**Figure 3.3.10a**) (\*  $P < 0.05$ ). Both filler-treated groups (**Figure 3.3.10b–c**) had higher densities of elastic fiber areas than the

untreated groups (**Figure 3.3.10d**). The proportion of elastic fiber area of the HAc–nanoHAp group was larger than that of the pure HAc group (**Figure 3.3.10e**) (\*\*  $P < 0.01$ ), indicating that nanoHAp exhibited a great ability to regenerate elastic fibers. It can be concluded that HAc–nanoHAp accelerated the substitution of normal tissue matrix for abnormal tissue because of the UVB treatment.

### **3.3.4. Discussion**

The main factors contributing to improvement of skin wrinkles are related to physical properties of the injectable fillers, specifically, the volumetric longevity and gel stiffness [117, 129, 142]. In particular, the duration of the wrinkle improvement can be predicted based on the gel persistence and biostability [139]. In our previous study, 60% of the HAc–nanoHAp filler volume was retained 4 weeks after injection into nude mouse skin, whereas drastic degradation of pure HAc was observed, with only 40% of the volume retained [139]. These findings indicate that the HAp nanoparticles in HAc–nanoHAp imposed a physical barrier to enzymatic breakdown, which contributed to their high resistance. Thus, the incorporation of HAp nanoparticles made the gel more durable than pure HAc under physiological conditions. The HAc–nanoHAp-treated skins resulted in better wrinkle improvement thanks to the increased longevity and greater volumizing effect of the HAc–

nanoHAp fillers than pure HAc. Therefore, HAc–nanoHAp is suited to lifting zones with deep furrows and high levels of muscle activity, such as nasolabial folds.

Lifted skin generally tends to move to its original state and thus gradually applies a downwards force to injected fillers, which induces gel deformation.[146] Thus, gels with higher stiffness (higher  $G'$ ) such that they can maintain their shape and remain localized at the injected site can be introduced to correct wrinkles and deep folds [128]. Pure HAc with lower gel stiffness was observed to be largely deformed into a flattened shape, whereas HAc–nanoHAp exhibited smaller deformation, maintaining its shape. This result is correlated to the quantified  $G'$  results. HAc–nanoHAp exhibited stronger structural integrity than pure HAc, and the stronger gel–gel interaction of HAc–nanoHAp restricted filler movement under the application of a shear force to the skin tissue, with the filler appearing less diffuse in the lateral direction. Because of the severe deformation in shape, the pure-HAc-treated wrinkles had a minimal effect on filling the volume; however, HAc–nanoHAp provided more efficient skin lifting.

Synergistic effect of HAc-nanoHAp filler can be also highlighted in terms of not only improving the wrinkles, but also enhancing structural support the dermal matrix. In particular, HAc-nanoHAp filler showed excellent gel cohesiveness as depicted in **Figure 3.3.2**, resulting in high structural integrity with strong resistance to skin friction. However, the bioactivity of the filler can be generally decreased if its

cohesivity is too high, since there is insufficient space for the cells and tissue to be infiltrated into filler gel particles. Bioactivity of HAc-nanoHAp filler can be complemented by the exposure of high density of HAp nanoparticles on the surface of the hydrogel filler. This structural morphology is provided by in-situ precipitation process. Indeed, HAc-nanoHAp filler fabricated through *in situ* precipitation showed big difference between simply mixed composite filler in terms of uniformity and the appearance of HAp particles in the HAc matrix. Due to uniform distribution of HAp nanoparticles on the surface of filler matrix, biointegration with the surrounding tissue is highly promoted, consequently resulting in even more enhanced performance with prolonged volume maintenance.

An additional factor affecting wrinkle improvement is the bioactivity of the filler materials, which is a measure of their ability to stimulate the regeneration of surrounding tissue. HAp induces fibroblast proliferation; thus, we also performed immunostaining using vimentin, which is a fibroblast marker. The fibroblasts were highly proliferated after 8 weeks in both groups, and the HAc–nanoHAp filler resulted in a significantly larger vimentin area than that of pure HAc. According to the vimentin area results, the HAc–nanoHAp filler increased the biosynthetic capacity of dermal fibroblasts (**Figure 3.3.11**). This finding is directly associated with the reconstruction of a physiologic environment, such as the synthesis of collagen [157]. The fibroblasts surrounding HAc–nanoHAp demonstrated a 2.5-

fold-higher level of type I procollagen gene expression compared with that of the pure-HAc-treated skins (**Figure 3.3.12**). A high density of collagen production following HAc–nanoHAp filler injection was also observed in highly organized forms, as depicted in **Figure 3.3.13**. This structural support of the dermal ECM by HAp nanoparticles generated a tightening effect on the collagen fiber network in accordance with the stretched fibroblasts [151]. Thus, the firmness of the dermal tissue was improved as the thickness of dermal tissue was increased. The HAp nanoparticles also stimulated the level of elastic fibers, which play a role in determining the skin elasticity. The increased content of ECM components resulting in wrinkle improvement compensated for the skin laxity caused by the gel stiffness and skin deformation, which explains the difference in the wrinkle ratio observed for the *in vivo* results and simulation data.

### **3.3.5. Conclusion**

HAc–nanoHAp hydrogel fillers were successfully fabricated via *in situ* precipitation, and their effectiveness on improving the rheological properties and dermal biomechanics were further evaluated. Based on *in vivo* analysis using a wrinkled skin model, we achieved high lifting capacity using the HAc–nanoHAp hydrogel fillers as a result of enhanced mechanical properties compared with those of the pure HAc filler. Furthermore, the biocompatibility of HAc–nanoHAp was

analyzed in an *in vivo* test, showing highly stimulated ECM synthesis in the dermal environment. Consequently, it is expected that HAC–nanoHAp hydrogels have great potential for soft tissue augmentation application, as they show great wrinkle lifting performance and enhanced bioactivity.

## Figures

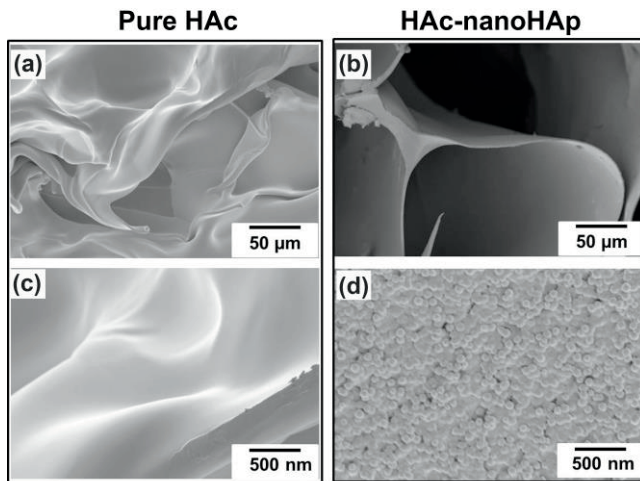


**Figure 3.3.1. Cross-sectional SEM images of (a) pure HAC with high porosity and (b) HAC–nanoHAp. High-magnification images of (c) pure HAC with a smooth surface and (d) HAC–nanoHAp containing uniformly distributed HAp nanoparticles.**

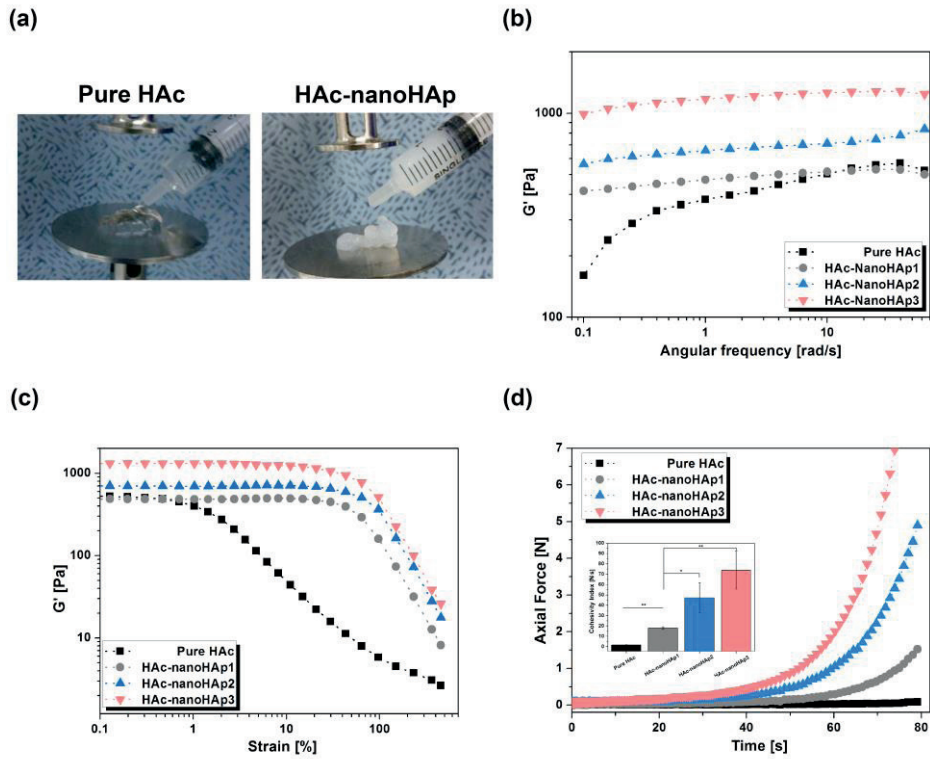


Figure 3.3.2. (a) Photographs of fillers on the rheometer plate.  $G'$  of fillers as a function of (b) angular frequency and (c) strain. (d) Axial force graph of fillers in unconfined mode under compression.

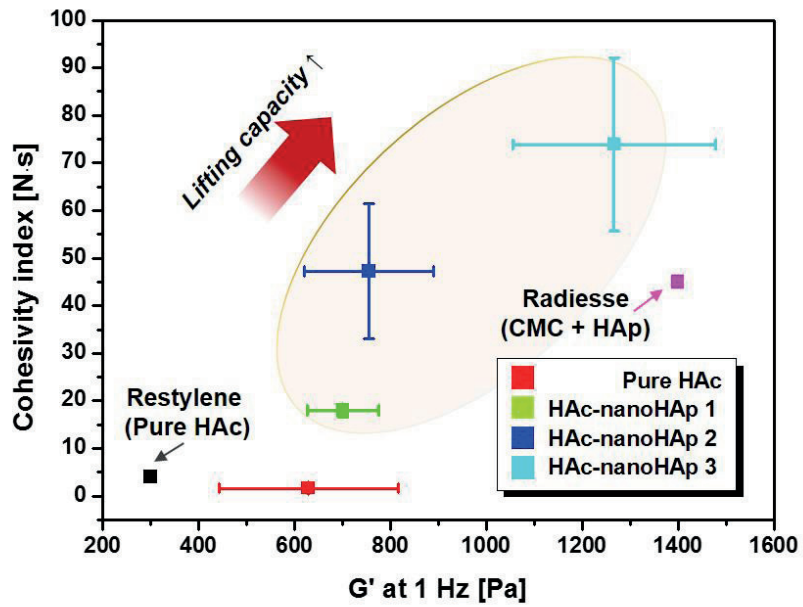
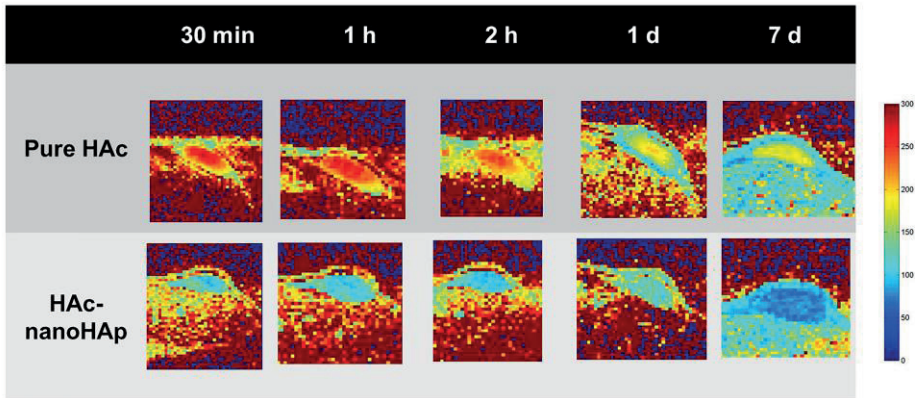
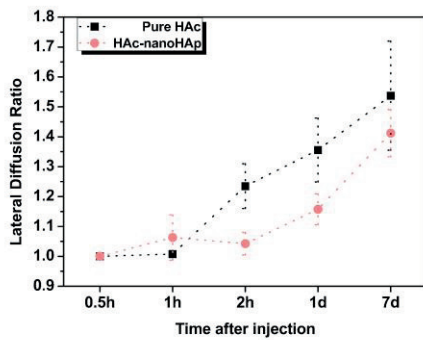


Figure 3.3.3.  $G'$  and cohesivity index of commercial filler products and HAC-nanoHAp to illustrate their lifting capacities.

(a)



(b)



(c)

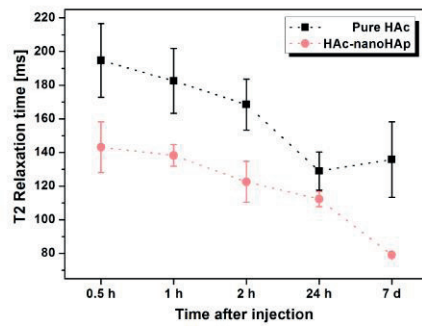
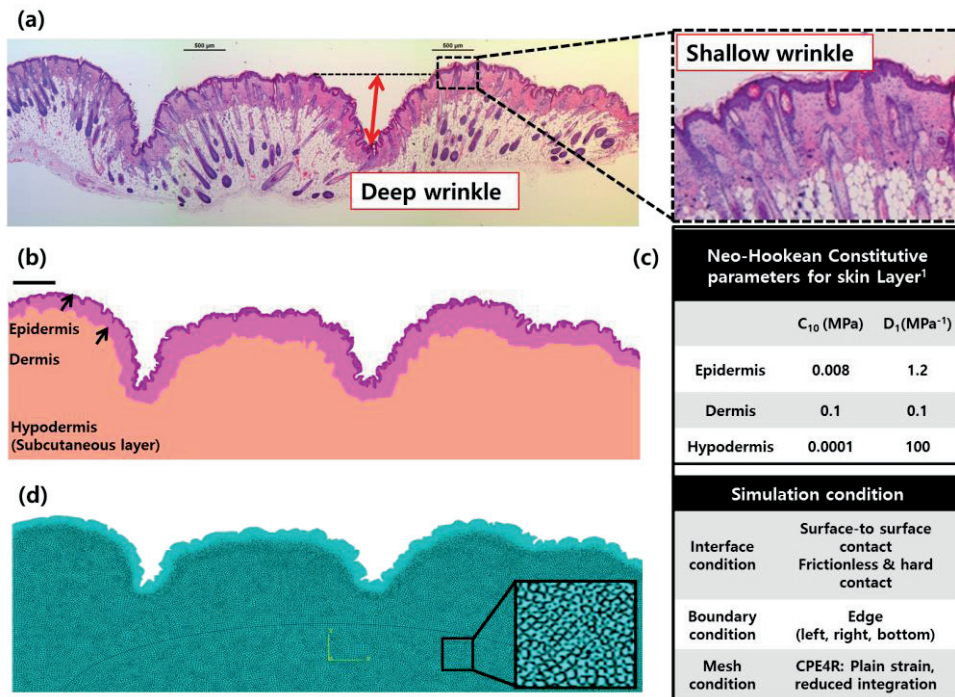


Figure 3.3.4. (a) T2 parametric images showing fillers and dermal tissue modification and lateral diffusion of fillers over 7 days. (b) Lateral diffusion ratio and (c) T2 relaxation time graph of fillers over time.



1. Maria F. et al. / Journal of the mechanical behavior of biomedical materials 49 (2015)

**Figure 3.3.5. (a) H&E stained image showing shallow and deep wrinkles. (b) Illustration of skin layer components obtained using Image J. Scale bar = 500 μm. (c) Constitutive parameters for each skin layer and simulation conditions. (d) Mesh-generated image of each skin layer and injected filler.**

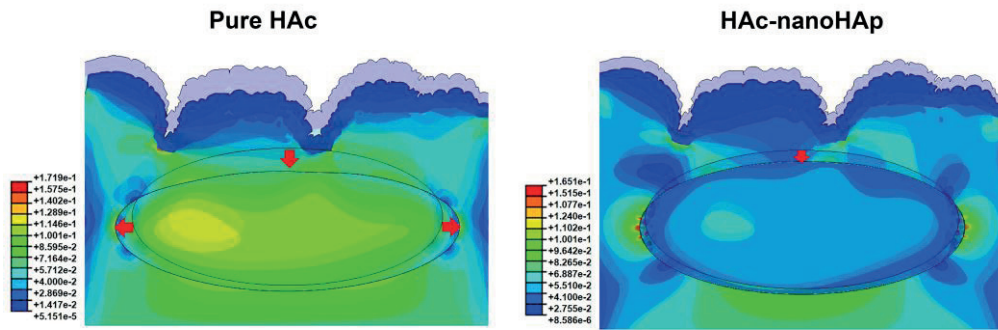


Figure 3.3.6. Color plot of logarithmic strain distribution after simulation for pure HAc and HAc–nanoHAp, showing the gel stiffness effect on wrinkle improvement after loading a normal force on the skin to observe filler deformation in accordance with wrinkle deformation. The red arrow indicates the direction of filler deformation.

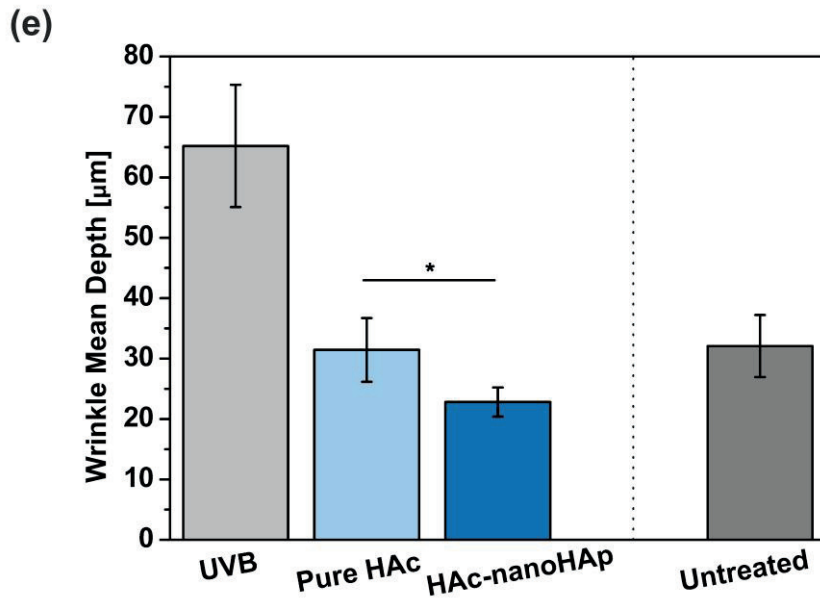
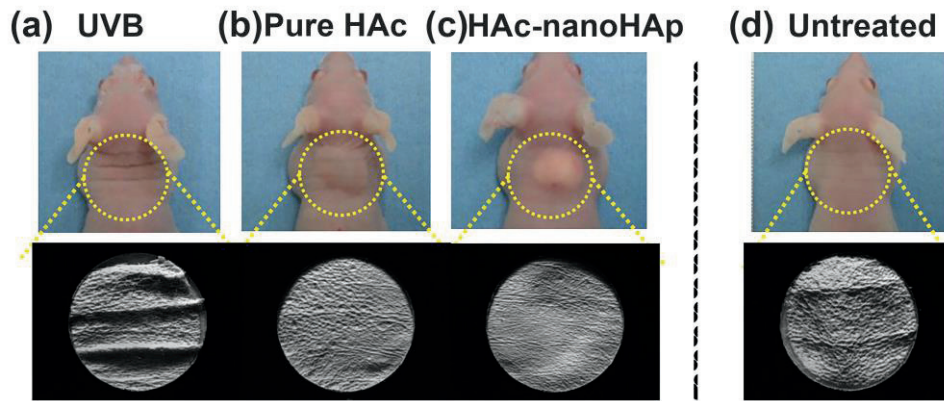


Figure 3.3.7. Examination of wrinkles using skin replica: (a) UVB-treated, (b) pure-HAC-filler-treated, (c) HAC–nanoHAp-filler-treated, and (d) untreated samples. (e) Mean wrinkle depth calculated from histological images. (\* $P < 0.05$ ).

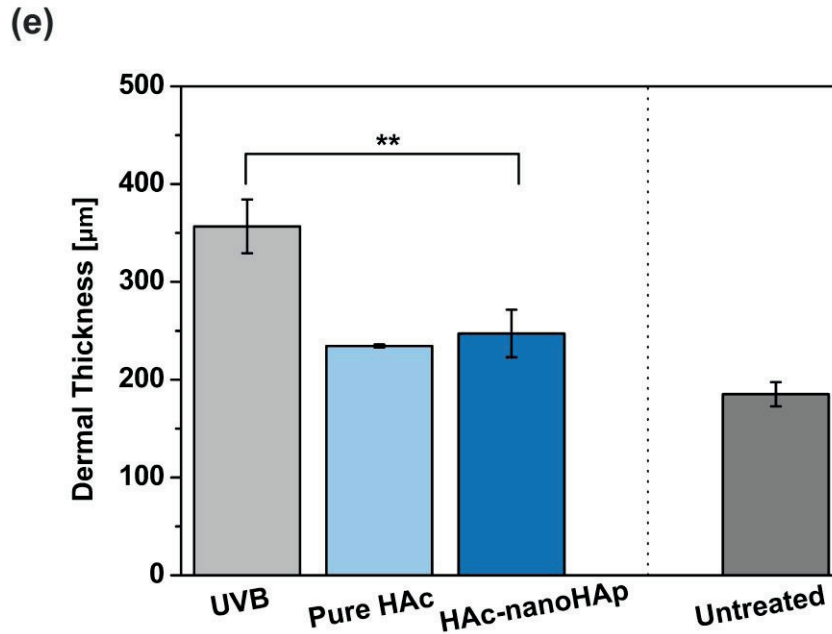
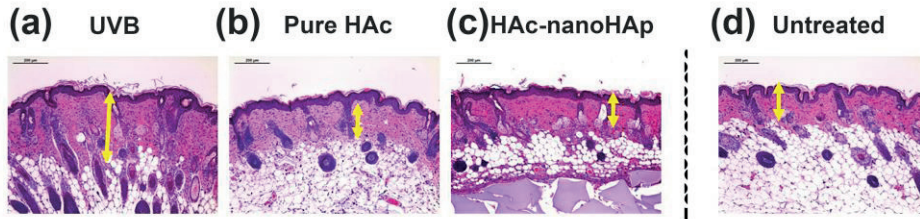


Figure 3.3.8. Images stained with H&E stain (100×): (a) UVB-treated, (b) pure-HAC-filler-treated, (c) HAC–nanoHAp-filler-treated, and (d) untreated skin. (e) Quantification of dermal thickness (\*\* P < 0.01).

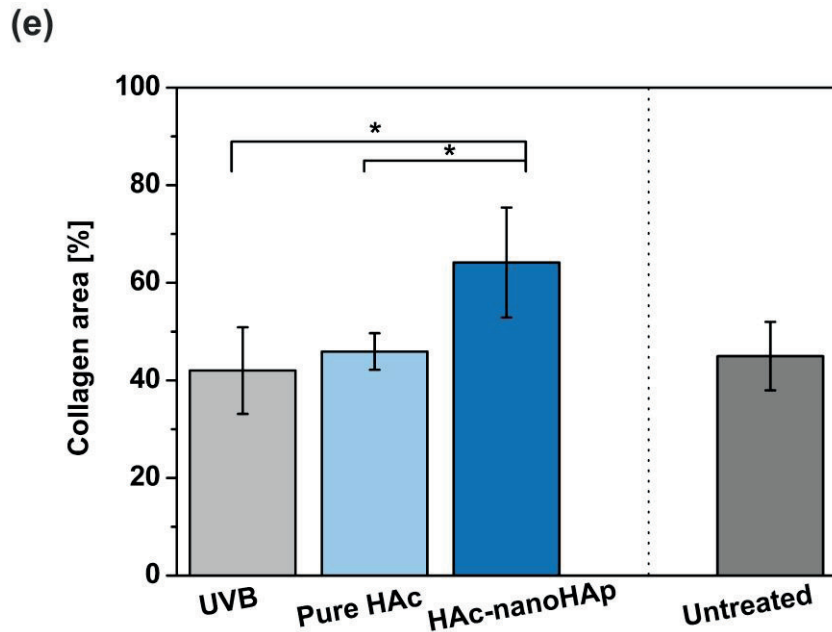
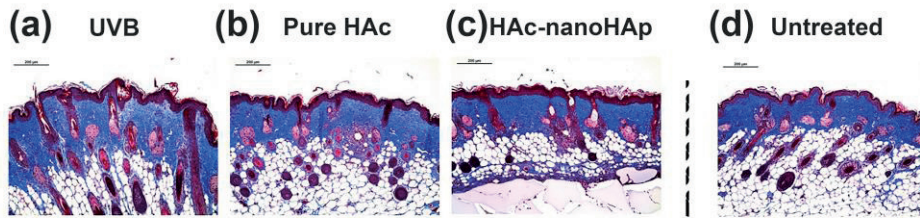
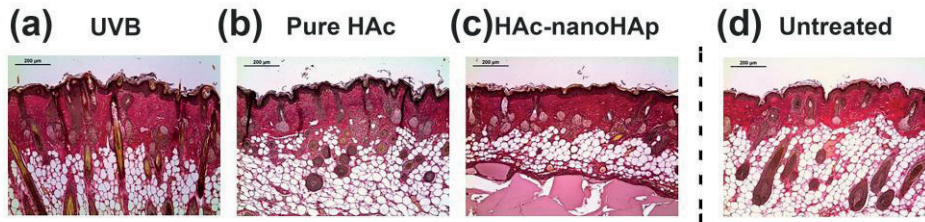


Figure 3.3.9. Collagen fiber formation in the dermis observed from images stained with MT stain (100x): (a) UVB-treated, (b) pure-HAc-filler-treated, (c) HAC–nanoHAp-filler-treated, and (d) untreated skin. (e) Quantification of collagen fiber area from MT stained images (\* P < 0.05).



(e)

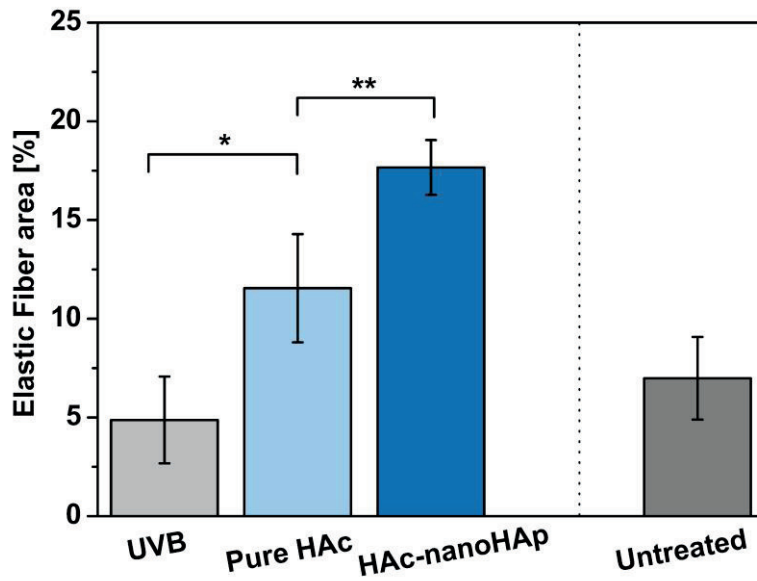
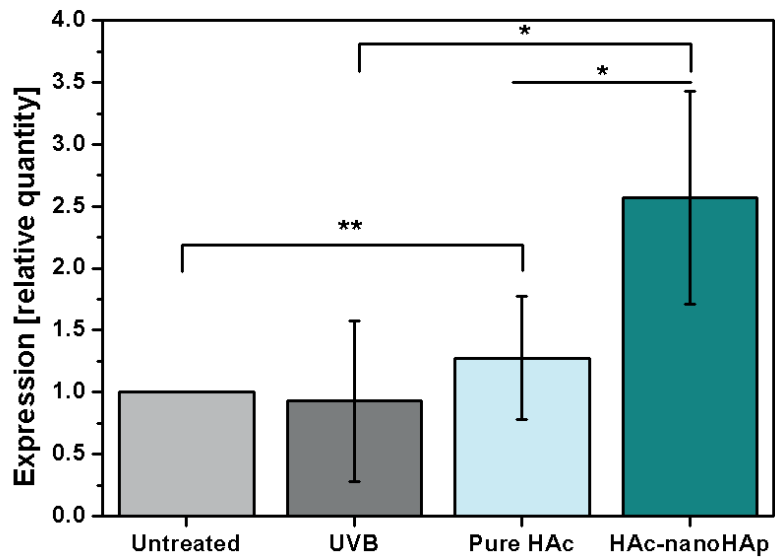


Figure 3.3.10. Elastic fiber formation in the dermis observed from images stained with Verhoeff–Van Gieson (100x): (a) UVB-treated, (b) pure-HAC-filler-treated, (c) HAC–nanoHAp-filler-treated, and (d) untreated skin. (e) Quantification of elastic fiber area (\*  $P < 0.05$ , \*\*  $P < 0.01$ ).



**Figure 3.3.11. Procollagen level of untreated, UVB-treated, pure-HAc-treated, and HAc–nanoHAp-treated skin 4 weeks after injection (\* P < 0.05, \*\* P < 0.01).**

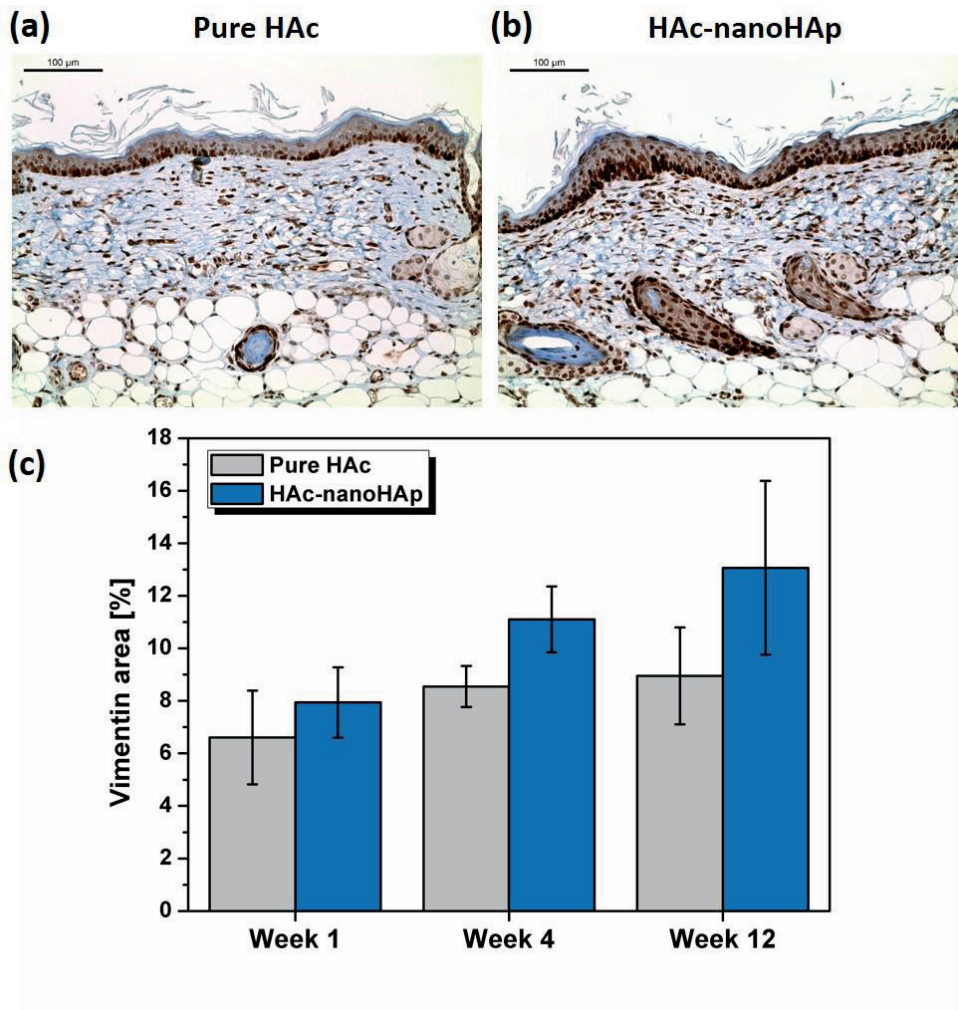
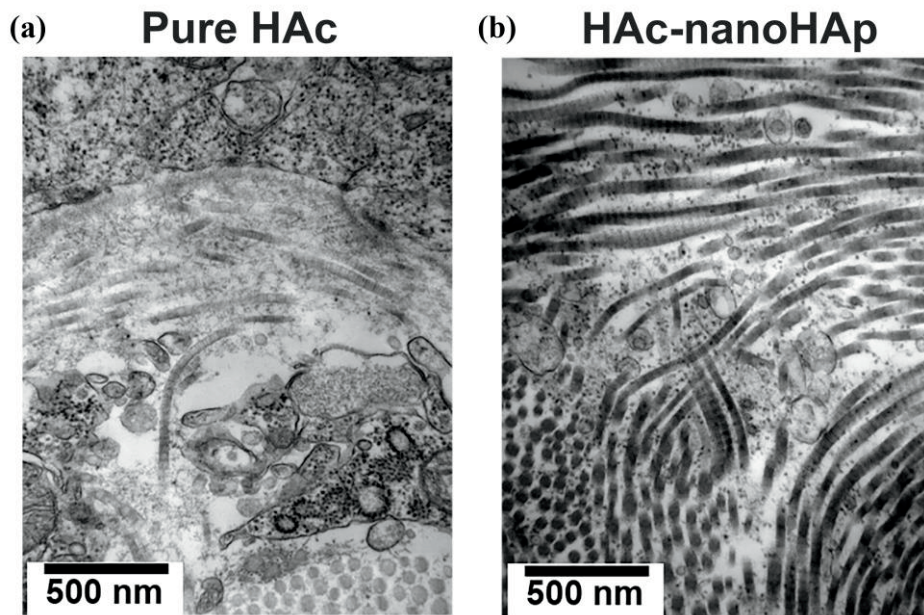


Figure 3.3.12. Observation of vimentin in (a) pure HAC and (b) HAC–nanoHAp by immunostaining (scale bar = 100 μm). (c) Quantitative vimentin area at week 1, 4, and 12.



**Figure 3.3.13. TEM images of dermis after treatment with (a) pure HAc and (b) HAc–nanoHAp showing the higher density of collagen in highly organized forms following HAc–nanoHAp filler injection.**

**Chapter 4.**

**Hyaluronic Acid–Calcium Fluoride**

**Nanocomposite Hydrogels for Advanced**

**Antibacterial Wound Dressings**

## 4.1. Introduction

Wound healing is a global issue that poses various challenges as the aging population increases. Indeed, unfavorable delayed healing conditions, including those associated with diabetes [158], ulcers [159], and persistent infections, result in wound failure accompanied by severe suffering [160]. Therefore, the need for the development of an effective wound dressing to achieve expeditious wound healing has attracted considerable attention.

An ideal wound dressing must prevent infection, allow gaseous exchange, and provide a hydrated environment [161]. Recently, commercial wound dressing materials made of hydrogels have been widely reported because of the presence of hydrophilic polymer chains, which can absorb a large amount of water [162]. Hydrogel dressings can also provide moisture to wounds and properly absorb exudates from the wound. These dressings can be made from either synthetic or natural polymers. Among the various dressings in hydrogel form, HAC has been recognized as exerting a positive effect on the wound healing process because of its excellent biocompatibility, bioactivity, and biodegradability [163, 164]. However, the demand for more advanced platforms for efficient wound therapy and the desire to achieve expeditious wound healing with several functionalities, such as bioadhesivity, bioactivity, or antibacterial activities, has resulted in great progress in the development of advanced wound dressing materials.

One strategy to maximize the therapeutic effects of advanced wound dressings is to incorporate several agents or other materials to the dressings to fabricate composite hydrogel forms [165]. Especially for antibacterial effects, Ag nanoparticles [166] and antibiotic-loaded inorganic carriers such as silica nanoparticles [167] have been immobilized in hydrogels. However, these systems can cause toxicity in a cellular environment because of either the high concentration of particles or fast release of drugs. In our work, CaF<sub>2</sub> nanoparticles were selected for incorporation in a HAc-based hydrogel to design a novel nanocomposite hydrogel system for advanced wound healing. Ca ions are known to greatly affect fibroblast contraction and proliferation, resulting in a decrease of wound size[168]. The effect of F ions on antibacterial activity has also been widely reported [169]. Thus, we expected that a CaF<sub>2</sub>-embedded composite hydrogel would display synergetic effects on wound healing in terms of bioactivity and antibacterial activity. In addition, the sustained release of ions from the composite hydrogels is expected because of the high crystallinity of CaF<sub>2</sub>. Because there have been no reports related to the effect of CaF<sub>2</sub> on the wound healing process, we strongly highlight the potential for developing CaF<sub>2</sub> composite hydrogels via the *in situ* precipitation process described in **Chapter 2**.

## **4.2. Experimental procedures**

### **Fabrication and characterization of HAC–CaF<sub>2</sub> nanocomposite hydrogels**

Before incorporating CaF<sub>2</sub>, the pure HAC hydrogel was fabricated using a mixture of glycidyl methacrylated HAC and poly(ethylene glycol) diacrylate with a M.W. of 700 g/mol using a photo-crosslinking process. The pure hydrogel was then immersed in CaCl<sub>2</sub> solution overnight and subsequently dipped in NH<sub>4</sub>F solution to induce CaF<sub>2</sub> precipitation within the gel. A schematic diagram of this process is presented in **Figure 4.1**. The precipitation time was controlled from 10 min to 1 h. The surface morphologies of the hydrogels were examined using FE-SEM (SUPRA 55VP, Carl Zeiss, Germany), and their compositions were determined using XRD (D8-Advance, Bruker, Germany). The results were compared with those for the pure hydrogel.

### **Ion release behavior**

The ion release behaviors of fluorine ions (F<sup>-</sup>) from the CaF<sub>2</sub> composite hydrogels in PBS solution at 37°C were monitored until 10 days using a fluoride ion electrode (Orion Star A214 fluoride electron, Orion Research Inc., UK) connected to an ion analyzer (901, Orion Research, UK) after dilution with an ionic strength adjustment buffer solution (TISAB).

### ***In vitro* cell tests**

The *in vitro* cellular responses were examined using cell attachment tests and MTS assays using L929 fibroblasts. Fibroblasts at densities of  $1 \times 10^4$  cells/mL were seeded on the hydrogels for the cell attachment. The cells were cultured in  $\alpha$ -MEM (Welgene, Korea) supplemented with 10% FBS and 1% penicillin–streptomycin in a humidified incubator with 5% CO<sub>2</sub> at 37°C for 3 days. After being fixed using 4% paraformaldehyde, the cells on the samples were stained with fluorescent phalloidin, and DAPI for 20 min, and 5 min, respectively. The cells attached on the hydrogels were visualized using CLSM (FluoView FV1000, Olympus, Japan). Then,  $3 \times 10^4$  cells/mL of cells were seeded on the hydrogels for the cell proliferation test. After culturing for 3 and 5 days, the level of cell proliferation was measured using the MTS assay (CellTiter 96 Aqueous One Solution, Promega, USA).

For the *in vitro* cell migration assay, human umbilical vein endothelial cells (HUVECs) were used. In brief, HUVEC cells were seeded on 4-well plates and cultured until a cell monolayer was created. Then, a scratch was created using a pipette tip, and the plates were gently washed with the  $\alpha$ -MEM medium supplemented with FBS to rinse the detached cells. The pure hydrogel and CaF<sub>2</sub> composite hydrogel were placed on each plate and incubated for 24 h. After culturing, images were obtained using a photomicroscope (ZEISS, Axiophot, Germany) after staining with crystal violet for 20 min, and the migration ratio was calculated using the following equation:

$$\text{Migration ratio (\%)} = (M_0 - M_t) / M_0 \times 100\%.$$

Here,  $M_0$  and  $M_t$  represent the initial and healed scratch distance, respectively.

### **Assessment of antibacterial activity of the CaF<sub>2</sub> composite hydrogels**

To confirm the antibacterial activity of the CaF<sub>2</sub> composite hydrogels, both qualitative and quantitative methods were employed using two different bacterial strains, *Escherichia coli* (*E. coli*; ATCC, PTA-573, Rockville, MD, USA) and *Staphylococcus aureus* (*S. aureus*) in Luria–Bertani broth (LB broth; BD Difco™, 244620, USA). A concentration of  $0.5 \times 10^5$  CFU/mL of bacteria was introduced onto the surface of the pure hydrogel and CaF<sub>2</sub> composite hydrogel. The bacterial suspensions inoculated on each sample were incubated at 37°C for 12 h. Bacterial live/dead assays and colony tests were conducted using the qualitative and quantitative method, respectively.

For the live/dead assays, the samples were carefully rinsed with new LB broth. The samples were then stained with SYTO 9 and propidium iodide at a ratio of 1:1 for 15 min. The stained bacteria were examined using CLSM (live: green, dead: red).

For the colony tests, the hydrogels were rinsed with 1 mL of PBS immediately after incubation, and the rinsed samples were transferred into 3 mL of fresh PBS in a 15-mL sterilized tube. The tubes containing bacteria incubated on the samples were then vortexed for 1 min to detach all the bacteria from the surfaces of the samples.

The viable bacteria in the PBS were examined by standard serial dilution and spreading on a LB agar plate. The agar plate was incubated in 37°C for 15 h, and the colony images were obtained using a digital camera.

### ***In vivo* animal tests**

For the *in vivo* animal tests, 13 male 6-week-old Sprague–Dawley rats were used to observe the wound healing efficiency of the CaF<sub>2</sub> composite hydrogels compared with pure HAc hydrogels. This animal experiment was approved by the Institutional Animal Care and Use Committee of GENOSS. Wound closure was observed using full-thickness wounds. The rats were anesthetized via an intraperitoneal injection of zoletil (30 mg/kg) and rumpun (5 mg/kg). After the anesthetic was administered, the dorsum was shaved, sterilized with diluted betadine solution, and draped in a sterile manner. For the full-thickness wound preparation, an 8-mm diameter wound was created using a medical biopsy punch, and hydrogel dressings of identical size were placed on the wounds. Then, each hydrogel dressing was covered with transparent film and compressive dressing bandages for solid fixation. The wound closure was examined at different times and was quantified by measuring the change of the size of the wounds. At each measurement time, the hydrogel dressings were exchanged with new ones. After 7 days and 14 days of treatment, the tissues were harvested and fixed in 10% formalin overnight and embedded in paraffin. After sectioning the

paraffin block in the vertical direction of the skins, histological sections were stained using H&E stain.

### 4.3. Results

A more dense and uniform distribution of nanoparticles was precipitated on the surface of the CaF<sub>2</sub> composite hydrogels compared with the pure hydrogel (**Figure 4.2**). Different CaF<sub>2</sub> nanoparticle morphologies were also observed depending on the precipitation time based on EDS analysis (**Figure 4.3**). With increasing precipitation time, the CaF<sub>2</sub> nanoparticle content increased. In addition, in the XRD patterns of all of the composite hydrogels, typical peaks of CaF<sub>2</sub> ceramics and increased crystallinity with increasing precipitation time were observed (**Figure 4.4**).

The ion-release profiles differed depending on the CaF<sub>2</sub> concentration and precipitation time, as observed in **Figure 4.5**. By controlling the precipitation time, especially for 10 min and after 30 min, a large difference in the ion-release profiles as a function of CaF<sub>2</sub> concentration was observed. A shorter precipitation time resulted in faster release of fluoride, whereas for the 30-min and 1-h samples, sustained ion release was achieved.

Upon incorporating CaF<sub>2</sub> particles in the gel matrix, the water content significantly decreased and the G' values dramatically increased compared with

those of the pure gel (**Figure 4.6**). Because  $\text{CaF}_2$  particles have high crystallinity, changing their content did not affect the stiffness of the hydrogels.

Live/dead assays using both *E. coli* and *S. aureus* were conducted, and the results are presented in **Figure 4.7**. Interestingly, the  $\text{CaF}_2$  composite gel seemed more effective in inhibiting bacterial growth for *S. aureus* than for *E. coli*. *E. coli* is a representative gram-negative bacteria, which possesses additional lipid layer, whereas *S. aureus* is a gram-positive bacteria, which only has an outer layer consisting of proteoglycan. Thus, *E. coli* has a more negatively charged surface than *S. aureus*. The fluorine released from the  $\text{CaF}_2$  composite gel was less effective on the growth *E. coli*, whereas it greatly affected the growth of *S. aureus*. As *S. aureus* is generally found in infected wound regions, the  $\text{CaF}_2$  composite gel could be applied as an effective antibacterial wound healing material. The quantitative data from the bacterial colony tests using *E. coli* and *S. aureus* also matched the live/dead assay results, as observed in **Figure 4.8**. Regardless of the type of bacteria, the number of bacteria on the  $\text{CaF}_2$  composite gel decreased compared with that on the pure gel, demonstrating the role of  $\text{CaF}_2$  in inhibiting bacterial growth.

Interestingly, the  $\text{CaF}_2$  composite gel exhibited excellent bioactivity compared with the pure gel. The fibroblasts were highly stretched and proliferated on the composites compared with on the pure hydrogel (**Figure 4.9**), which can be explained by the effects of Ca ions on cell viability. The fluoride ions greatly affected

the bacteria growth negatively: however, they did not have any effect on cell viability. To elucidate the wound healing efficiency of the CaF<sub>2</sub> composite gel, an *in vitro* cell migration assay was conducted using HUVECs. As observed in **Figure 4.10**, the released ions from the CaF<sub>2</sub> composite gel greatly stimulated cell migration, resulting in faster wound closure than that observed using the pure gel. Among the composites, the samples with the 10-min precipitation time showed higher proliferation.

The *in vivo* animal tests on the full-thickness wound model also showed good agreement with the *in vitro* results, as depicted in **Figure 4.11**. Expectedly, the untreated wound remained in the dry state and a scab was formed over the wound, whereas the wounds treated with the pure gel and CaF<sub>2</sub> composite gel maintained their moisturized environment because of the hydrogel dressing treatments. The differences between these gels can be clearly observed in the wound healing rates, which were calculated based on the changes in the wound size areas. At day 6, the wounds treated with the CaF<sub>2</sub> composite gels dramatically decreased in size down to 40% of their initial sizes, whereas the wounds treated with the pure hydrogel remained at 60% of their initial sizes. Based on the histologically stained images of the wounds after 7 and 14 days of treatment, better wound healing performance was observed for the wound treated with the CaF<sub>2</sub> composite gel than that treated with the pure gel and the untreated wound (**Figure 4.12**). At day 7, large numbers of

fibroblasts were observed on the newly formed dermis sites of the wound regions regardless of the dressing material. However, a larger amount of newly generated epidermis was observed for the wounds treated with the CaF<sub>2</sub> composite gel than for those treated with the pure gel. At day 14, a clear difference was observed between the samples. The untreated wound was also mostly healed; however, inflammatory cells were still present. Compared with the pure gel, the CaF<sub>2</sub> composite gel accelerated re-epithelialization, resulting in a thicker and more mature epidermis. Overall, these results demonstrate the great potential of the CaF<sub>2</sub> composite gel to serve as an advanced composite hydrogel for efficient wound healing applications.

#### **4.4. Discussion**

Because of their water-rich nature, hydrogels not only provide a moist environment to surrounding tissue but can also deliver any hydrophilic drug or agent to assist wound healing. In addition, incorporating bioactive ions to form a composite hydrogel or crosslinking hydrogel networks have also been reported for enhancing wound healing efficiency. However, it is difficult to control the release of ions under physiological conditions in these systems. In our work, we successfully fabricated CaF<sub>2</sub> composite gels through an *in situ* precipitation process that showed sustained release of ions because of the high crystallinity of the particles in the gel. Because of this high crystallinity, the entire composite gel system possesses high stability under

physiological conditions with high robustness. The incorporation of a low concentration of ions (ppm units) sufficiently improved both the antibacterial activity and bioactivity for efficient wound healing.

The main approach of this work involved endowing multifunctionality to the hydrogel to enhance wound healing by inducing ion release from the precipitated particles in the hydrogel, which can play a role in wound-healing stimulation. In particular, fluoride ions are well-known for inhibiting bacterial growth, especially in dental applications. For example, the growth of *Streptococcus mutans*, which is a type of oral bacteria, tends to be inhibited in an environment containing approximately 1.9 ppm fluoride ions [169]. Moreover, fluoride ions are known to bind to bacterial membranes and inhibit the metabolism of bacteria [170]. Indeed, the actions of fluoride ions released from the  $\text{CaF}_2$  composite gel on bacteria led to inhibited growth of both *E. coli* and *S. aureus*. Therefore, it is reasonable to assume that the presence of fluoride in the  $\text{CaF}_2$  composite gel further restricted the growth of bacteria compared with the pure gel. Another feasible explanation for these results is related to the surface charge, as it is known to affect the level of bacterial adhesion [171]. Because the hydrogel itself was mainly composed of HAc, a well-known negatively charged polymer, and fluoride ions were released from the  $\text{CaF}_2$  particles within the gel, the  $\text{CaF}_2$  composite gel surface provided a negative surface charge under physiological conditions. This condition led to lower bacterial adhesion

because of the degree of electrostatic repulsion with the bacteria, eventually resulting in the inhibition of bacterial growth.

Interestingly, the released ions had a positive effect on the cellular behaviors of both L929 and HUVECs. There is a related study showing that fluorapatite (FA) positively supports the proliferation of human gingival fibroblast, which demonstrates the good biocompatibility of FA for soft tissues [172]. We confirmed that  $\text{CaF}_2$  positively contributes to the cell proliferation and *in vitro* migration. We also clearly demonstrated the *in vivo* wound healing efficiency of  $\text{CaF}_2$  composite gel, which appeared to accelerate the migration of fibroblasts and endothelial cells and the formation of granulation tissue. In particular, ions released from the  $\text{CaF}_2$  composite gel stimulate the migration of cells from the peripheral region of wounds and promote cell interactions, resulting in the formation of epidermis and collagen deposition on the dermis.

## **4.5. Conclusion**

$\text{CaF}_2$  composite hydrogels were successfully fabricated through the *in situ* precipitation process. Because of the high crystallinity of the  $\text{CaF}_2$  particles, a high stiffness of the overall system and sustained release profiles of ions were achieved. In particular, the released ions functioned not only as antibacterial agents but also as bioactive stimuli to promote cellular proliferation and migration. In addition, the

CaF<sub>2</sub> composite gel exhibited excellent *in vivo* wound healing capability by attracting cells, stimulating cell migration to wound sites, enhancing the deposition of ECM matrix, and fostering re-epithelialization. The incorporation of CaF<sub>2</sub> in the hydrogels shows great promise for the design of multifunctional hydrogel dressing materials with improved wound healing efficiency.

## Figures

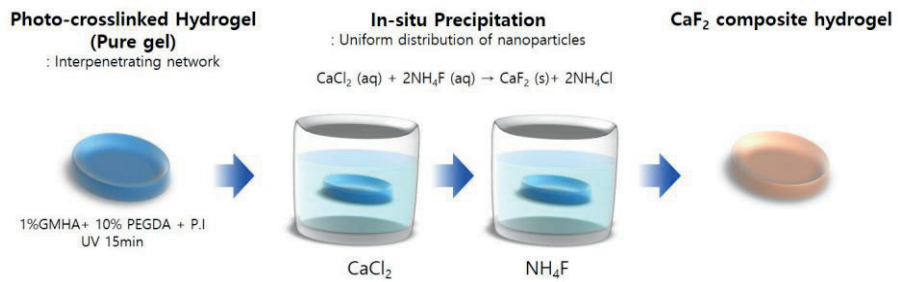


**Figure 4.1. Schematic illustration of fabrication of CaF<sub>2</sub> composite hydrogel via *in situ* precipitation process.**

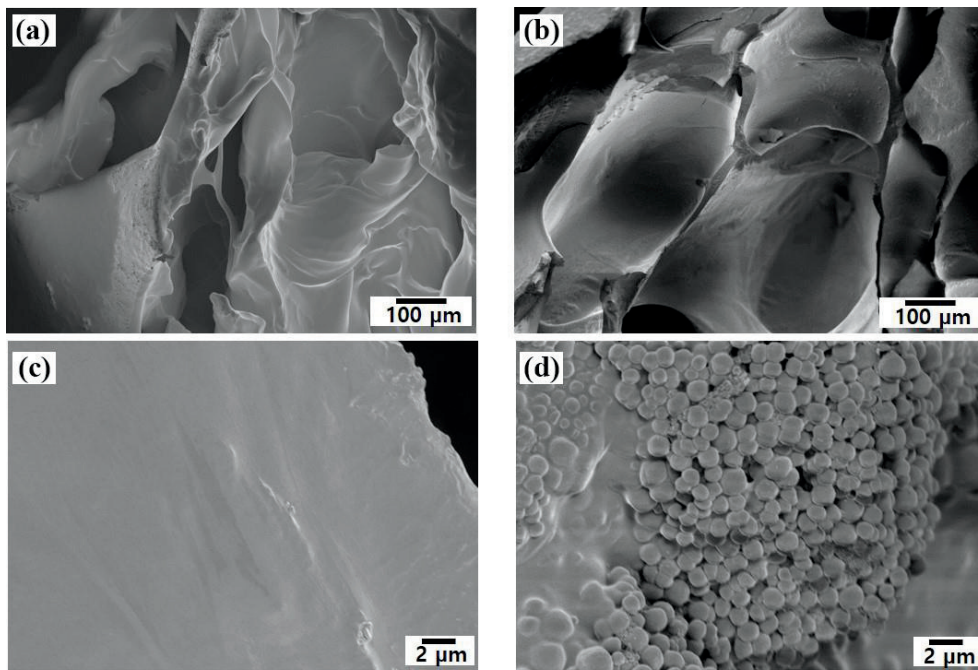


**Figure 4.2.** SEM images of (a) pure gel and (b) CaF<sub>2</sub> composite gel and high-magnified images of (c) pure gel and (d) CaF<sub>2</sub> composite gel.

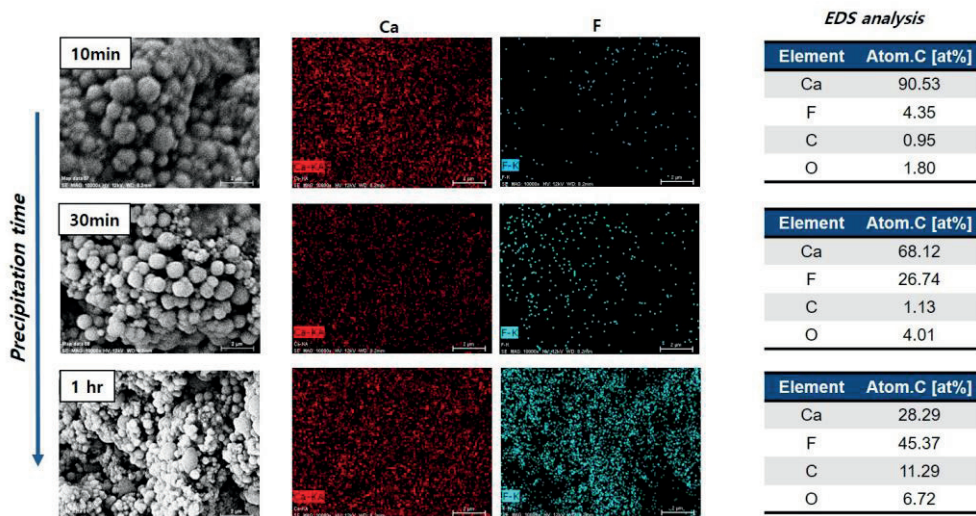
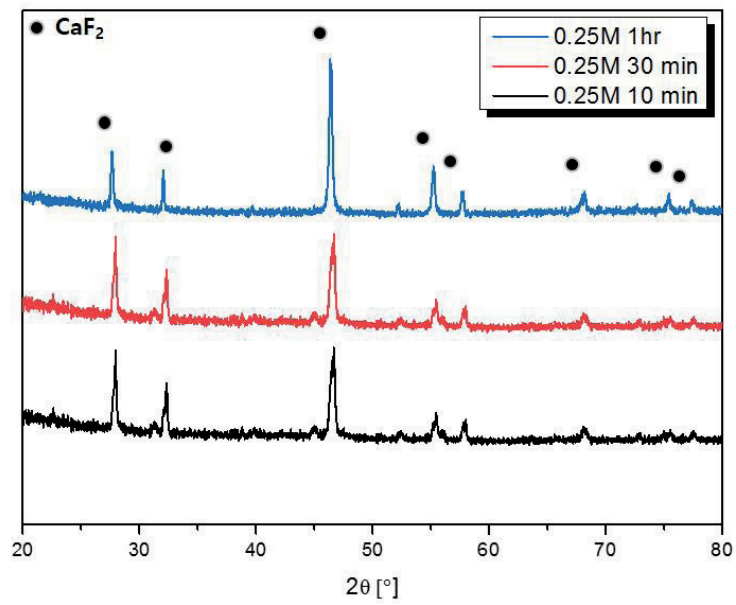


Figure 4.3. EDS mapping images and elemental analysis of  $\text{CaF}_2$  composite gels for precipitation times of 10 min, 30 min, and 1 h.



**Figure 4.4. XRD patterns of  $\text{CaF}_2$  composite gels for precipitation times of 10 min, 30 min, and 1 h.**

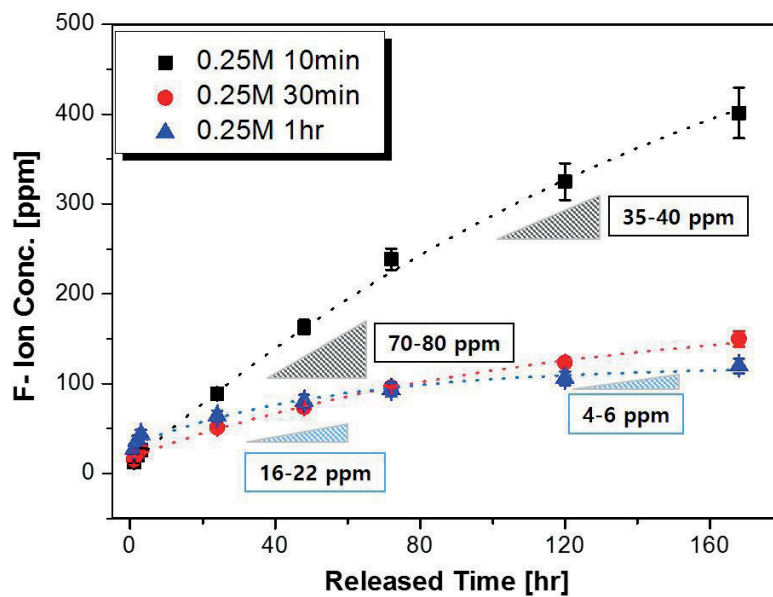


Figure 4.5. Fluoride ion release profiles of  $\text{CaF}_2$  composite gels for precipitation times of 10 min, 30 min, and 1 h.

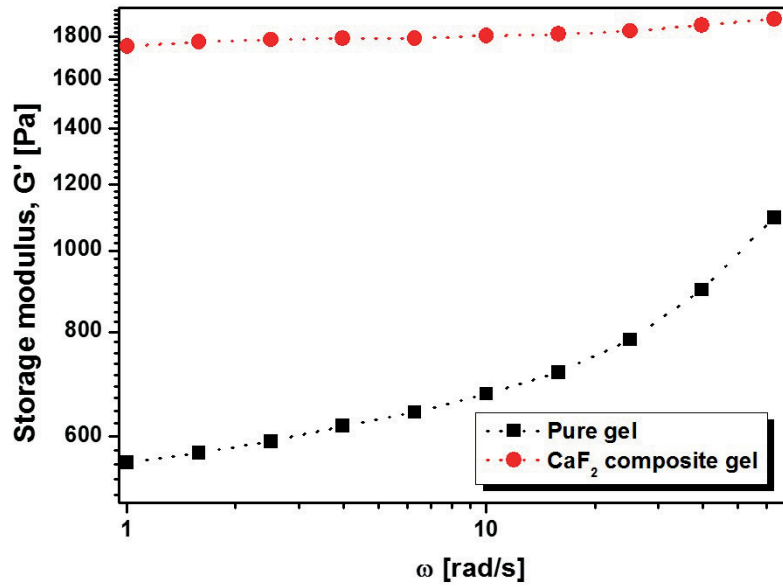


Figure 4.6. Rheological behavior of pure gel and CaF<sub>2</sub> composite gel in frequency sweep mode.

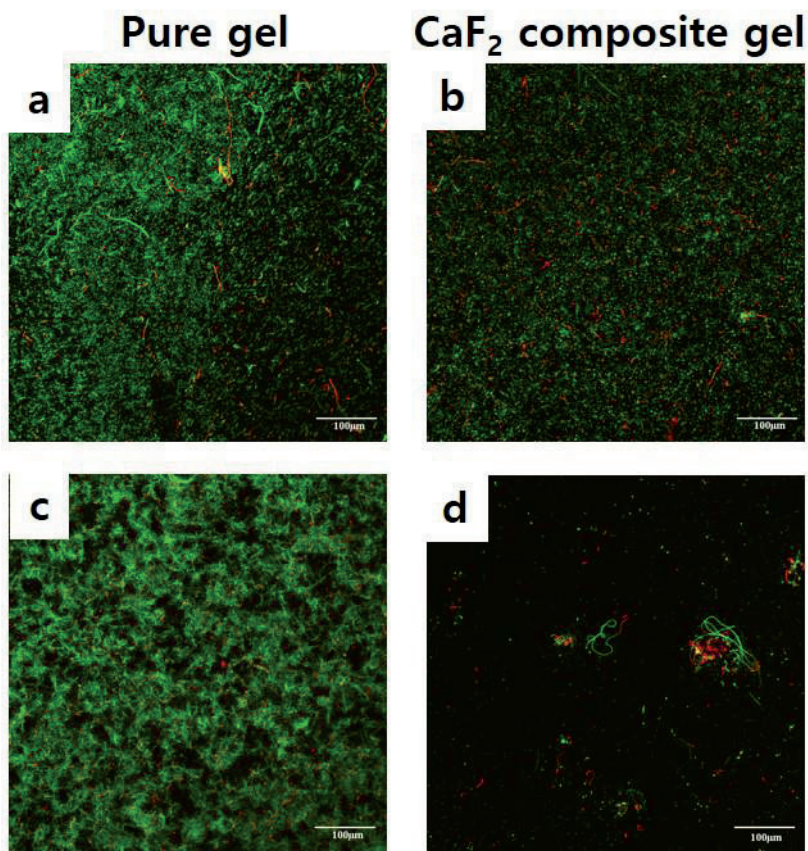
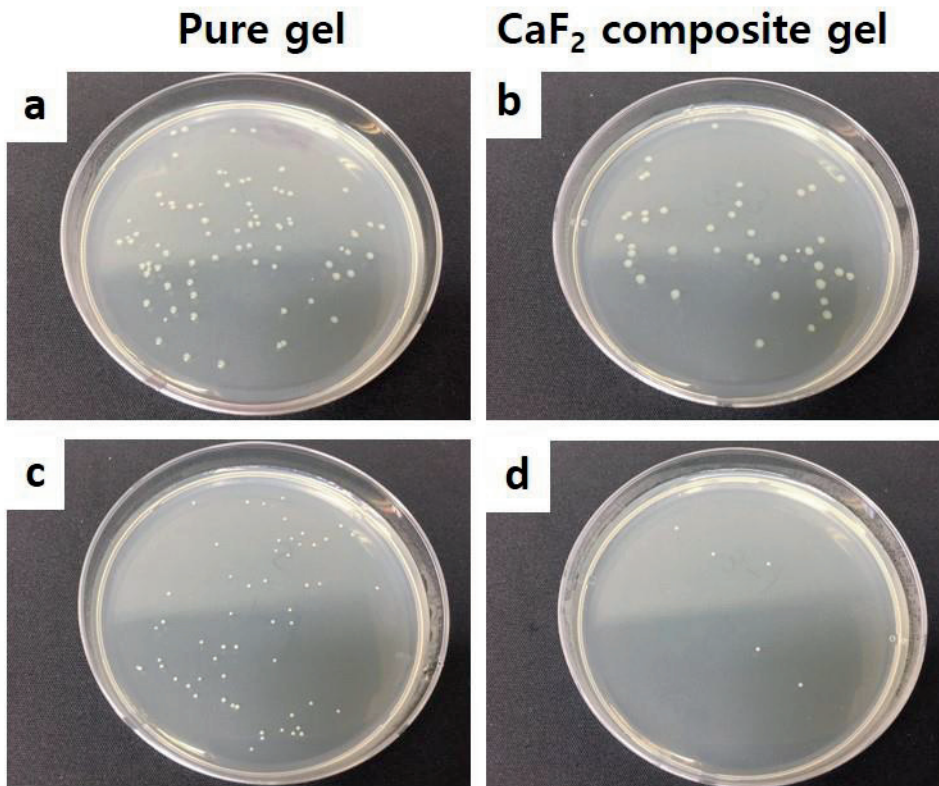


Figure 4.7. Live/dead assay images: Live and dead *E. coli* on the (a) pure gel and (b) CaF<sub>2</sub> composite gel. Live and dead *S. aureus* on the (c) pure gel and (d) CaF<sub>2</sub> composite gel.



**Figure 4.8.** Colonies of *E. coli* on the (a) pure gel and (b) CaF<sub>2</sub> composite gel and colonies of *S. aureus* on the (c) pure gel and (d) CaF<sub>2</sub> composite gel.

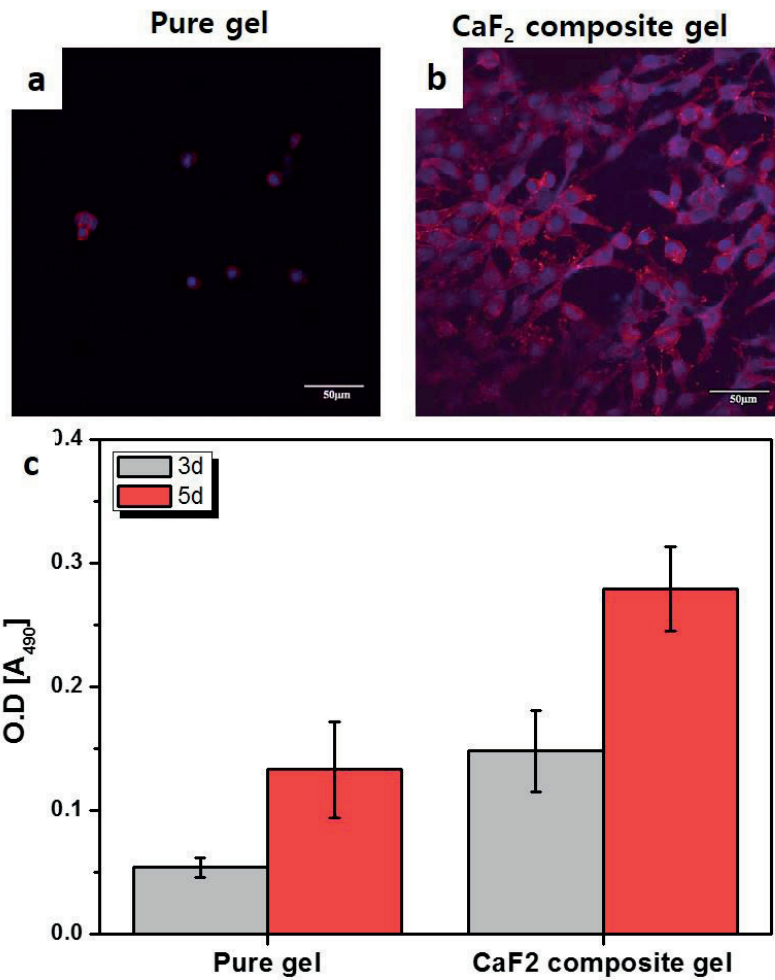


Figure 4.9. (a) CLSM images of L929 fibroblasts cultured on pure gel and CaF<sub>2</sub> composite gel after 2 days. (b) Cell viability of pure gel and CaF<sub>2</sub> composite gel measured by MTS assay after 3 and 5 days.

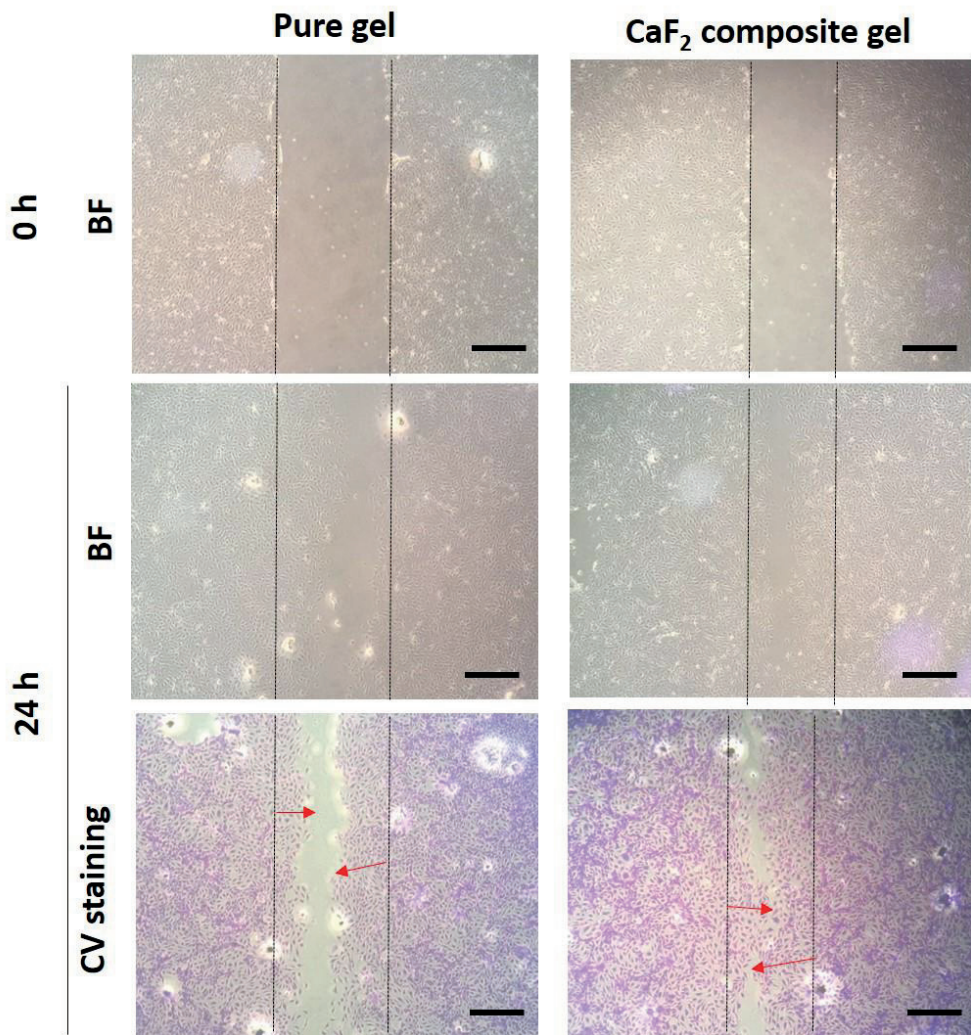
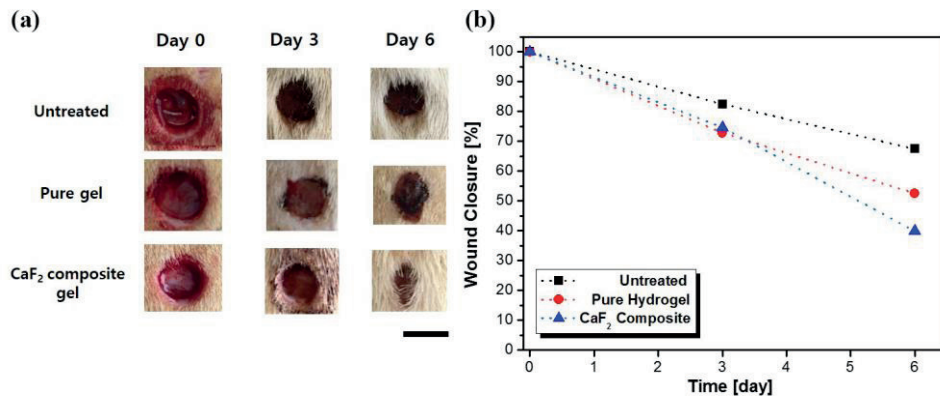
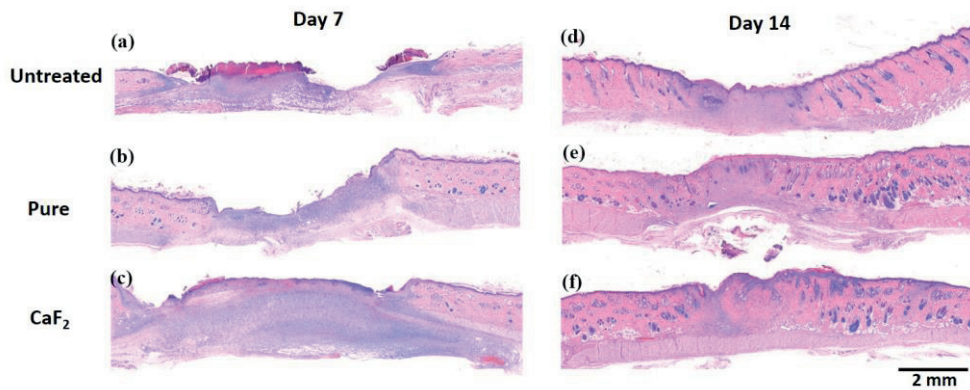


Figure 4.10. *In vitro* HUVEC migration test using pure gel and CaF<sub>2</sub> composite gel.



**Figure 4.11. *In vivo* animal test results: (a) optical images showing wound closure and (b) wound closure over time for untreated wound and wounds treated with pure gel and CaF<sub>2</sub> composite gel up to day 6.**



**Figure 4.12.** H&E stained images for (a) untreated wound and wounds treated with (b) pure hydrogel and (c) CaF<sub>2</sub> composite hydrogel at day 7 and (d) untreated wound and wounds treated with (e) pure hydrogel and (f) CaF<sub>2</sub> composite hydrogel at day 7 day 14.

## **Chapter 5. Conclusion**

## 5.1. Conclusion

In this work, we successfully developed hyaluronic acid (HAc) based nanocomposite hydrogels with biocompatible ceramic nanoparticles through *in situ* precipitation process. Due to high water absorption capacity and anionic nature under physiological condition, HAc hydrogels enabled nano-sized bioceramic particles to be uniformly precipitated within the gel matrix with good structural homogeneity, integrity and minimal aggregation. These structural morphology yielded positive effects on the rheological properties and enzymatic degradation kinetics, compared to the microscopic structure obtained from a physical mixing process. In addition, HAc-CaP nanocomposite hydrogels exhibited enhanced bioactivity compared to pure HAc hydrogels, providing considerable potential for various biomedical applications such as injectable dermal fillers, and hydrogel wound dressings.

Systematic investigation on the effectiveness of the composite fillers on mechanical strength and durability, HAc-nanoHAp fillers exhibited better performances such as long-lasting properties as well as biological response than pure HAc and the composite with micro-sized HAp. In addition, from *in vivo* analysis in a wrinkled skin model, we achieved high lifting capacity of HAc-nanoHAp fillers as well as good biological responses by highly stimulated ECM synthesis in the dermal environment. Accordingly, the HAc-HAp nanocomposite hydrogel fillers are great

options for soft tissue augmentation.

Finally, we also developed an advanced hydrogel wound dressing composed of CaF<sub>2</sub> through *in situ* precipitation process. Precipitated CaF<sub>2</sub> particles enhanced the structural and mechanical stability of the composite hydrogel. In addition, sustained release of fluoride ions from the composite hydrogel mediated excellent both *in vitro* and *in vivo* wound healing capability by attracting cells, stimulating cell migration to wound sites. Moreover, good antibacterial effect was achieved by those released fluoride ions, showing great promise for the design of multifunctional hydrogel dressing materials with improved wound healing efficiency.

## **5.2. Further works**

The scope of the applications of HAC- based nanocomposite hydrogels, via *in situ* precipitation process, can be extended by controlling the composition of precipitated bioceramic particles in the hydrogels. For instance, by increasing CaP content, CaP-rich nanocomposite hydrogels are applicable to injectable bone fillers. In addition, a multiphasic scaffolds based on the nanocomposite hydrogels can be achieved using electric or magnetic fields to induce a concentration gradient of ions. Furthermore, hydrogel coating on a porous foam which can induce the existence of precipitated particles on the surface of the coating layers can be developed for more advanced dressing material.

# Figure

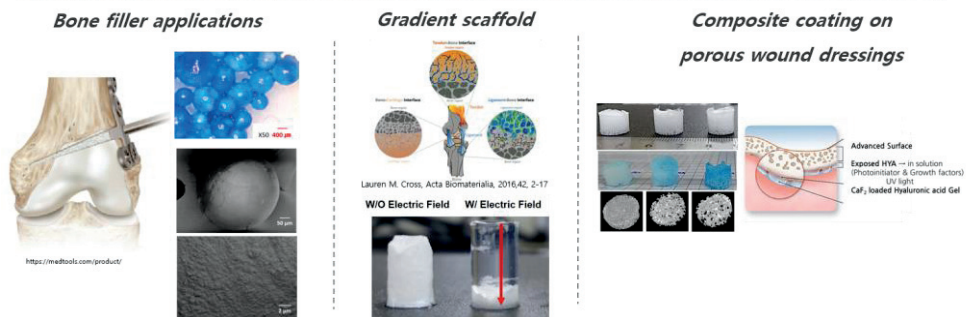


**Figure 5. Various applications of HAc based nanocomposite hydrogels for further works.**

## References

1. Paul, A., et al., *Nanoengineered biomimetic hydrogels for guiding human stem cell osteogenesis in three dimensional microenvironments*. Journal of Materials Chemistry B, 2016. **4**(20): p. 3544-3554.
2. Shapiro, J.M. and M.L. Oyen, *Hydrogel Composite Materials for Tissue Engineering Scaffolds*. Jom, 2013. **65**(4): p. 505-516.
3. Place, E.S., et al., *Synthetic polymer scaffolds for tissue engineering*. Chemical Society Reviews, 2009. **38**(4): p. 1139-1151.
4. Kharkar, P.M., K.L. Kiick, and A.M. Kloxin, *Designing degradable hydrogels for orthogonal control of cell microenvironments*. Chemical Society Reviews, 2013. **42**(17): p. 7335-7372.
5. Hunt, J.A., et al., *Hydrogels for tissue engineering and regenerative medicine*. Journal of Materials Chemistry B, 2014. **2**(33): p. 5319-5338.
6. El-Sherbiny, I.M. and M.H. Yacoub, *Hydrogel scaffolds for tissue engineering: Progress and challenges*. Glob Cardiol Sci Pract, 2013. **2013**(3): p. 316-42.
7. Nichol, J.W., et al., *Cell-laden microengineered gelatin methacrylate hydrogels*. Biomaterials, 2010. **31**(21): p. 5536-5544.
8. Gaharwar, A.K., N.A. Peppas, and A. Khademhosseini, *Nanocomposite hydrogels for biomedical applications*. Biotechnol Bioeng, 2014. **111**(3): p. 441-53.
9. Pasqui, D., et al., *Metal oxide nanoparticles as cross-linkers in polymeric hybrid hydrogels*. Materials Letters, 2011. **65**(2): p. 392-395.
10. Hench, L.L. and J.M. Polak, *Third-generation biomedical materials*. Science, 2002. **295**(5557): p. 1014-7.
11. Merino, S., et al., *Nanocomposite Hydrogels: 3D Polymer-Nanoparticle Synergies for On-Demand Drug Delivery*. ACS Nano, 2015. **9**(5): p. 4686-97.
12. Cha, C., et al., *Carbon-based nanomaterials: multifunctional materials for*

- biomedical engineering*. ACS Nano, 2013. **7**(4): p. 2891-7.
13. da Silva, M.A. and C.A. Dreiss, *Soft nanocomposites: Nanoparticles to tune gel properties*. Polymer International, 2015.
  14. Thoniyot, P., et al., *Nanoparticle-Hydrogel Composites: Concept, Design, and Applications of These Promising, Multi-Functional Materials*. Adv Sci (Weinh), 2015. **2**(1-2): p. 1400010.
  15. Richtering, W. and B.R. Saunders, *Gel architectures and their complexity*. Soft Matter, 2014. **10**(21): p. 3695-3702.
  16. Weissman, J.M., et al., *Thermally Switchable Periodicities and Diffraction from Mesoscopically Ordered Materials*. Science, 1996. **274**(5289): p. 959-60.
  17. Berts, I., et al., *Structure of polymer and particle aggregates in hydrogel composites*. Journal of Polymer Science Part B: Polymer Physics, 2013. **51**(6): p. 421-429.
  18. Amsden, B., *Solute Diffusion within Hydrogels. Mechanisms and Models*. Macromolecules, 1998. **31**(23): p. 8382-8395.
  19. Fraser, J.R., T.C. Laurent, and U.B. Laurent, *Hyaluronan: its nature, distribution, functions and turnover*. J Intern Med, 1997. **242**(1): p. 27-33.
  20. Burdick, J.A. and G.D. Prestwich, *Hyaluronic Acid Hydrogels for Biomedical Applications*. Advanced Materials, 2011. **23**(12): p. H41-H56.
  21. Borzacchiello, A. and L. Ambrosio, *Network formation of low molecular weight hyaluronic acid derivatives*. J Biomater Sci Polym Ed, 2001. **12**(3): p. 307-16.
  22. Xin, X., et al., *Hyaluronic-acid-based semi-interpenetrating materials*. J Biomater Sci Polym Ed, 2004. **15**(9): p. 1223-36.
  23. Bencherif, S.A., et al., *Influence of the degree of methacrylation on hyaluronic acid hydrogels properties*. Biomaterials, 2008. **29**(12): p. 1739-1749.
  24. Hachet, E., et al., *Design of Biomimetic Cell-Interactive Substrates Using Hyaluronic Acid Hydrogels with Tunable Mechanical Properties*.

- Biomacromolecules, 2012. **13**(6): p. 1818-1827.
25. Borzacchiello, A., et al., *Hyaluronic Acid Based Hydrogels for Regenerative Medicine Applications*. Biomed Res Int, 2015. **2015**: p. 871218.
  26. Portnov, T., T.R. Shulimzon, and M. Zilberman, *Injectable hydrogel-based scaffolds for tissue engineering applications*. Reviews in Chemical Engineering, 2017. **33**(1): p. 91-107.
  27. Tan, H.P. and K.G. Marra, *Injectable, Biodegradable Hydrogels for Tissue Engineering Applications*. Materials, 2010. **3**(3): p. 1746-1767.
  28. Yeom, J., et al., *Effect of Cross-Linking Reagents for Hyaluronic Acid Hydrogel Dermal Fillers on Tissue Augmentation and Regeneration*. Bioconjugate Chemistry, 2010. **21**(2): p. 240-247.
  29. Yu, F., et al., *An injectable hyaluronic acid/PEG hydrogel for cartilage tissue engineering formed by integrating enzymatic crosslinking and Diels-Alder "click chemistry"*. Polymer Chemistry, 2014. **5**(3): p. 1082-1090.
  30. Kim, J., et al., *Bone regeneration using hyaluronic acid-based hydrogel with bone morphogenic protein-2 and human mesenchymal stem cells*. Biomaterials, 2007. **28**(10): p. 1830-1837.
  31. Widjaja, L.K., et al., *Hyaluronic acid-based nanocomposite hydrogels for ocular drug delivery applications*. Journal of Biomedical Materials Research Part A, 2014. **102**(9): p. 3056-3065.
  32. Schramm, C., et al., *The Cross-linked Biopolymer Hyaluronic Acid as an Artificial Vitreous Substitute*. Investigative Ophthalmology & Visual Science, 2012. **53**(2): p. 613-621.
  33. Kurisawa, M., et al., *Injectable biodegradable hydrogels composed of hyaluronic acid-tyramine conjugates for drug delivery and tissue engineering*. Chemical Communications, 2005(34): p. 4312-4314.
  34. Xu, X., et al., *Hyaluronic acid-based hydrogels: from a natural polysaccharide to complex networks*. Soft Matter, 2012. **8**(12): p. 3280-3294.
  35. Drury, J.L. and D.J. Mooney, *Hydrogels for tissue engineering: scaffold design variables and applications*. Biomaterials, 2003. **24**(24): p. 4337-4351.

36. Jia, X.Q. and K.L. Kiick, *Hybrid Multicomponent Hydrogels for Tissue Engineering*. *Macromolecular Bioscience*, 2009. **9**(2): p. 140-156.
37. Fakhari, A. and C. Berklund, *Applications and emerging trends of hyaluronic acid in tissue engineering, as a dermal filler and in osteoarthritis treatment*. *Acta Biomater*, 2013. **9**(7): p. 7081-92.
38. Segura, T., et al., *Crosslinked hyaluronic acid hydrogels: a strategy to functionalize and pattern*. *Biomaterials*, 2005. **26**(4): p. 359-371.
39. Pitarresi, G., et al., *Photo-cross-linked hydrogels with polysaccharide-poly(amino acid) structure: New biomaterials for pharmaceutical applications*. *Biomacromolecules*, 2006. **7**(4): p. 1302-1310.
40. Jia, X.Q., et al., *Synthesis and characterization of in situ cross-linkable hyaluronic acid-based hydrogels with potential application for vocal fold regeneration*. *Macromolecules*, 2004. **37**(9): p. 3239-3248.
41. Hahn, S.K., R. Ohri, and C.M. Giachelli, *Anti-calcification of bovine pericardium for bioprosthetic heart valves after surface modification with hyaluronic acid derivatives*. *Biotechnology and Bioprocess Engineering*, 2005. **10**(3): p. 218-224.
42. Dickerson, M.B., K.H. Sandhage, and R.R. Naik, *Protein- and Peptide-Directed Syntheses of Inorganic Materials*. *Chemical Reviews*, 2008. **108**(11): p. 4935-4978.
43. Sohrabi, M., et al., *Development of injectable biocomposites from hyaluronic acid and bioactive glass nano-particles obtained from different sol-gel routes*. *Materials Science & Engineering C-Materials for Biological Applications*, 2013. **33**(7): p. 3730-3744.
44. Pek, Y.S., et al., *The development of a nanocrystalline apatite reinforced crosslinked hyaluronic acid-tyramine composite as an injectable bone cement*. *Biomaterials*, 2009. **30**(5): p. 822-828.
45. Lau, H.K. and K.L. Kiick, *Opportunities for Multicomponent Hybrid Hydrogels in Biomedical Applications*. *Biomacromolecules*, 2015. **16**(1): p. 28-42.

46. Vallés-Lluch, A., et al., *Hyaluronic acid-silica nanohybrid gels*. *Biomacromolecules*, 2013. **14**(12): p. 4217-4225.
47. Nejadnik, M.R., et al., *Self-healing hybrid nanocomposites consisting of bisphosphonated hyaluronan and calcium phosphate nanoparticles*. *Biomaterials*, 2014. **35**(25): p. 6918-29.
48. He, L.H., et al., *In-situ mineralization of chitosan/calcium phosphate composite and the effect of solvent on the structure*. *Frontiers of Materials Science*, 2011. **5**(3): p. 282-292.
49. Wang, L., Y. Li, and C.Z. Li, *In situ processing and properties of nanostructured hydroxyapatite/alginate composite*. *Journal of Nanoparticle Research*, 2009. **11**(3): p. 691-699.
50. Nardecchia, S., et al., *In Situ Precipitation of Amorphous Calcium Phosphate and Ciprofloxacin Crystals during the Formation of Chitosan Hydrogels and Its Application for Drug Delivery Purposes*. *Langmuir*, 2012. **28**(45): p. 15937-15946.
51. Leach, J.B., et al., *Photocrosslinked hyaluronic acid hydrogels: Natural, biodegradable tissue engineering scaffolds*. *Biotechnology and Bioengineering*, 2003. **82**(5): p. 578-589.
52. Hwang, C.M., et al., *Assessments of injectable alginate particle-embedded fibrin hydrogels for soft tissue reconstruction*. *Biomedical Materials*, 2013. **8**(1).
53. Shibayama, M., *Structure-mechanical property relationship of tough hydrogels*. *Soft Matter*, 2012. **8**(31): p. 8030-8038.
54. Lee, S., et al., *Dynamics in Multicomponent Polyelectrolyte Solutions*. *Macromolecules*, 2009. **42**(4): p. 1293-1299.
55. Sarvestani, A.S. and E. Jabbari, *A model for the viscoelastic Behavior of nanofilled hydrogel composites under oscillatory shear loading*. *Polymer Composites*, 2008. **29**(3): p. 326-336.
56. Merabia, S., P. Sotta, and D.R. Long, *Unique Plastic and Recovery Behavior of Nanofilled Elastomers and Thermoplastic Elastomers (Payne and Mullins*

- Effects*). Journal of Polymer Science Part B-Polymer Physics, 2010. **48**(13): p. 1495-1508.
57. Sarvestani, A.S., X.Z. He, and E. Jabbari, *The role of filler-matrix interaction on viscoelastic response of biomimetic nanocomposite hydrogels*. Journal of Nanomaterials, 2008.
  58. Degennes, P.G., *Polymers at an Interface - a Simplified View*. Advances in Colloid and Interface Science, 1987. **27**(3-4): p. 189-209.
  59. Degennes, P.G., *Polymers at an Interface .2. Interaction between 2 Plates Carrying Adsorbed Polymer Layers*. Macromolecules, 1982. **15**(2): p. 492-500.
  60. Collins, M.N. and C. Birkinshaw, *Hyaluronic acid based scaffolds for tissue engineering-A review*. Carbohydrate Polymers, 2013. **92**(2): p. 1262-1279.
  61. De Gennes, P.G., *Scaling Concepts in Polymer Physics*, 1979.
  62. Sun, L.M., et al., *Preparation and Properties of Nanoparticles of Calcium Phosphates With Various Ca/P Ratios*. Journal of Research of the National Institute of Standards and Technology, 2010. **115**(4): p. 243-255.
  63. Carlsson, L., et al., *Nano-hybrid self-crosslinked PDMA/silica hydrogels*. Soft Matter, 2010. **6**(15): p. 3619-3631.
  64. Wang, X.R. and C.G. Robertson, *Strain-induced nonlinearity of filled rubbers*. Physical Review E, 2005. **72**(3).
  65. Wang, M., S. Deb, and W. Bonfield, *Chemically coupled hydroxyapatite-polyethylene composites: processing and characterisation*. Materials Letters, 2000. **44**(2): p. 119-124.
  66. Sarvestani, A.S., X.Z. He, and E. Jabbari, *Effect of osteonectin-derived peptide on the viscoelasticity of hydrogel/apatite nanocomposite scaffolds*. Biopolymers, 2007. **85**(4): p. 370-378.
  67. Oyane, A., et al., *Simple surface modification of poly(epsilon-caprolactone) to induce its apatite-forming ability*. Journal of Biomedical Materials Research Part A, 2005. **75A**(1): p. 138-145.
  68. Oyane, A., et al., *Simple surface modification of poly(epsilon-caprolactone)*

- for apatite deposition from simulated body fluid*. *Biomaterials*, 2005. **26**(15): p. 2407-2413.
69. Goes, J.C., et al., *Apatite coating on anionic and native collagen films by an alternate soaking process*. *Acta Biomaterialia*, 2007. **3**(5): p. 773-778.
70. Li, Q.H., et al., *In vitro synthesis of bioactive hydroxyapatite using sodium hyaluronate as a template*. *Journal of Materials Chemistry*, 2012. **22**(38): p. 20257-20265.
71. Jiao, Y., et al., *A rheological study of biodegradable injectable PEGMC/HA composite scaffolds*. *Soft Matter*, 2012. **8**(5): p. 1499-1507.
72. Murphy, W.L. and D.J. Mooney, *Bioinspired growth of crystalline carbonate apatite on biodegradable polymer substrata*. *Journal of the American Chemical Society*, 2002. **124**(9): p. 1910-1917.
73. Nuttelman, C.R., M.C. Tripodi, and K.S. Anseth, *Synthetic hydrogel niches that promote hMSC viability*. *Matrix Biology*, 2005. **24**(3): p. 208-218.
74. Bongio, M., et al., *Biomimetic modification of synthetic hydrogels by incorporation of adhesive peptides and calcium phosphate nanoparticles: in vitro evaluation of cell behavior*. *Eur Cell Mater*, 2011. **22**: p. 359-76.
75. Engler, A.J., et al., *Matrix elasticity directs stem cell lineage specification*. *Cell*, 2006. **126**(4): p. 677-689.
76. Discher, D.E., P. Janmey, and Y.L. Wang, *Tissue cells feel and respond to the stiffness of their substrate*. *Science*, 2005. **310**(5751): p. 1139-1143.
77. Wang, L.S., et al., *Injectable biodegradable hydrogels with tunable mechanical properties for the stimulation of neurogenic differentiation of human mesenchymal stem cells in 3D culture*. *Biomaterials*, 2010. **31**(6): p. 1148-1157.
78. Largo, R.A., et al., *Long-term biostability and bioactivity of "fibrin linked" VEGF(121) in vitro and in vivo*. *Biomaterials Science*, 2014. **2**(4): p. 581-590.
79. Stosich, M.S., et al., *Bioengineering strategies to generate vascularized soft tissue grafts with sustained shape*. *Methods*, 2009. **47**(2): p. 116-121.

80. Quan, T.H., et al., *Enhancing Structural Support of the Dermal Microenvironment Activates Fibroblasts, Endothelial Cells, and Keratinocytes in Aged Human Skin In Vivo*. *Journal of Investigative Dermatology*, 2013. **133**(3): p. 658-667.
81. Kim, Z.H., et al., *A Composite Dermal Filler Comprising Cross-Linked Hyaluronic Acid and Human Collagen for Tissue Reconstruction*. *Journal of Microbiology and Biotechnology*, 2015. **25**(3): p. 399-406.
82. Gong, J.P., et al., *Double-network hydrogels with extremely high mechanical strength*. *Advanced Materials*, 2003. **15**(14): p. 1155-1158.
83. Gong, J.P., *Why are double network hydrogels therefore tough?* *Soft Matter*, 2010. **6**(12): p. 2583-2590.
84. Nakayama, A., et al., *High mechanical strength double-network hydrogel with bacterial cellulose*. *Advanced Functional Materials*, 2004. **14**(11): p. 1124-1128.
85. Webber, R.E., et al., *Large strain hysteresis and mullins effect of tough double-network hydrogels*. *Macromolecules*, 2007. **40**(8): p. 2919-2927.
86. Stevens, L., et al., *Ionic-covalent entanglement hydrogels from gellan gum, carrageenan and an epoxy-amine*. *Soft Matter*, 2013. **9**(11): p. 3009-3012.
87. Sun, J.Y., et al., *Highly stretchable and tough hydrogels*. *Nature*, 2012. **489**(7414): p. 133-136.
88. Chen, Q., et al., *A robust, one-pot synthesis of highly mechanical and recoverable double network hydrogels using thermoreversible sol-gel polysaccharide*. *Advanced Materials*, 2013. **25**(30): p. 4171-4176.
89. Lin, S., et al., *Design of stiff, tough and stretchy hydrogel composites via nanoscale hybrid crosslinking and macroscale fiber reinforcement*. *Soft Matter*, 2014. **10**(38): p. 7519-7527.
90. Samorezov, J.E., C.M. Morlock, and E. Alsberg, *Dual Ionic and Photo-Crosslinked Alginate Hydrogels for Micropatterned Spatial Control of Material Properties and Cell Behavior*. *Bioconjugate Chemistry*, 2015. **26**(7): p. 1339-1347.

91. Moura, M.J., et al., *In Situ Forming Chitosan Hydrogels Prepared via Ionic/Covalent Co-Cross-Linking*. *Biomacromolecules*, 2011. **12**(9): p. 3275-3284.
92. Jătariu, A.N., et al., *Ionic and covalently cross-linked hydrogels based on gelatin and chitosan*. *Soft Materials*, 2013. **11**(1): p. 45-54.
93. Berger, J., et al., *Structure and interactions in covalently and ionically crosslinked chitosan hydrogels for biomedical applications*. *European Journal of Pharmaceutics and Biopharmaceutics*, 2004. **57**(1): p. 19-34.
94. Shen, X.P., et al., *Hydrogels based on cellulose and chitin: fabrication, properties, and applications*. *Green Chemistry*, 2016. **18**(1): p. 53-75.
95. Bakarich, S.E., et al., *Recovery from applied strain in interpenetrating polymer network hydrogels with ionic and covalent cross-links*. *Soft Matter*, 2012. **8**(39): p. 9985-9988.
96. Yang, C.H., et al., *Strengthening Alginate/Polyacrylamide Hydrogels Using Various Multivalent Cations*. *ACS Applied Materials & Interfaces*, 2013. **5**(21): p. 10418-10422.
97. Naficy, S., et al., *Mechanical properties of interpenetrating polymer network hydrogels based on hybrid ionically and covalently crosslinked networks*. *Journal of Applied Polymer Science*, 2013. **130**(4): p. 2504-2513.
98. Jeong, S.H., et al., *Strong and Biostable Hyaluronic Acid-Calcium Phosphate Nanocomposite Hydrogel via in Situ Precipitation Process*. *Biomacromolecules*, 2016. **17**(3): p. 841-851.
99. Wong, C.T., et al., *In vivo cancellous bone remodeling on a Strontium-containing hydroxyapatite (Sr-HA) bioactive cement*. *Journal of Biomedical Materials Research - Part A*, 2004. **68**(3): p. 513-521.
100. Mi, F.L., et al., *Chitosan-polyelectrolyte complexation for the preparation of gel beads and controlled release of anticancer drug. II. Effect of pH-dependent ionic crosslinking or interpolymer complex using tripolyphosphate or polyphosphate as reagent*. *Journal of Applied Polymer Science*, 1999. **74**(5): p. 1093-1107.

101. Shu, X.Z., K.J. Zhu, and W.H. Song, *Novel pH-sensitive citrate cross-linked chitosan film for drug controlled release*. International Journal of Pharmaceutics, 2001. **212**(1): p. 19-28.
102. Jha, A.K., W.M. Jackson, and K.E. Healy, *Controlling Osteogenic Stem Cell Differentiation via Soft Bioinspired Hydrogels*. Plos One, 2014. **9**(6).
103. Trappmann, B. and C.S. Chen, *How cells sense extracellular matrix stiffness: a material's perspective*. Current Opinion in Biotechnology, 2013. **24**(5): p. 948-953.
104. Watt, F.M. and W.T.S. Huck, *Role of the extracellular matrix in regulating stem cell fate*. Nature Reviews Molecular Cell Biology, 2013. **14**(8): p. 467-473.
105. Park, J.W., Y.J. Kim, and J. Jang, *Enhanced osteoblast response to hydrophilic strontium and/or phosphate ions-incorporated titanium oxide surfaces*. Clinical Oral Implants Research, 2010. **21**(4): p. 398-408.
106. Liu, Y.T., et al., *Engineering three-dimensional structures using bio-inspired dopamine and strontium on titanium for biomedical application*. Journal of Materials Chemistry B, 2014. **2**(45): p. 7927-7935.
107. Silva-Correia, J., et al., *Biocompatibility Evaluation of Ionic- and Photo-Crosslinked Methacrylated Gellan Gum Hydrogels: In Vitro and In Vivo Study*. Advanced Healthcare Materials, 2013. **2**(4): p. 568-575.
108. Machida-Sano, I., et al., *Surface characteristics determining the cell compatibility of ionically cross-linked alginate gels*. Biomedical Materials (Bristol), 2014. **9**(2).
109. Shoichet, M.S., et al., *Stability of hydrogels used in cell encapsulation: An in vitro comparison of alginate and agarose*. Biotechnology and Bioengineering, 1996. **50**(4): p. 374-381.
110. Varma, D.M., et al., *Injectable carboxymethylcellulose hydrogels for soft tissue filler applications*. Acta Biomaterialia, 2014. **10**(12): p. 4996-5004.
111. Iannitti, T., et al., *Experimental and Clinical Efficacy of Two Hyaluronic Acid-based Compounds of Different Cross-Linkage and Composition in the*

- Rejuvenation of the Skin*. Pharmaceutical Research, 2014.
112. Paliwal, S., et al., *Skin Extracellular Matrix Stimulation following Injection of a Hyaluronic Acid-Based Dermal Filler in a Rat Model*. Plastic and Reconstructive Surgery, 2014. **134**(6): p. 1224-1233.
  113. Loghem, J.V., Y.A. Yutskovskaya, and W. Philip Werschler, *Calcium hydroxylapatite: over a decade of clinical experience*. J Clin Aesthet Dermatol, 2015. **8**(1): p. 38-49.
  114. Jones, D., A. Tezel, and M. Borrell, *In vitro resistance to degradation of hyaluronic acid dermal fillers by ovine testicular hyaluronidase*. Dermatologic Surgery, 2010. **36**(SUPPL. 1): p. 804-809.
  115. Buck Ii, D.W., M. Alam, and J.Y.S. Kim, *Injectable fillers for facial rejuvenation: a review*. Journal of Plastic, Reconstructive and Aesthetic Surgery, 2009. **62**(1): p. 11-18.
  116. Chen, J.H., J.T. Chen, and Z. Xu, *Rheological and Biological Characteristics of Hyaluronic Acid Derivative Modified by Polyethylene Glycol*. Journal of Wuhan University of Technology-Materials Science Edition, 2008. **23**(5): p. 617-621.
  117. Park, S., et al., *Investigation of the Degradation-Retarding Effect Caused by the Low Swelling Capacity of a Novel Hyaluronic Acid Filler Developed by Solid-Phase Crosslinking Technology*. Annals of Dermatology, 2014. **26**(3): p. 357-362.
  118. Glogau, R.G., *Fillers: from the past to the future*. Semin Cutan Med Surg, 2012. **31**(2): p. 78-87.
  119. Cockerham, K. and V.J. Hsu, *Collagen-based dermal fillers: past, present, future*. Facial Plast Surg, 2009. **25**(2): p. 106-13.
  120. Burgess, C.M. and R.M. Quiroga, *Assessment of the safety and efficacy of poly L-lactic acid for the treatment of HIV-associated facial lipoatrophy*. J Am Acad Dermatol, 2005. **52**(2): p. 233-9.
  121. Graivier, M.H., et al., *Calcium hydroxylapatite (Radiesse) for correction of the mid- and lower face: Consensus recommendations*. Plastic and

- Reconstructive Surgery, 2007. **120**(6): p. 55s-66s.
122. Beasley, K.L., M.A. Weiss, and R.A. Weiss, *Hyaluronic Acid Fillers: A Comprehensive Review*. Facial Plastic Surgery, 2009. **25**(2): p. 86-94.
  123. Falcone, S.J. and R.A. Berg, *Crosslinked hyaluronic acid dermal fillers: A comparison of rheological properties*. Journal of Biomedical Materials Research - Part A, 2008. **87**(1): p. 264-271.
  124. Leach, J.B., et al., *Photocrosslinked hyaluronic acid hydrogels: Natural, biodegradable tissue engineering scaffolds*. Biotechnology and Bioengineering, 2003. **82**(5): p. 578-589.
  125. Duranti, F., et al., *Injectable hyaluronic acid gel for soft tissue augmentation: A clinical and histological study*. Dermatologic Surgery, 1998. **24**(12): p. 1317-1325.
  126. Fakhari, A. and C. Berklund, *Applications and emerging trends of hyaluronic acid in tissue engineering, as a dermal filler and in osteoarthritis treatment*. Acta Biomaterialia, 2013. **9**(7): p. 7081-7092.
  127. La Gatta, A., et al., *Comparative analysis of commercial dermal fillers based on crosslinked hyaluronan: Physical characterization and in vitro enzymatic degradation*. Polymer Degradation and Stability, 2011. **96**(4): p. 630-636.
  128. Borrell, M., D.B. Leslie, and A. Tezel, *Lift capabilities of hyaluronic acid fillers*. Journal of Cosmetic and Laser Therapy, 2011. **13**(1): p. 21-27.
  129. Tezel, A. and G.H. Fredrickson, *The science of hyaluronic acid dermal fillers*. Journal of Cosmetic and Laser Therapy, 2008. **10**(1): p. 35-42.
  130. Tezel, A. and G.H. Fredrickson, *The Science of Hyaluronic Acid Dermal Fillers (vol 10, pg 35, 2008)*. Journal of Cosmetic and Laser Therapy, 2014. **16**(1): p. 45-45.
  131. Kodavaty, J. and A.P. Deshpande, *Mechanical and Swelling Properties of Poly (vinyl alcohol) and Hyaluronic Acid Gels used in Biomaterial Systems - a Comparative Study*. Defence Science Journal, 2014. **64**(3): p. 222-229.
  132. Peng, Z.Y., et al., *Preparation and Properties of Polyvinyl Alcohol/Collagen Hydrogel*. Journal of Macromolecular Science Part B-Physics, 2012. **51**(10):

- p. 1934-1941.
133. Parenteau-Bareil, R., R. Gauvin, and F. Berthod, *Collagen-Based Biomaterials for Tissue Engineering Applications*. Materials, 2010. **3**(3): p. 1863-1887.
  134. Davidenko, N., et al., *Collagen-hyaluronic acid scaffolds for adipose tissue engineering*. Acta Biomaterialia, 2010. **6**(10): p. 3957-3968.
  135. Tang, S.Q. and M. Spector, *Incorporation of hyaluronic acid into collagen scaffolds for the control of chondrocyte-mediated contraction and chondrogenesis*. Biomedical Materials, 2007. **2**(3): p. S135-S141.
  136. Park, S.N., et al., *Biological characterization of EDC-crosslinked collagen-hyaluronic acid matrix in dermal tissue restoration*. Biomaterials, 2003. **24**(9): p. 1631-1641.
  137. Leonardis, M., et al., *Use of cross-linked carboxymethyl cellulose for soft-tissue augmentation: preliminary clinical studies*. Clinical Interventions in Aging, 2010. **5**: p. 317-322.
  138. Gao, G.R., et al., *Synergistic toughening of nanocomposite double network hydrogels by physical adsorption and chemical bonding of polymer chains to inorganic nanospheres and nanorods: a comparative study*. Rsc Advances, 2016. **6**(44): p. 37974-37981.
  139. Seol-Ha Jeong, Y.-F.F., Jae-Uk Baek, Juha Song, Tae-Hyun Choi, Suk-Wha Kim and Hyoun-Ee Kim, *Long-lasting and bioactive hyaluronic acid-hydroxyapatite composite hydrogels for injectable dermal fillers*. Journal of Biomaterials Applications, 2016.
  140. Juhasz, J.A., S.M. Best, and W. Bonfield, *Preparation of novel bioactive nano-calcium phosphate-hydrogel composites*. Science and Technology of Advanced Materials, 2010. **11**(1).
  141. Seol-Ha Jeong, Y.-H.K., Suk-Wha Kim, Ji-Ung Park, Hyoun-Ee Kim, Ju-Ha Song, *Strong and Biostable Hyaluronic acid-Calcium Phosphate Nanocomposite Hydrogel via in Situ Precipitation Process*. Biomacromolecules, 2016.

142. Santoro, S., et al., *Rheological properties of cross-linked hyaluronic acid dermal fillers*. Journal of Applied Biomaterials & Biomechanics, 2011. **9**(2): p. 127-136.
143. Yan, X.M., et al., *Improved synthesis of hyaluronic acid hydrogel and its effect on tissue augmentation*. Journal of Biomaterials Applications, 2012. **27**(2): p. 179-186.
144. Edsman, K., et al., *Gel Properties of Hyaluronic Acid Dermal Fillers*. Dermatologic Surgery, 2012. **38**(7): p. 1170-1179.
145. Dorsey, S.M., et al., *MRI evaluation of injectable hyaluronic acid-based hydrogel therapy to limit ventricular remodeling after myocardial infarction*. Biomaterials, 2015. **69**: p. 65-75.
146. Hillel, A.T., et al., *Validation of a Small Animal Model for Soft Tissue Filler Characterization*. Dermatologic Surgery, 2012. **38**(3): p. 471-478.
147. Gensanne, D., et al., *In vivo visualization of hyaluronic acid injection by high spatial resolution T2 parametric magnetic resonance images*. Skin Research and Technology, 2007. **13**(4): p. 385-389.
148. Burdick, J.A., et al., *Controlled degradation and mechanical behavior of photopolymerized hyaluronic acid networks*. Biomacromolecules, 2005. **6**(1): p. 386-391.
149. Jansen, D.A. and M.H. Graivier, *Evaluation of a calcium hydroxylapatite-based implant (Radiesse) for facial soft-tissue augmentation*. Plast Reconstr Surg, 2006. **118**(3 Suppl): p. 22S-30S, discussion 31S-33S.
150. Turlier, V., et al., *Association between collagen production and mechanical stretching in dermal extracellular matrix: In vivo effect of cross-linked hyaluronic acid filler. A randomised, placebo-controlled study*. Journal of Dermatological Science, 2013. **69**(3): p. 187-194.
151. Wang, F., et al., *In vivo stimulation of de novo collagen production caused by cross-linked hyaluronic acid dermal filler injections in photodamaged human skin*. Archives of Dermatology, 2007. **143**(2): p. 155-163.
152. Quan, T.H., et al., *Solar ultraviolet irradiation reduces collagen in*

- photoaged human skin by blocking transforming growth factor-beta type II receptor/Smad signaling. American Journal of Pathology, 2004. 165(3): p. 741-751.*
153. Son, E.D., et al., *Topical application of 17 beta-estradiol increases extracellular matrix protein synthesis by stimulating TGF-beta signaling in aged human skin in vivo. Journal of Investigative Dermatology, 2005. 124(6): p. 1149-1161.*
154. Fan, Y., et al., *An Experimental Model Design for Photoaging. J Craniofac Surg, 2015. 26(6): p. e467-71.*
155. Gensanne, D., et al., *In vivo visualization of hyaluronic acid injection by high spatial resolution T-2 parametric magnetic resonance images. Skin Research and Technology, 2007. 13(4): p. 385-389.*
156. Kamman, R.L., et al., *Multi-exponential relaxation analysis with MR imaging and NMR spectroscopy using fat-water systems. Magnetic Resonance Imaging, 1987. 5(5): p. 381-392.*
157. Krutmann, J., *Skin Aging/Anti-Aging Strategies. Hautarzt, 2011. 62(8): p. 576-576.*
158. Xiao, Y., et al., *Diabetic wound regeneration using peptide-modified hydrogels to target re-epithelialization. Proceedings of the National Academy of Sciences of the United States of America, 2016. 113(40): p. E5792-E5801.*
159. Lyder, C.H., *Pressure ulcer prevention and management. Jama-Journal of the American Medical Association, 2003. 289(2): p. 223-226.*
160. Boateng, J. and O. Catanzano, *Advanced Therapeutic Dressings for Effective Wound Healing--A Review. J Pharm Sci, 2015. 104(11): p. 3653-80.*
161. Singer, A.J. and S.A. McClain, *Development of a porcine excisional wound model. Academic Emergency Medicine, 2003. 10(10): p. 1029-1033.*
162. Chen, S., et al., *Mesenchymal stem cell-laden anti-inflammatory hydrogel enhances diabetic wound healing. Scientific Reports, 2015. 5.*
163. Anderson, I., *The properties of hyaluronan and its role in wound healing.*

- Prof Nurse, 2001. **17**(4): p. 232-5.
164. Frenkel, J.S., *The role of hyaluronan in wound healing*. Int Wound J, 2014. **11**(2): p. 159-63.
165. Boateng, J.S., et al., *Wound healing dressings and drug delivery systems: a review*. J Pharm Sci, 2008. **97**(8): p. 2892-923.
166. Alvarez, G.S., et al., *Antibiotic-loaded silica nanoparticle-collagen composite hydrogels with prolonged antimicrobial activity for wound infection prevention*. Journal of Materials Chemistry B, 2014. **2**(29): p. 4660-4670.
167. Fan, Z.J., et al., *A Novel Wound Dressing Based on Ag/Graphene Polymer Hydrogel: Effectively Kill Bacteria and Accelerate Wound Healing*. Advanced Functional Materials, 2014. **24**(25): p. 3933-3943.
168. Kawai, K., et al., *Calcium-based nanoparticles accelerate skin wound healing*. PLoS One, 2011. **6**(11): p. e27106.
169. Marquis, R.E., *Antimicrobial actions of fluoride for oral bacteria*. Can J Microbiol, 1995. **41**(11): p. 955-64.
170. Guha-Chowdhury, N., A.G. Clark, and C.H. Sissons, *Inhibition of purified enolases from oral bacteria by fluoride*. Oral Microbiol Immunol, 1997. **12**(2): p. 91-7.
171. Wilson, W.W., et al., *Status of methods for assessing bacterial cell surface charge properties based on zeta potential measurements*. J Microbiol Methods, 2001. **43**(3): p. 153-64.
172. Alhilou, A., et al., *Physicochemical and Antibacterial Characterization of a Novel Fluorapatite Coating*. ACS Omega, 2016. **1**(2): p. 264-276.

## 초 록

조직공학에서는 생체 내 조직과 환경이 유사한 입체 구조의 하이드로젤이 각광받고 있는데 그 중에서도 높은 강도, 여러 자극 감응형, 약물 및 생체인자 전달 등 다양한 기능성을 부여하기 위하여 하이드로젤에 고분자 뿐 아니라 금속 혹은 세라믹 입자를 혼합하여 복합 하이드로젤을 만드는 연구가 많이 진행되고 있다. 나노 크기의 금속 혹은 세라믹입자로 이루어져 있는 복합 하이드로젤의 경우, 대표적인 제작방법으로는 가교시키기 전의 고분자 혹은 단량체 용액에 입자들을 물리적으로 교반하는 방법이 있다. 하지만, 나노 크기의 입자를 용액 내에 고르게 분산시키는 것이 어려울 뿐 아니라, 입자들끼리 뭉치는 양상을 보이기도 한다. 뿐만 아니라 이러한 입자들이 젤화가 이루어지는 동안 가라앉아 균일한 구조를 제작하는데 어려움이 있다. 이를 해결하기 위해서, 입자들의 표면처리나 젤의 구성성분이 될 고분자의 화학적 처리 등 추가적인 반응이 필요하다. 이를 해결하기 위하여, 기본적으로 높은 팽윤 특성을 지니고 있는 하이드로젤의 기본특성을 이용하여 복합 하이드로젤을 제작하였다. 하이드로젤 내부에 이온을 확산시킨 후, pH 변화 등으로 인한 석출과정을 거쳐 젤 내부에 입자들을 고르게 석출시켜 복합 하이드로젤을 제작하였다.

본 논문은 생체적합성이 우수한 히알루론산 하이드로젤 내부에 대표적인 생체세라믹에 해당하는 인산칼슘을 나노사이즈로 석출시켜 기존 복합 하이드로젤보다 기계적 물성 및 분해저항성, 그리고 생체활성 등을 향상시키는 연구에 대해 다루었다.

인산칼슘의 전구체에 해당하는 염화칼슘과 인산용액에 히알루론산 하이드로젤을 담가 이온들이 내부로 확산되게 한 후, 수산화암모늄으로 인산칼슘을 석출시켰다. 이러한 석출법을 통하여 얻은 복합 하이드로젤의 미세구조 및 조성, 인산칼슘의 크기 및 조성, 분포도 등을 구체적으로 분석하였다. 전구체 용액의 농도를 조절함으로써 석출되는 인산칼슘의 조성을 다양하게 조절할 수 있었고, 이로 인해 복합 하이드로젤의 습윤능력, 유연학적 물성, 효소에 의한 분해 정도 등 다양한 물성 또한 조절이 가능한 것으로 보였다. 또한, 기존 교반 방법으로 만든 복합 하이드로젤보다 우수한 유연학적 물성을 띠는 양상에 대하여, 기존에 알려져 있는 젤의 구조와 물성 간의 관계에 대한 모델을 이용하여 히알루론산 고분자 부분과 인산칼슘 나노입자의 상호작용의 차이를 도출하였다. 그리고 석출법을 통한 복합 하이드로젤의 우수한 생체저항성을 히알루로나아제 효소 용액 내 및 동물실험을 통하여 평가한 결과, 순수 히알루론산 하이드로젤에 비해 저항속도가 현저하게 낮아졌음을 확인하였다.

기존 방법으로 제작한 복합 하이드로젤에 비해서도 우수한 생체저항성을 나타내었다. 마지막으로 섬유아세포의 부착정도 및 증식평가, 그리고 동물실험을 통하여 인산칼슘 혼합으로 인하여 복합 하이드로젤의 생체활성이 향상되었음을 확인하였다.

우수한 기계적 물성 및 생체활성을 나타내는 복합 하이드로젤을 주입형 필러 및 하이드로젤 창상재료로의 응용가능성을 평가하였다. 우선, 주입형 필러로 적용하기 위하여 위에서 연구한 복합 하이드로젤을 분쇄하였는데, 이 과정에서 균일한 인산칼슘 나노입자가 히알루론산 하이드로젤 표면에 고르게 분산된 구조적 형태가 유지됨을 확인하였다. 분쇄된 젤 형태를 앞서 분석한 대로 특성평가 및 유변학적 물성을 평가하였다. 더 나아가 나노 입자 형태의 인산칼슘을 포함한 이 복합 하이드로젤이 마이크로입자의 인산칼슘이 교반된 형태의 복합 하이드로젤보다 다양한 면에서 우수성을 나타내었다. 나노 복합체가 마이크로 복합체보다 유변학적으로 더 단단한 거동을 보였고 이로 인하여 쥐 피부에 주입하여 볼륨 유지능을 평가한 결과, 나노 복합체가 마이크로 복합체보다 더 오랜 기간동안 큰 부피로 유지하는 것을 확인하였다. 뿐만 아니라, 나노 복합체가 마이크로 복합체보다 균일도가 뛰어나 생체활성 면에서도 훨씬 향상된 양상을 보였다. 이 나노 복합체 필러가 실제 주름개선에도

효과가 있는지 평가하기 위하여, 광노화 과정을 통하여 생긴 쥐 주름 부위에 필러를 주입하여 주름개선효과 및 피부조직 재생 정도 등을 심도있게 분석하였다. 순수 히알루론산 필러보다 훨씬 우수한 주름개선효과를 보였는데, 이는 앞서 보였던 나노 복합체 필러의 향상된 기계적 물성뿐 아니라, 체내 세포 및 조직 재생을 돕는 인산칼슘의 영향으로 인한 결과라는 점을 확인할 수 있었다.

마지막으로, 우수한 상처치유능과 항균효과를 가진 복합 하이드로젤 재료를 제작하기 위하여, 위에서 연구한 석출법을 이용하여 인산칼슘 이외에 플루오린화 칼슘을 하이드로젤 내부에 석출시켰다. pH 변화 없이 빠른 속도로 플루오린화 칼슘입자를 석출이 가능하였고, 석출된 입자들의 결정성이 높아 복합 하이드로젤을 생리학적 용액에 담갔을 때 ppm 단위 수준의 플루오린 이온을 방출시킬 수 있었다. 석출시간을 조절하여 이온 방출거동 또한 조절이 가능하였다. 방출된 플루오린 이온은 세포독성에 영향을 거의 미치지 않고, 오히려 우수한 생체활성을 띠었다. 섬유아세포의 부착정도 및 증식 정도가 순수 히알루론산 기반 하이드로젤 위에서보다 훨씬 증가하였을 뿐 아니라 혈관내피세포의 이동을 촉진시킴으로써 플루오린화 칼슘이 내포된 복합 하이드로젤의 우수한 상처치유능을 알 수 있었다. 또한, 방출된 플루오린 이온으로 인하여 대장균 및 황색포도상구균의

증식을 억제시켜 항균효과를 지닌 것을 확인하였다. 전층 피부결손 동물모델을 이용하여 복합 하이드로젤의 상처 치유정도 및 주변 조직 재생 정도를 평가한 결과, 아무 처리하지 않은 상처는 물론 순수 히알루론산 기반 하이드로젤보다 더 빠른 속도로 상처가 치유되었을 뿐 아니라 상처 주위 표피 및 진피 재생을 효과적으로 촉진시킨 점을 조직학적으로 평가하였다.

이로써, 본 연구에서는 석출법을 통하여 균일하고 우수한 물성을 지닌 히알루론산 기반 세라믹입자의 복합 하이드로젤을 다양하게 제작할 수 있었고, 이를 실제 주입형 필러 및 창상치유재료 등 연조직재생 스캐폴드로의 응용가능성을 평가하였다. 더 나아가 석출입자의 조성을 조절하여 연조직뿐 아니라 경조직용 스캐폴드로써의 연구뿐 아니라, 하이드로젤 내부에서 석출 정도를 달리함으로써 다중상 스캐폴드로의 제작 등으로 활용 및 연구범위를 넓힐 수 있을 것으로 기대된다.

**주요어:** 히알루론산, 석출법, 복합 하이드로젤, 나노 인산칼슘입자, 플루오린화 칼슘, 주입형 필러, 하이드로젤 창상재료

**학 번:** 2014-30215